High Power Doubled and Tripled ML Nd:YAG Laser for Laser Ranging

G. Cavalcabò, L. Fiorina, E. Zanzottera

CISE Tecnologie Innovative S.p.A.

Segrate (Milano-ITALY)

G.C. Reali

Università Di Pavia

ABSTRACT

A 250 mj, 300 ps Q-Switch/active M-L Nd:YAG laser has been designed and tested at the CISE labs, to be used in a variety of applications, laser ranging included.

The system has been estensively tested and qualified to be airborne, and is based on a SFUR cavity with a double rod pumping chamber which allows to amplify the 300 ps pulse produced by the oscillator cavity-dumped system (S/N> 100) to get over 250 mj.

A compact SH-TH, BBO based, generator produces 120 mj and 40 mj of second and third harmonic, respectively.

SYSTEM DESCRIPTION

The system, described in fig. 1, is based on a negative branch resonator, the Self Filtering Unstable Resonator (SFUR[1]) that has demonstrated to be the best cavity for this kind of application because it provides good efficiency, very good beam profile and low misalignment sensitivity. These last properties are very important to reduce the possibility of optical damage of laser components.

The mode-locking is performed by means of an active acousto-optic device, driven by a 50 MHz modulation frequency corresponding to a 1.5 m long optical cavity.

With this configuration the mode-locked train is normally composed by three spikes, the central one containing most of the output energy (65%); in order to have only one spike a cavity dumping scheme has been adopted. In this case the pockels cell is opened to allow Q-switch operation and then suddenly swiched-off in coincidence with the central spikes, which is then coupled out of the cavity by the polarizer. For this reason the beam mode does not present the donut shape which is typical of SFUR with output coupling with a scraper mirror.

The pulse duration is 300 ps, measured by means of a streak camera. An étalon is normally inserted in the cavity to increase the pulse duration to 1 ns, which is required for many application.

The single pulse contrast is better than 5%, limited by the thermal induced birefringence of the laser rod, which is pumped with 10 Hz repetition rate and 35 J flashlamp input energy inside the pumping chamber (containing two Nd:YAG rods).
In order to get a better contrast an external single pulse selector has been installed before the amplifier, it improves the contrast to better than 0.5%.

The energy from the oscillator is typically 30 mj, the amplifier gain is about 8, and the output energy on the harmonic generator is 250 mj.

The harmonic generator is composed by two cascaded BBO crystals, with phase matching Type 1. A half-wavelength plate is inserted between the two cristal to rotate the polarization of the 1064 nm radiation in order to be parallel to the 532 nm radiation for proper phase matching on the tripler.
BBO crystals provide good conversion efficiency (50% of second harmonic and 16% of third harmonic) and good resistance to optical damage.

REFERENCES

1) Gobbi, P.G., Morosi, S., and Reali G.C., and Zarkasi, A.S., "Novel Unstable Resonator Configuration with a Self-Filtering Aperture: Experimental Characterization of the ND:YAG Loaded Cavity", Applied Optics, 24, 26-33, 1985.

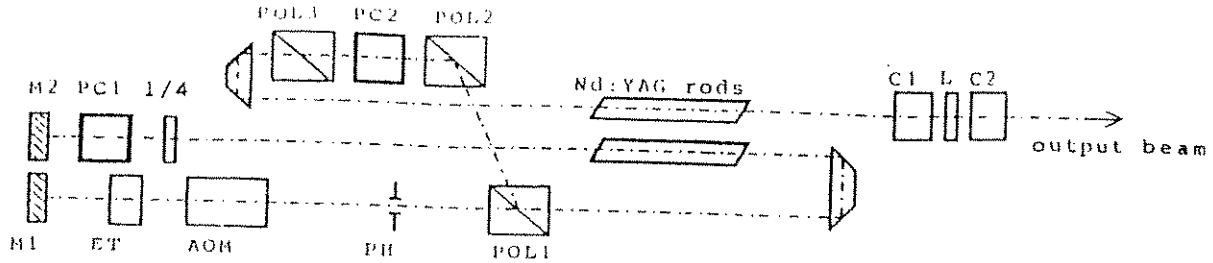

Fig. 1 - Block Diagram of M-L laser

M1: mirror HR at 1064 nm - 0° deg - 0.5 m ROCCV

M2: mirror HR at 1064 nm - 0° deg - 4 m ROCCV

PC1: Pockels cell KD*P

ET: solid etalon 3 mm

1/4: quarter-wave plate at 1064 nm

AOM: acustooptic modulator

POL3: polarizer

PC2: Pockels cell $LiNbO_3$

POL2: polarizer

POL1: polarizer

Nd:YAG rods: 4" x $\frac{1}{4}$" rods

C1: BBO for second harmonic generation

L: half-wave plate at 1064 nm

C2: BBO for third harmonic generation

TABLE 1

Specifications of M-L laser system

Resonator:	SFUR with cavity dumping
Configuration:	Oscillator + Amplifier
Pumping chamber:	Single flashlamp-double rod
M-L type:	Active with A.O. modulator
Pulse duration:	300-1000 ps
Pulse selection:	with cavity dumping and external pulse selector
Pulse contrast:	0.5%
Pulse energy at 1064 nm:	250 mj
Pulse energy at 532 nm:	120 mj
Pulse energy at 355 nm:	40 mj
Repetition rate:	10 Hz
Flashlamp input energy:	35 j
Harmonic generator:	with two BBO crystals PM I

PULSE SELECTOR FOR SHORT LASER RESONATOR

M.ČECH

Faculty of Nuc Sci and Physical Engineering
Czech Technical University
115 19 Prague, Brehova 7
Czechoslovakia
Telex 121254 fjfi c
Phone +42 2 848840

General

A fast pulse selector for short laser resonator is described. Main advantages of the new selector are solid state electrical switching, small size, different modes of operation - single pulse or semitrain, 3 nsec pulse train spacing for good operation (good laser resonator mechanical stability), internal time delay 10 nsec.
The selector is used on the laser radar station Helwan, Egypt [3].

Electrical and optical design

For a pulse selecting from laser pulse train is often used a krytron [1] or a solid state switch on avalanche transistor basis as a high voltage switching element. The krytron switch produces high electrical noise. Due to this krytron drawback a fast solid state high voltage switch was developed.

High voltage pulser consist of two transistor cascades, Fig.1. Each cascade contains fifteen 220V $U_{CES(BR)}$ transistors of Czechoslovak production. The first cascade generates leading edge of 3200V pulse.The pulser is triggered by trigger signal with 15V amplitude. Special opto-switch is used as the trigger detector [2].

The second cascade generates trailing edge of pulse This cascade is self-triggered by increasing input voltage over breakdown level.

The selector consists of two Pockel cells (KD*P crystals) PC1 and PC2, (Fig.2.) placed between two optically crossed polarizers. Two electro-optical crystals are used due to:

a) the quarter wave voltage is sufficient for properly pulse selecting
b) two crystals arranged optically in series improve the contrast ratio of the selected pulse

Input polarizer selects vertical polarization from laser beam and isolates the oscillator from reflection too. The train of pulses then enters the Pockels cells tandem. Normally no voltage is applied into two cells and therefore the train of pulses with vertical polarization is reflected from its direction by the output polarizator and starts the trigger detector. After start signal the first avalanche cascade is switch on and the Pockels cells voltage is increasing to quarter wave value. The Pockels cell effect rotates the plane of polarization of the linear polarized light of the one pulse of train about 90° after passing the pulse by PC1 and PC2. The output pulse from the PC2 passes straight by the output polarizer. After passing the selected pulse the quarter wave voltage is removed from the Pockets cells and the rest of pulses from the train is again reflected by the output polarizer.

Experimental results

The selector has been tested by two input signals: mode-locked train and GI pulse.

Mode-locked train has been generated by oscillator with dye ML51 with 30% input transmission placed at the Brewster angle in the resonator. The spacing between pulses is 2.4 ns, Fig.3. The very short resonator has been used to obtain the envelope of the selected pulses. Output of selector shows Fig.4. Internal delay time from trigger signal to high voltage output is 10 nsec. A shape of selected pulses demonstrates the fast switching capability. Fig.5 shows sum of 100 pulses and demonstrates the low time jitter of the selector.

The selector is possible to modify for semitrain generation very easy. For this purpose it is necessary to remove the trailing edge cascade. This effect is obtained by disconnecting the transistor circuit in cascade. This method has been used in Helwan station [3].

Optical switching have been tested in slicer mode. A giant laser pulse generating in the same laser resonator (only the dye ML51 was changed to BDN folio) entered to the selector. The selector sliced the shorter pulse from GI input pulse. Sum of 10 nsec GI pulse and the sliced pulse is shown on Fig.7.

Fig.8 describes the main sliced pulse parameters. FWHM of the optical pulse is 3.2 nsec and the width near the zero level is 6 nsec only. It means pulse spacing 3 nsec in train is sufficient to very good contrast for pulse selecting.

Literature

[1] H.Jelínková: Constant Gain Pulse Forming Laser, proc. of the 4th International Workshop on Laser Ranging Instrumentation,Austin,1981,published in Bonn,1982

[2] I.Procházka: Start Detector for Mode Locked Train Laser Radar, proc. of the 6th International Workshop on Laser Ranging Instrumentation,Antibes,1986

[3] K.Hamal et al.:Interkosmos Satellite Laser Station in Helwan, Version Single Pulse / Semitrain. in this proceedings

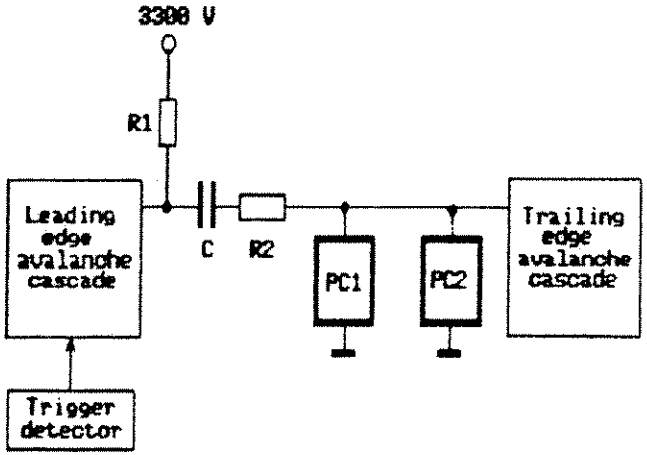

Fig.1: Electrical block diagram of the pulse selector

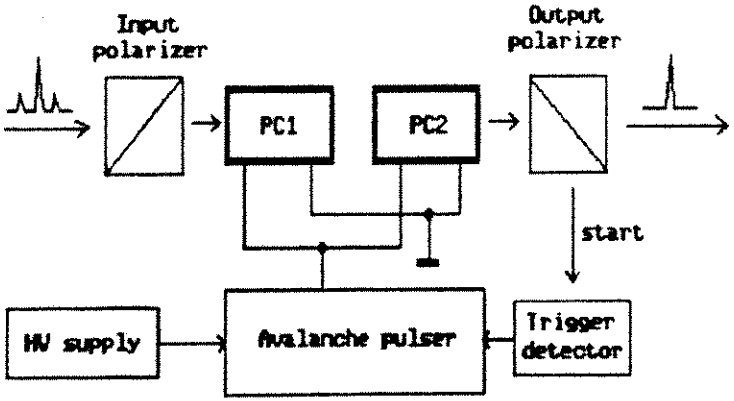

Fig.2: Optical block diagram of pulse selector

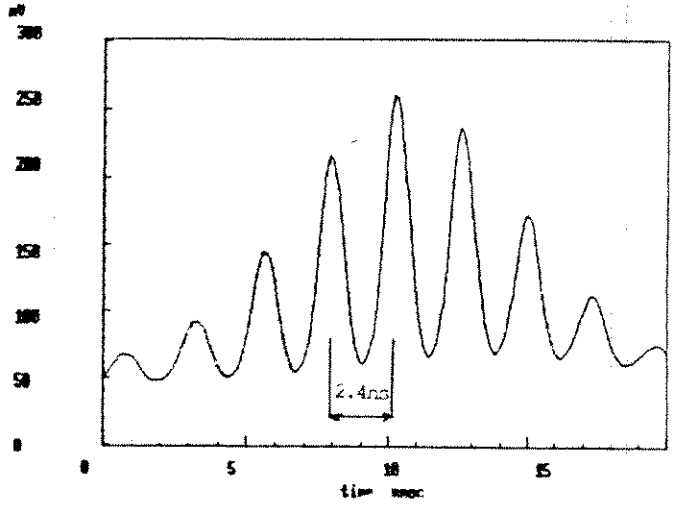

Fig.3: Mode locking train

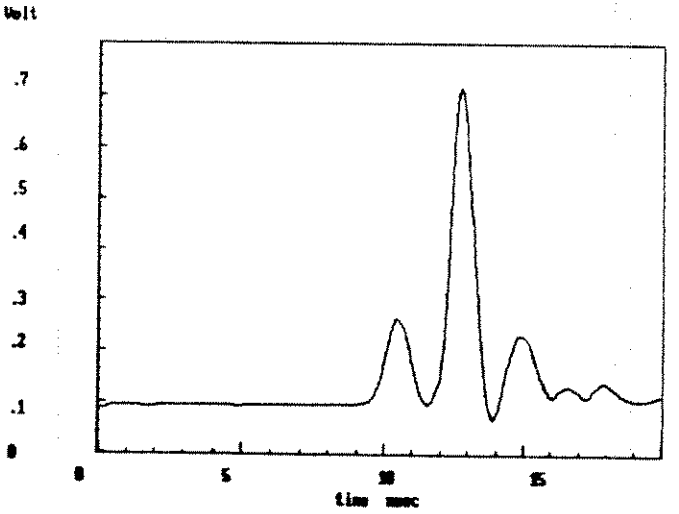

Fig.4: One pulse selected from train

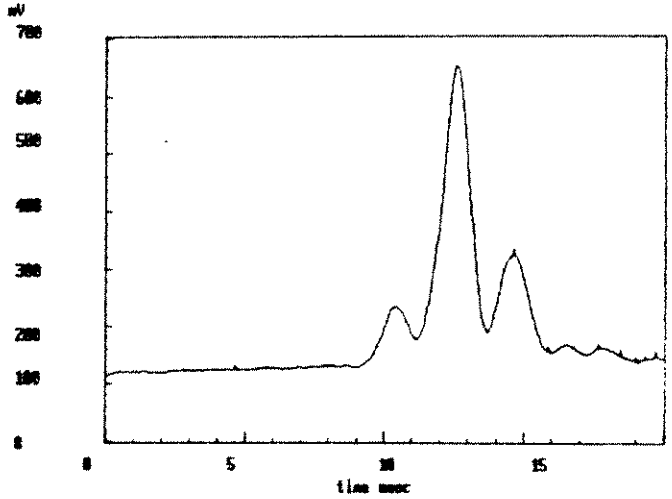

Fig.5: Sum of 40 selected pulses

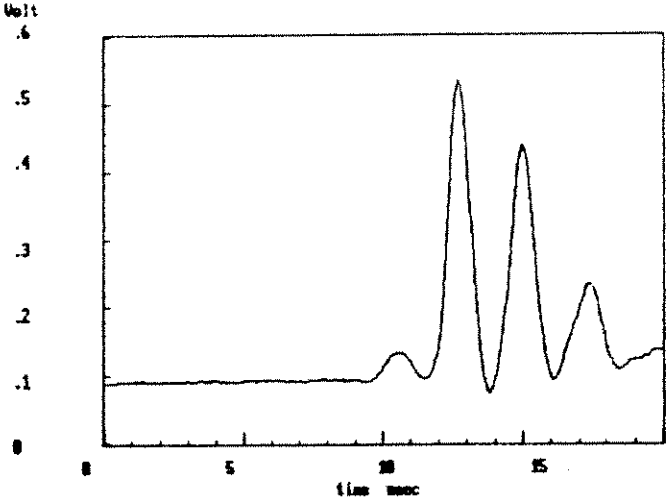

Fig.6: Semitrain / Trailing cascade removed /

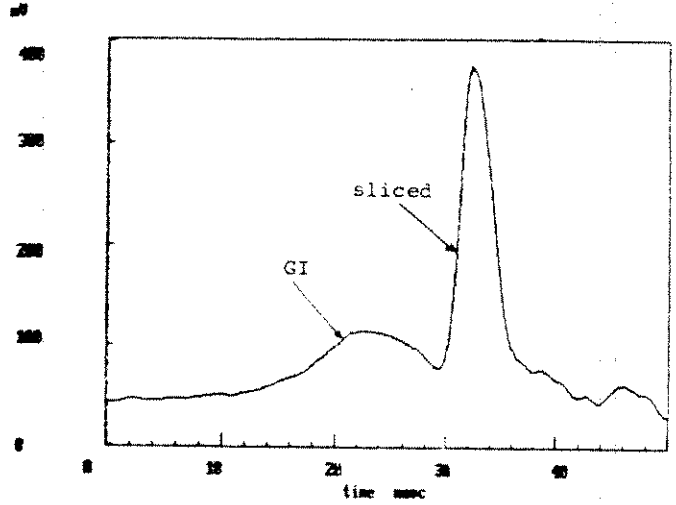

Fig.7: Sum of GI and sliced pulses

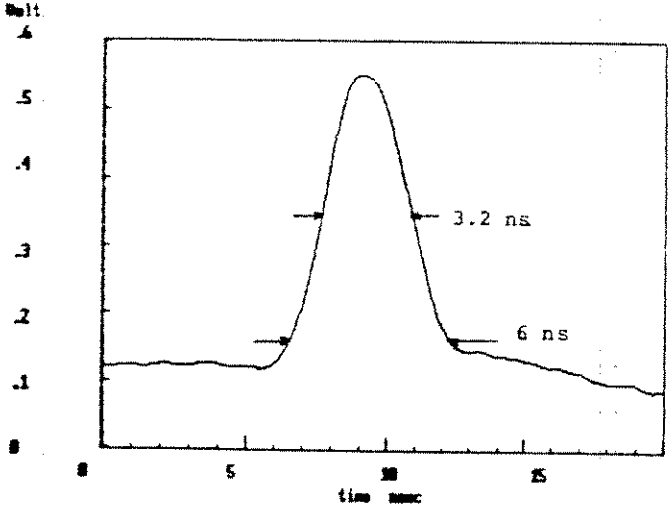

Fig.8: Sliced pulse from GI

Detection

Avalanche photodiodes optimized for single-photon detection

S.Cova, M.Ghioni, A.Lacaita and G.Ripamonti

Politecnico di Milano, Dipartimento di Elettronica and
Centro di Elettronica Quantistica e Strumentazione Elettronica CNR

Piazza L. da Vinci 32, 20133 Milano, Italy

Telephone (+39) 2 - 2367604
Facsimile (+39) 2 - 23996126
Telex 333467 POLIMI I

ABSTRACT

Single optical photons can be detected with silicon avalanche diodes working in the triggered avalanche mode, at bias level higher than the breakdown voltage. New device structures, optimized for working in this mode, have been designed and fabricated. The criteria for the design are presented and discussed.

The device performance is illustrated by experimental results. The carrier diffusion effects, and the associated slow tails in the resolution function, have been minimized. Full width at half maximum (FWHM) of the resolution curve better than 30 picoseconds have been obtained. Low dark-count rates at room temperature are also obtained, in the range from 100 to 10000 counts per second.

1. INTRODUCTION

Avalanche photodiodes can be used as ultrafast detectors in single photon timing techniques. These devices are p-n junctions working at a bias above the breakdown voltage, in the triggered avalanche mode. They have been successfully employed in various applications, such as optical fiber characterization by means of optical time domain reflectometry, laser ranging, fluorescent and luminescence decay analysis, etc.[1,2].

An important parameter in single-photon detection is the time resolution, that is, the precision in the determination of the photon arrival time. It is currently defined as the FWHM of the curve obtained in tests with ultrafast light pulses.

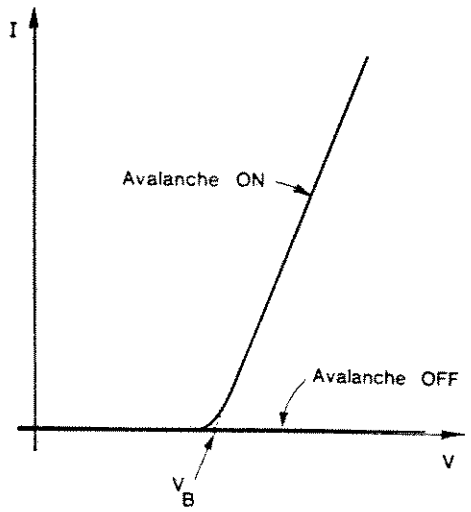

Fig.1 Typical reverse I-V characteristic of an avalanche photodiode (V_b is the breakdown voltage).

Special avalanche photodiodes can be designed for achieving the best timing performance. They are called SPADs (Single photon avalanche diodes) or TADs (Triggered Avalanche Diodes). We have designed SPAD devices that show a time resolution better than 20 ps FWHM. This is the best result so far reported in single photon timing measurements.

Some commercially available avalanche photodiodes, having low dark current (e.g. RCA C30921S), can also work in the triggered avalanche mode. They do not attain such a high time resolution. However, they can provide higher quantum efficiency than SPADs in the red and near infrared wavelength range.

Commercial devices are available with sensitive area of several thousands of square microns, which is sufficient for most of the envisaged applications, though it is considerably smaller than that of the photomultiplier tube (PMTs).

In applications where the small active area is acceptable, these photodiodes are a solid state alternative to PMTs, providing wider spectral sensitivity range, better time resolution and the typical advantages of solid state devices: ruggedness, small dimensions, low cost, long life, low operating voltage and low power dissipation.

In the following, we shall describe the performance of a commercial APD as a single photon detectors. Afterwards, we will describe specially-designed devices, having optimized time resolution performance.

2. DEVICE OPERATION

In Fig.1 is shown the reverse current-voltage characteristic of an avalanche photodiode. Above the breakdown voltage, it exhibits two branches. In the upper

branch (ON state), an avalanche current in the mA range flows, corresponding to a self-sustaining avalanche process. In the lower branch (OFF state), the avalanche process has not yet been triggered, and no current flows. When a carrier succeeds in triggering the avalanche, the current rises to the ON value: if the carrier is photogenerated, the leading edge of the avalanche current is synchronous with the arrival time of the photon. The avalanche current continues to flow until an external circuit quenches the diode by lowering the bias voltage close to or below the breakdown voltage. After a finite dead time, the working voltage of the device is restored, in order to make possible the detection and timing of another photon.

The avalanche can also be triggered by carriers thermally generated or emitted from trapping centers in the depletion layer of the active junction. This causes a dark count rate, that lowers the signal-to-noise ratio in single-photon measurements. It can be reduced by a proper design of the device structure and employing careful fabrication processes.

A widely employed method of operating the device is ***passive quenching*** [3,4]. The diode is inversely biased through a ballast resistor R_L (100 kΩ or more). The avalanche triggering corresponds to closing the switch in the equivalent circuit of Fig.2. The avalanche current discharges the capacitances, the diode voltage drops and the diode current correspondingly decreases; when the voltage gets close to the breakdown, the avalanche is quenched (switch open in the equivalent circuit). The diode voltage then slowly rises towards the bias voltage; since the capacitances are slowly recharged by the small current in the ballast resistor. An output pulse with fast leading edge is available across a low value resistor connected to the other end of the diode, typically 50 Ω. The pulse amplitude depends on the applied overvoltage $(V-V_b)$ and on the series resistance R_S of the diode.

The slow recovery in the passive quenching arrangement represents a serious drawback. A photon arriving during the first part of a recovery will be lost,

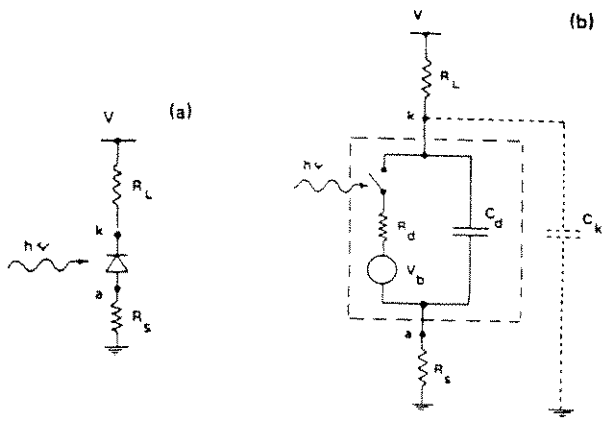

Fig.2 a) Passive quenching arrangement and b) equivalent circuit for triggered avalanche operation. R_L ballast resistor; R_S output resistor; C_d device capacitance; C_k stray capacitance.

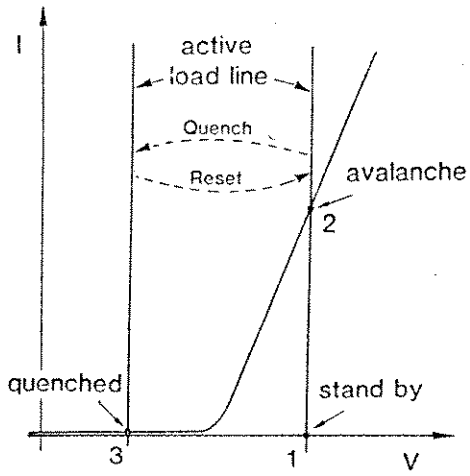

Fig.3 Active quenching. 1-2: avalanche triggering by a carrier. 2-3: fast quenching transition, forced by the load line shift. 3-1: fast recovery forced by the load line reset.

since the voltage is still too low. A photon arriving later on, during a recovery, can trigger the diode, but it will find the diode voltage lower than the bias supply voltage. The pulse generated will therefore have an amplitude lower than the standard and will cross the threshold of the timing circuit with a significantly longer delay. In conclusion, if the count rate is not very low (a few kcps), the detector dead time is not well defined and the time resolution is worsened.

The inherent resolution of the APD can be exploited by using the ***active quenching*** method [5,6]. The principle (see Fig.3) is to force the quenching and resetting transitions in short times (tens of nanoseconds or less) by using a controlled low impedance source for biasing the diode. The rise of the avalanche pulse is sensed by a fast comparator, whose output switches the bias voltage

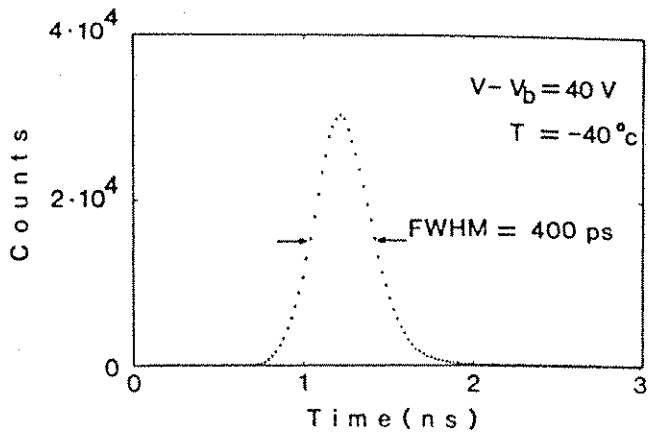

Fig.4 Time resolution of the RCA C30921S diode: bias voltage 40 V above the breakdown; temperature -40 C; active quenching circuit.

source down to the quenching level. After a well defined deadtime, having accurately controlled duration, the bias voltage is swiftly and accurately restored to the operating level. A standard pulse synchronized to the avalanche rise can be derived from the comparator output and used for the time measurement.

3. COMMERCIAL DEVICES

RCA C30921S are silicon avalanche photodiodes designed for optical communications at 830 nm with data rates up to 1 GBit/s, laser ranging and other applications requiring high speed and high responsivity. They have a reach-through structure [7]. The back of the wafer is etched in correspondence to the active area in order to reduce the thickness to about 35 μm. At the operative voltage the structure is practically fully depleted; the residual neutral p^+ layer on the back is less than 1 μm thick and the total depleted depth is about 30 μm. The light enters through the back of the mounted diode chip. The useful photosensitive area has about 0.2 mm^2 area. The device is specified to have a breakdown voltage of 225 V and a very low dark current in the multiplication region, so that even at room temperature it can be biased above the breakdown voltage to operate in the triggered avalanche mode. In this paper we report only the conclusions of extensive tests of these devices which have been described in detail in ref. [8].

The active quenching circuit was employed. It provided quenching pulses up to 40V with rise time less than 40ns. The best results were obtained with the maximum available excess bias voltage of 40V at -40 C. 400 ps FWHM was obtained (Fig.4). In Fig.5 a semilogarithmic plot of the same data shows that the response is remarkably well-behaved: secondary peaks and non-monotonic irregularities, that plague the response of PMTs, are absent and only a small exponential tail is observed. This tail is attributed to that part of the electrons photogenerated in the neutral p^+ layer of the device that reach the depletion layer by diffusion [8].

From a practical standpoint, these devices can be operated at about 0 C, with a time resolution up to 420 ps FWHM but a high dark count rate up to 240 kcps.

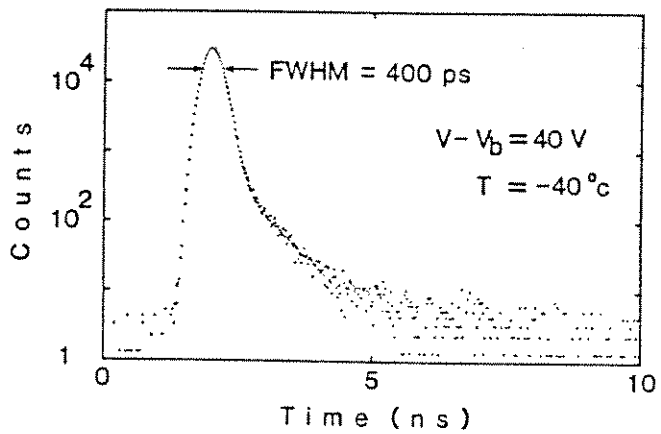

Fig.5 Same data as Fig. 4 with logarithmic vertical scale.

4. SINGLE PHOTON AVALANCHE DIODES

In order to achieve the best time resolution, the avalanche photodiode must be specifically designed. The experiments performed on commercial devices and properly designed avalanche photodiodes, show that:

(a) the breakdown must be uniform over the whole active junction in order to produce a standard macroscopic current pulse.
(b) the dark count rate must be sufficiently low, that is, the thermal carrier generation and the concentration of trapping centers should be minimized;
(c) the depletion region width must be small. At the saturated velocity, the carriers transit time is of 10 ps/μm. Depending on the depth at which the photon is absorbed, the avalanche will be triggered at different times. In order to achieve a time resolution of a few tens of picoseconds the depletion region must be no more than one micron thick.
(d) the time resolution improves by increasing the maximum electric field. Therefore, the devices must have a low breakdown voltage, and be operated at the maximum bias voltage.
(e) the time resolution is adversely affected by the increase of the active area. This is due to physics of the propagation of the avalanche perpendicular to the field.
(f) in order to minimize the tail in the resolution curve, the thickness of the neutral region, beneath the active junction must be minimized, without increasing the series resistance beyond a few kΩ.

It is evident from the previous requirements that a proper design must consider the tradeoff between the quantum efficiency of the detector, the achievable time resolution and the signal-to-noise ratio.

We had previously implemented and tested prototype SPAD devices using the geometry described by Haitz [3]. The response of the prototype SPAD devices is shown in Fig.6. In order to reduce the time response of the detector, the diffusion tail must be reduced. Our approach was to design epitaxial device

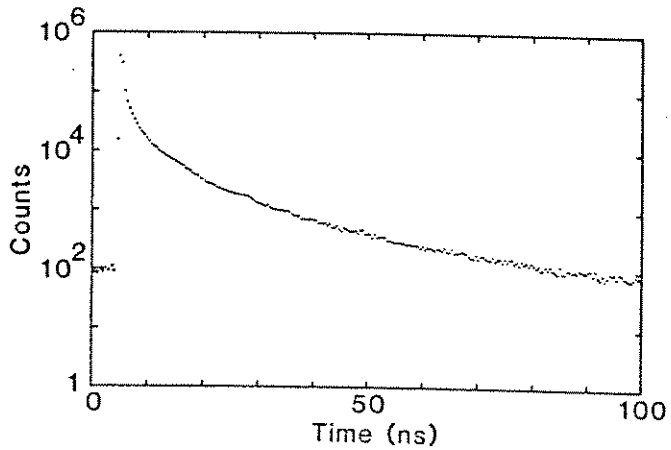

Fig.6 Optical pulse of a gain-switched laser diode (Hamamatsu C1308 Picosecond Light Pulser, 833 nm wavelength) measured with the prototype SPAD structure in a TCPC set-up.

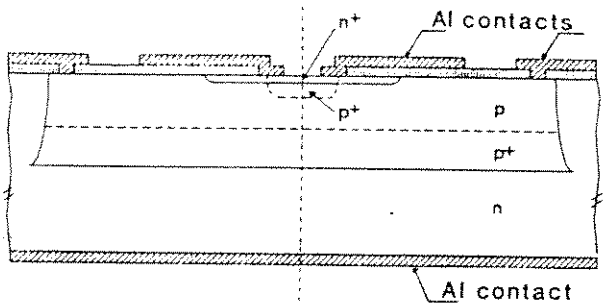

Fig.7 Schematic cross section of the double epitaxial SPAD structure.

structures in which the substrate acted as a sink for photogenerated carriers and the active junction was located in a suitable epistrate, but without increasing the series resistance beyond a few kΩ. A new SPAD structure with two different p epilayers grown over the n substrate is shown in Fig.7. The buried epilayer, which is only 2 μm thick, provides a low resistivity path (0.3 Ωcm) to the side contact. The active n^+p junction is built in the upper, low-doped p epistrate (10 Ωcm), which is only 2.5 μm thick. The low p doping in the outer part of the n^+p junction and a field plate raise the edge breakdown voltage up to 50 V. Devices with this geometry have been fabricated with different diameters of the sensitive area, in the range from 8 to 20 μm, with a breakdown voltage of 16 V [9] and low dark count rate, 2 kcps typical at 19V for the smallest area devices. Fig.8 shows, in logarithmic scale, the pulse of a gain-switched laser-diode measured using the double epitaxial SPAD. It is characterized by a peak (55 ps FWHM) and by a much shorter, exponential-like, diffusion tail, with a lifetime of 270 ps. The actual value of the detector time resolution is 45 ps FWHM.

In order to attain very high time resolution, maximum electric field higher than 400 kV/cm are required. However, a very high electric field is expected to significantly increase the dark count rate. In fact, the carrier emission probability from generation centers is strongly enhanced by field-dependent

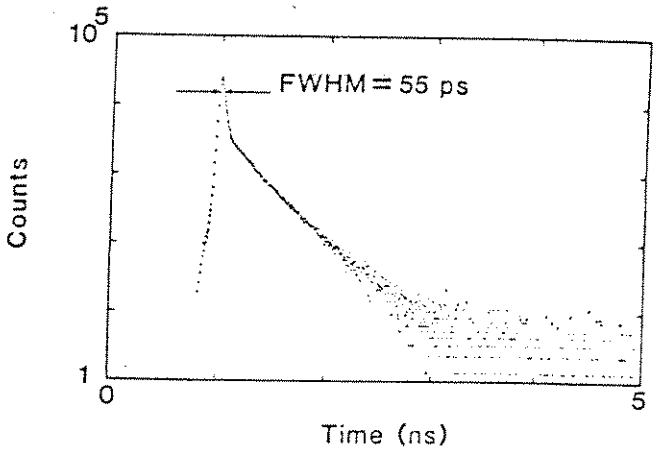

Fig.8 Same as Fig.6 but with the double epitaxial SPAD. Note the different scales.

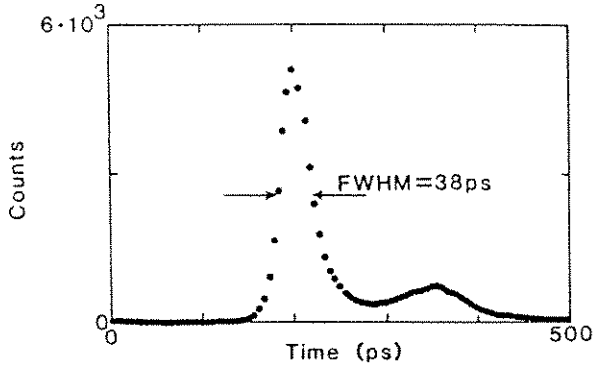

Fig.9 TCPC measurement with SPAD having 13V breakdown voltage at -65 C temperature, showing better than 20 ps FWHM device resolution.

effects [10]. For this reason, devices having a breakdown voltage around 13 V have a markedly higher dark-count rate of 100 kcps at 6 V excess bias. In Fig. 9 is shown a typical result, obtained at -65 C. Since the laser and the electronics provide 31 ps FWHM, the time resolution of the detector is evaluated to be 20 ps or less. At room temperature a time resolution better than 30 ps has been reached with the same devices.

5. CONCLUSIONS

Avalanche photodiodes working biased above the breakdown voltage can detect single photons. The device operation and the criteria for designing special silicon avalanche photodiodes have been presented and discussed. We have reported the experimental results obtained with devices designed to minimize the diffusion tail in the time response and to achieve high time resolution. We have measured 20 ps FWHM, that is the best result so far reported in single photon timing measurements. For comparison we have reported experimental results obtained with the commercial APD RCA C30921S.

In conclusion, single photon detectors having particular characteristics can be designed and tailored to the specific application. Suitable circuits permit their operation even at very high dark cont rates with optimum performance.

REFERENCES

1. S.Cova, G.Ripamonti and A.Lacaita, *Nucl.Instrum.Methods* A253, 482 (1987)
2. G.Ripamonti, S.Cova, *Electron.Lett.* 22, 818 (1985)
3. R.H.Haitz, *J.Appl.Phys.* 35, 1370 (1964); 36, 3123 (1965)
4. P.Antognetti, S.Cova and A.Longoni, *Proceedings of the 2nd Ispra Nuclear Electronics Symposium, Euratom Publication* EUR 5370e, 1975, pp. 453-456
5. S.Cova, A.Longoni and A.Andreoni, *Rev.Sci.Instrum.* 49, 1186 (1981)
6. S.Cova, A.Longoni and G.Ripamonti, *IEEE Trans.Nucl.Sci.* NS-29, 599 (1982)
7. P.P.Webb, R.J.McIntyre and J.Conradi, *RCA Rev.* 35, 234 (1974)
8. A.Lacaita, S.Cova and M.Ghioni, *Rev.Sci.Instrum.* 59, 1121 (1988)
9. A.Lacaita, M.Ghioni and S.Cova, *Electron.Lett.* 13 ,841 (1989)
10. G.Vincent, A.Chantre and D.Bois, *J.Appl.Phys.* 50, 5484 (1979)

Prospect of Laser Ranging using a Semitrain versus a Single Pulse

Karel Hamal, Ivan Procházka

Czech Technical University, Prague
Faculty of Nuclear Science and Physical Engineering
115 19 Prague 1, Břehová 7
Tel.: +42 2 848840, telex 121 254 FJFI

Abstract

Here is a wide effort to increase the precision of laser ranging *Ground–Ground*, *Ground–Satellite*, *Satellite–Ground* and *Ground–Moon*. Considering the error budget and the energy balance it is desirable to have pulse duration bellow 70 psec and the output energy as high as possible [1]. However, the ultimate limiting factor is the catastrophic damage threshold of optical elements of the laser transmitter system. To overcome this limit the semitrain concept has been suggested and experimentally verified at Helwan SLR Station.

E.Silverberg [2] proposed and experimentally verified to use the train of pulses for SLR. We used [3] this version at the Helwan SLR Station since 1984 to 1986. However, the ambiguity causes serious difficulties when analyzing data. B.Greene [4] proposed to use a multiple pulse for ranging .

To increase the ranging precision (to decrease the RMS of the measurement) the multiphoton detection is widely exploited. On the other hand there are several reasons to use the *single photon detection* (SPD):

- Lunar ranging (inherently based on SPD)
- Great distance ground–ground ranging.
- High orbit satellites (stationers, Etalon etc.) are ranged at medium size laser stations at SPD.
- Lageos is ranged at modest size stations (mobile etc.) at SPD.
- The laser transmitter delivers lower average power by a factor of ten in comparison with multiphoton detection (less complex, lower optical damage risk).
- Lower eye risk.
- The existing laser transmitters are based on Nd:YAG crystals generating naturally pulses 20–30 ps long.

- Low systematic error (detector delay is not dependent on the signal strength).
- The receiver can be based on single photon solid state diode [5].

Some examples of the RMS budget (state of art technology) are on Table 1.

Considering the error budget and the energy balance, an ultimate limiting factor is a catastrophic damage threshold of optical elements of the laser transmitter ([1] Ref [P3]) given by the peak density. It is therefore obvious to employ a multiple pulse, or a *semitrain* of pulses, or a burst of pulses. See Fig.1. To generate this semitrain pulse is rather simple because all stations built until now employ mode-locking technology, where the origin of the short single pulse is anyhow mode locked train, which exists at the beginning of the laser transmitter chain. Additionally, because of the same origin, the time interval between consequent pulses is given by the round trip time of the oscillator resonator and is naturally determined in femtoseconds. This fact is in favor of the data analysis of the returned signal ([1] Ref [P7]). Therefore an adoption of the multiple pulse is straightforward.

We calculated the *return rate / semitrain* and we did compare it with the single pulse concept. Fig.2. Considering return rate / single pulse = 30% we obtained for a burst of 4 pulses the return rate up to 85% and maintaining single photon detection level,as well. In the experiment we have kept peak power of laser transmitter at the safe level 3 GW/cm^2 in green for both the single pulse (output energy 30 mJ, pulse duration 20 ps) and the*semitrainof 2 or 3 pulses* (80 mJ / 20 ps). We adjusted the return rate / single pulse = 0.1 and we obtained the return rate / 4 pulses = 0.25.

Comparing the concept from Fig.1, the single "long" pulse (300 ps, energy = 1) and the *semitrain* of 5 "short" pulses (60 ps, total energy = 1) the return rate / single pulse is equal.

The typical pass of the satellite laser ranging using the *semitrain* concept is on Fig.4 and also in [1] Fig.1. The ranging data analysis performed at Univ. of Texas and Goddard Space Flight Center verified the data performance, no ambiguity of the measured range has been detected within 200 passes. Statistically, the semitrain contributed a factor of 2.6 to the number of echoes when ranging the LAGEOS satellite.

Considering SPD, the implementation of the *semitrain* concept brings approx. twice increase of the return rate comparing to the single pulse. Comparing the single relatively "long" pulse with the burst of "short" pulses, the *semitrain* concept brings a higher precision at the same return rate. Considering the inherent SPD (Moon, high satellites, long distance ground– ground) it is the only solution when a higher precision is desired.

The adoption of the *semitrain* concept require a negligible hardware knowhow for the pulse selector electronics and a software knowhow for the data analysis. The *semitrain* concept is extremely appropriate for single photon detection using a photodiode [5].

Concepts of semitrain

Energy/single pulse = energy/semitrain

Goals : equal peak power

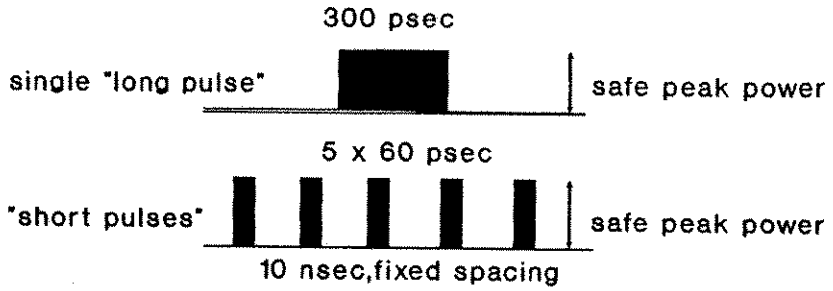

Application : ground , satellite , Monn

Energy/single pulse < energy/semitrain

Goals :equal peak power
higher return rate

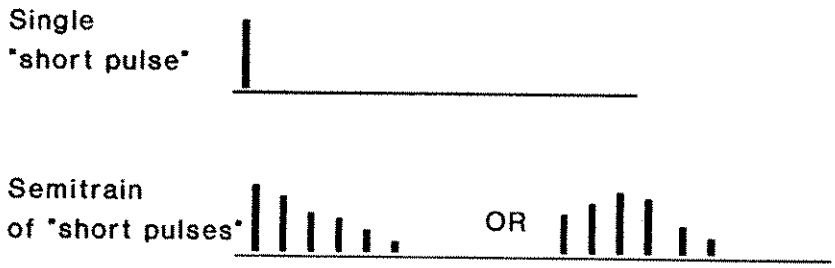

Application : ground , satellite

Fig.1

Ranging system performance

Semitrain versus single pulse

Single photon, diode detection

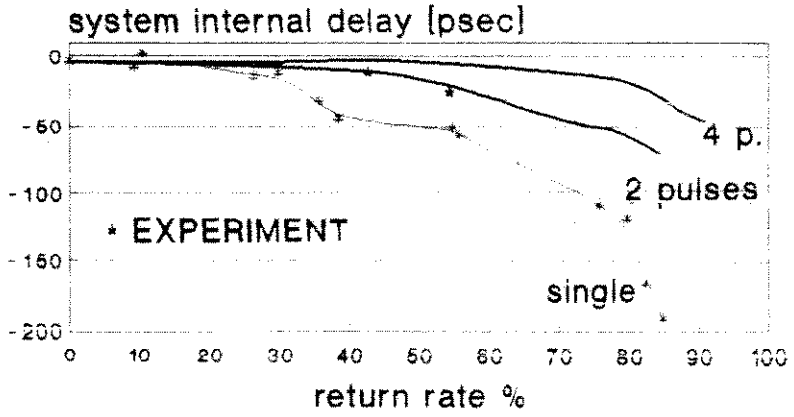

Fig.2

Single photon ranging

Ground / satellite / Moon

RMS BUDGET [psec]

Laser	300	100	60	20
				future
If Gaussian	120	40	25	8
Counter	36	36	36	20
START	40	40	30	10
STOP	35	35	35	20
r.s.s.	135	75	65	35
Experiment		*80 (Graz)*		
Satellite	25	25	25	
r.s.s.	140	80	70	
Experiment		*90 (Graz)*		

Table 1

Prospects of using a semitrain. Summary.

- Single photon detection
  - ⋆ higher return rate, attractive for low Q.E. detectors
    → HIGH RETURN RATE
  - ⋆ shorter echo pulses
    → LOW PULSE DURATION JITTER CONTRIBUTION
  - ⋆ no signal strength dependance
    → LOW SYSTEMATIC ERROR
- Laser transmitter
  - ⋆ shorter pulses are available
    keeping the peak power densities within safe values
    → HIGH RANGING PRECISION
  - ⋆ exploiting fully the inversion available in the amplifiers rods
    → HIGH AVERAGE POWER
  - ⋆ lower peak power densities
    → LOW OPTICAL DAMAGE RISK
- Modifications: Single pulse →*semitrain*
  - ⋆ hardware / slicer electronics
  - ⋆ software / data analysis

References

[1] Degnan J.J.: Satellite Laser Ranging, Current Status and Future Concepts. IEEE Trans.on Geoscience and Remote Sensing, Vol.GE-23, No.4,July 1985, 398

[2] Silverberg E.C.: The TLRS and the Change in Mobile Station Design Since 1978. Proceedings of the IVth International Workshop on Laser Ranging Instrumentation U.of Texas,Austin, USA, 1981, 59

[3] Hamal K. et al.: Interkosmos Laser Radar, Version Mode Locked Train. Proc. of the Vth International Workshop on Laser Ranging Instrumentation, Herstmonceux Castle,Great Britain, 1984, 214

[4] Greene B., presented at the Vth International Workshop on Laser Ranging Instrumentation, Herstmonceux Castle, Great Britain,1984

[5] Prochazka I., Hamal K., Sopko B., Photodiode Based Detector Package for Centimeter Satellite Ranging.in this proceedings

Two wavelength laser ranging using the semitrain of pulses, *proposal*

HARWARE CONFIGURATION

Laser • semitrain of 4-10 pulses

Detector • common for both wavelength,
• single photon ranging, diode
• detecting either one or the second wavelength,which are separated in time

Electronics • no change

Radar optics • two wavelength coatings
• dual peak receiver filter

ADVANTAGES

- simple receiver and diode detection package (re)construction for two wavelength
- the use of semitrain permits to increase the return rate up to 80% for both wavelength maintaining single photon echoes
- the same detector & counter for two wavelength delay measurement is resulting in high temporal stability and simplicity
- most of the systematic errors of the TW delay measurements cancel out by averaging

DRAWBACKS

- the two wavelength data return rate is limited to effectively 40%
- the ranging data processing procedure is more complex

Avalanche photodiode detection

at 1.06 μm

J.F. Mangin

C. Dumoulin

C. Veillet

CERGA/OCA
Av Copernic F-06130 GRASSE

Abstract

Ranging the Moon by using a YAG laser at its original wavelength could present various advantages, if it is possible to use a detector sensitive enough for single photoelectron detection.

This paper will present the arguments which lead to 1.06 μm laser ranging, and the various tests made for developing an avalanche photodiode detector. The first results obtained at both 1.06 and 0.532 μm will be presented in another paper in these proceedings.

1 - Why 1.06 μm ?

YAG laser with frequency doublers providing pulses at 0.532 μm are used for laser ranging of satellites and the Moon. The good behaviour of the detectors generally used (sensitivity of PMT and good time properties of MCP) makes this wavelength quite suitable for an accurate ranging.

Changing the wavelength from 0.532 to 1.06 μm is not really useful for satellite ranging, except for two-colour ranging with YAG at its fundamental and doubled (or tripled) frequencies. But it gives some advantages for Lunar Laser Ranging, as the amount of photons received back from the Moon in LLLR is very low (1 photon detected every 100 to 1000 shots with a 300 mJ/300 ps pulse ...).

Undoubled YAG will at first provide twice the energy extracted from a single frequency doubler, and four times the number of photons. Furthermore, the sensitivity of

photodiodes could be four times larger than a PMT (80 % versus 20 %), and the atmosphere, as soon as the target is low and the sky not very clear, is much more transparent in infra-red than in green. The only one disadvantage is the difraction of the cornercubes on the Moon, which will make four times larger the area illuminated by the returning beam.

For testing on the Moon itself the validity of these assumptions, it has decided to develop a detector for 1.06 μm.

2 - Which photodiode ?

The main goal of this study is to detect in single photoelectron mode at 1.06 μm. Various photodiodes have been tested. Germanium photodiodes are too noisy (at least at room temperature), and most of the Silicium photodiodes have a low sensitivity in near infrared, except RCA C30954 and RCA C30955. As the latter is less noisy, due to a smaller area, it has been finally chosen.

3 - Testing the RCA C30954

Between -50 and 20 degrees Celsius, the output pulse depends essentially on the applied high voltage and on the number of received photons. Three operating modes are available :
- a standard mode where a high number of photons is reqired for an output signal higher than the noise level, and for a short time response.
- a low Geiger mode, where a low input signal can be detected, but with a time response which can reach 20 ns ... - a high Geiger mode, where a permanent voltage V_H slightly smaller than the breakdown voltage V_B is applied, and a high Geiger pulse ($\simeq V_H/2$) sent for the time needed.

The first two modes are useless for Lunar Laser Ranging, and only the last one has been tested. It gives a full avalanche on noise or signal, and the output signal level depends only on $V_B + V_H/2$ and not on the number of photons.

Figure 1 displays the diagram of the electronic device used for generating the Geiger pulse. A TTL pulse is sent when the diode has to receive something, and it is possible to obtain a gate as short as 100 ns.

Various experiments have been made in order to see how the noise, the transit time and the sensitivity depend on the Geiger pulse voltage. Fig. 2, 3 and 4 present the plots obtained with the photodiode used (RCA C30954). It is clear that the transit time is decreasing, and the sensitivity increasing with the voltage, but the noise seems stable after a given Geiger pulse voltage.

4 - The avalanche photodiode in operation

The detector package is put in an RCA cooling box which permit to reach -45 degrees Celsius after half an hour through a Peltier effect. This box is implemented on the receiving table of the telescope.

This photodiode has been used for ranging both satellites and the Moon, and the first results are presented in another paper (see these proceedings, 'multiple wavelengths ranging' Section).

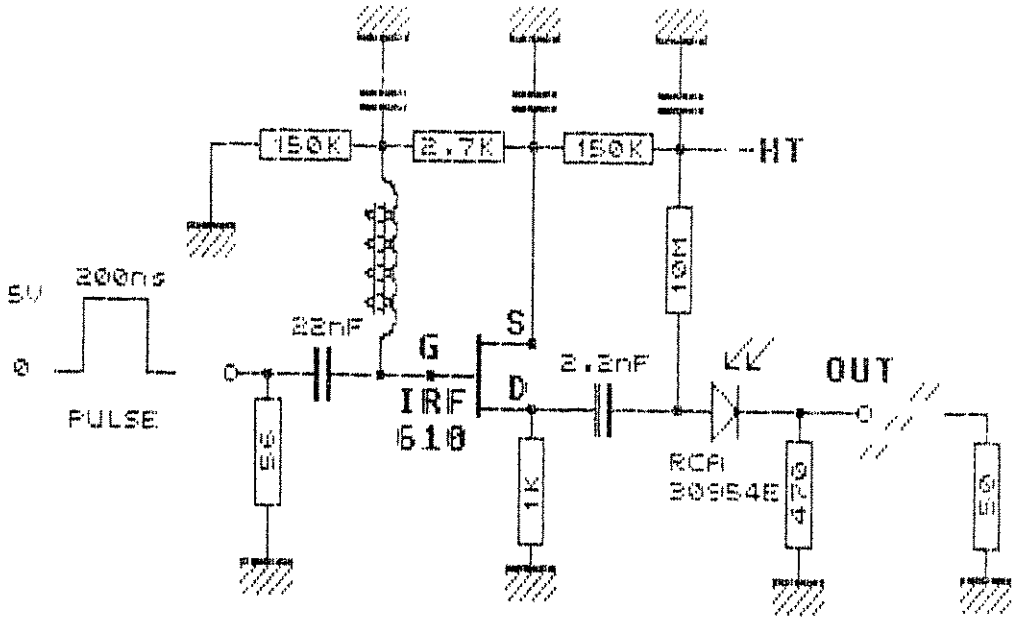

Figure .1: *The electronic diagram of the power supply designed for using the RCA photodiode in Geiger mode*

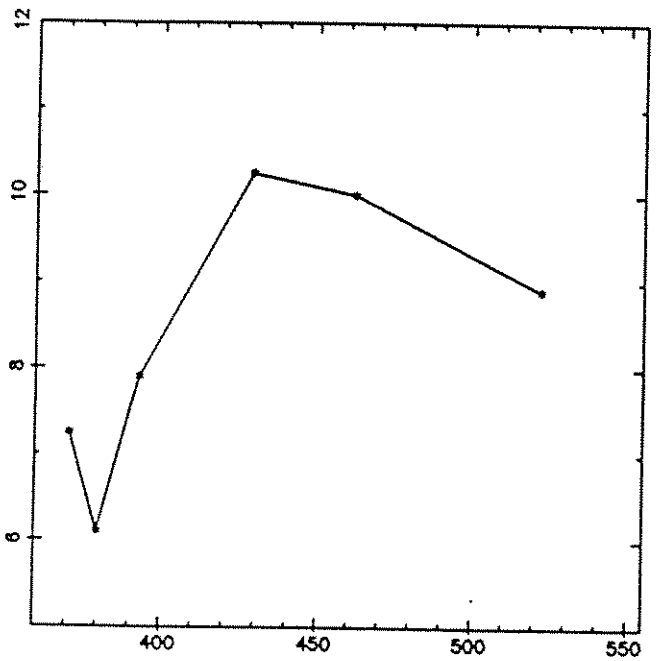

Figure .2: *Noise versus voltage applied to the photodiode*

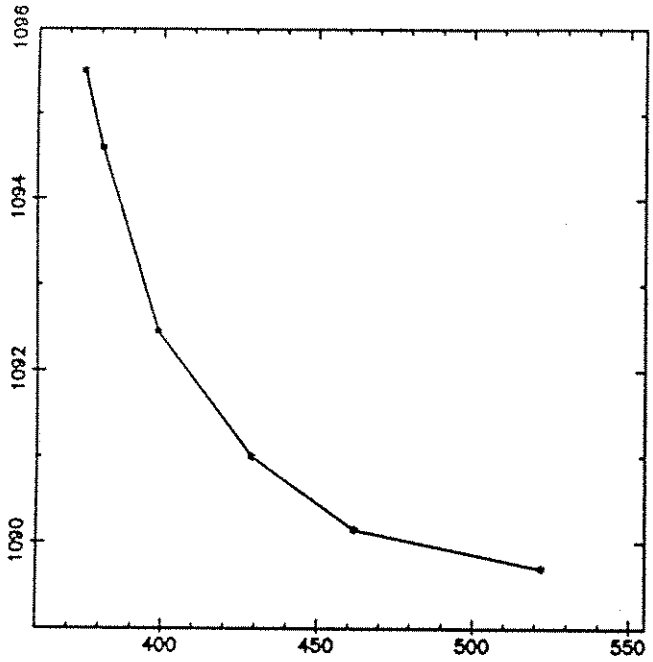

Figure .3: *Variation of the transit time relative to the voltage applied to the photodiode. The transit time itself (in ns) is not measured directly, but added to a transit time in cables and electronic devices which remains constant during the tests.*

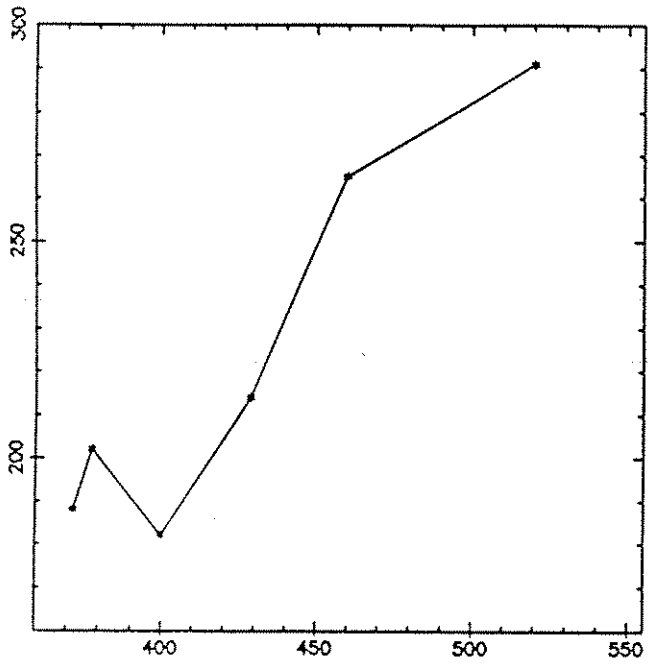

Figure .4: *Sensivity versus voltage applied to the photodiode. The number of detections over 2000 shots is given as a function of the voltage. The energy of the arriving beam (laser pulse attenuated) is kept roughly constant during the tests.*

PHOTODIODE BASED DETECTOR PACKAGE FOR CENTIMETER SATELLITE RANGING

I.PROCHAZKA, K.HAMAL, B.SOPKO

Faculty of Nuclear Science and Physical Engineering
Czech Technical University
115 19 Prague 1, Brehova 7
Czechoslovakia
telex 121254 fjfi c
phone +42 2 848840

General

We are reporting on the novel design of the fast photodiode for satellite laser ranging along with the design of the photodiode based receiver package for centimeter satellite laser ranging. The final goal is to construct an all solid state laser ranging detector chain. The diode based receiver having 3 cm (190 psec) ranging jitter operating at -60 Centigrade has been reported by S.R.Bowman [1], the single photon diode operating in the active quenching mode for spectroscopy at a room temperature, having an active area of 8-40 um in diameter, has been reported by Cova [2]. Both, the photodiode and the detector package have been designed and fabricated at the Czech Technical University, tested at the INTERKOSMOS Laser Radar Station in Helwan, Egypt and finally installed at the Lustbuehel Observatory in Graz, Austria, by March 1989.

Photodiode design

The diode, biased above the break voltage is connected to the active quenching circuit. We focussed the attention to the diode structure design and manufacturing technology and we modified the gating/ quenching circuit. The latest achievements in the diode samples fabrication technology permitted to increase the diode active area to 100um diameter while maintaining acceptable dark count rates at a room temperature and the fast response, as well. The diode structure was optimised to get as low detection jitter as possible on the expenses of the detection quantum efficiency at longer wavelength.

Detector package construction

The photodiode based detector package consisting of the diode, the discriminator, the active quenching and gating circuit and the collecting optics has been constructed. The detector package is interfaced to the laser ranging receiver via an X,Y fine adjustment setup. To simplify the installation in the field, the external dimensions of the device are the same as for the Hamamatsu microchannel plate photomultiplier R2287U.

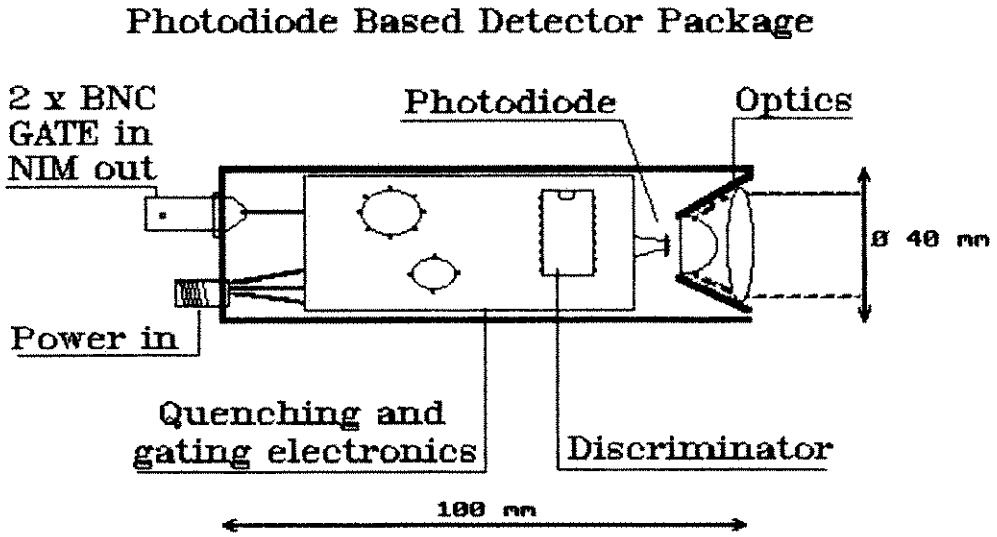

Fig. 1.

Detector package main characteristics,single photon ranging

Diode chip	construction	planar on Si
	break voltage	29 Volts, -18 mV/Kelvin
	diameter	100um , (20-200um available)
	quant.efficiency	> 20% at 532 nm
Optics	built in	aperture 15mm, f/D=1.0
Discriminator	built in	fixed threshold,single photon
Gating	on ext.pulse	TTL input pulse
Output pulse	uniform	NIM timing pulse
Jitter	contribution	35 psec RMS
Power requirements	external	+/-6V,100mA,-30V,1 mA
Dimensions	cylinder	diam. 40 mm,length 100 mm
Weight	total	110 grams, incl.optics

Detector package performance

The dark count rate and the jitter contribution of the detection package are dependent on the diode bias above the break voltage, Fig.2. Taking into account the satellites ephemeris quality, on one hand and the background noise contribution in the daylight tracking on the other hand, the voltage has been set to the maximal acceptable value of 3 Volts above break. The ranging jitter and the detection delay versus the signal strength, the time walk, for the Graz SLR are summarized on Fig.3. It has to be noted here, that the detector is designed for single photon detection, it responds ever to the first photon absorbed in the diode active area. Taking into account the laser pulse length of 100 psec, the time bias when detecting multiphoton echoes has to appear. For single photon echoes the time walk together with the system stability is within one millimeter. The calibration jitter budget of the laser ranging systems in Graz and Helwan 2 are summarized :

Calibration jitter budget

	Graz SLR (100 ps laser)	Helwan 2 (20 ps laser)
Time interval unit (HP5370)	36 psec	36 psec
Start circuit (optoswitch)	20 psec	20 psec
Start pulse length contribution	40 psec	8 psec
Receiver package	35 psec	35 psec
Stop pulse length contribution	40 psec	8 psec
Resulting system jitter r.s.s.	76 psec	55 psec

Conclusion

The detector package described above is in routine use at the Graz SLR since March 1989. Its ruggedness, high quantum efficiency, low jitter and excellent temporal stability make it attractive for satellite laser ranging. There are no external discriminators in the ranging chain. The system ranging precision estimate is typ. 13 mm RMS on Lageos, Starlette and Ajissai satellites [3]. The subcentimeter ranging precision has been achieved in ground target ranging experiments using 20 psec laser pulses. Ranging to the satellite, the contribution of the satellite retroreflectors array geometry to the error budget and the nonstandard distribution of the data have to be considered. The attractivity of the detector package space application is obvious.

References

[1] Bownam S.R. et al.: proc. of the VIth International Workshop on Laser Ranging Instrumentation,Antibes,1986

[2] Cova S. at al.,IEEE J.Quant.Electronics,QE-19,630,(1983)

[3] Kirchner G.: Status Report on SLR Station in Graz. in this proceedings

OPERATIONAL CHARACTERISTICS OF COMMERCIAL SILICON AVALANCHE PHOTODIODES FOR USE AS LASER RADAR RECEIVERS

L. Grunwaldt, R. Neubert, Li Ya *)

Central Institute for Physics of the Earth
Telegrafenberg A 17
Potsdam - 1561 , GDR
Telephone: 3100, Telex: 15305 vde pdm dd

Abstract

Commercial silicon avalanche photodiodes of RCA C 30902 type were tested for some parameters influencing their possible use as receivers in laser radar systems. Experiments were performed with respect to the spectral dependence of quantum efficiency, timing jitter at single photon level, signal strength dependent time-walk effects and influence of strong background radiation on detection probability (daylight tracking). Part of the measurements was taken both at room temperature and with dry ice cooling. A selected sample of RCA C 30902 E yielded a maximum quantum efficiency in the red of about 60 % and around 100 ps jitter in single photon response. Its use in daylight tracking even under room temperature conditions is possible. Power dependent time walk strongly suggests to work strictly at single photon level or to monitor the signal strength very carefully.

*) on leave from Chang Chun Satellite Observatory
of the Academy of Sciences
Chang Chun, Peoples Republic of China

Silicon avalanche photodiodes (APD) used in a reverse biased configuration as Geiger mode photodetectors (GMP) have been shown to be an interesting alternative to photomultiplier tubes in ranging experiments with 3rd generation laser radar stations (/1/, /2/). Their advantages

- simple, robust construction
- wide spectral range
- high quantum yield
- high internal amplification
- high speed (risetime of few ns or less)

offer a lot of possibilities for use as receivers, taking into account also disadvantages as

- small active area (which limits the field of view)
- necessary cooling in some cases
- nonlinearity of output versus input signal (saturated device).

The aim of this work was to study some of the properties of commercially available APD types in more detail, also directed to the question, if these types could already meet the requirements for a 4th generation laser ranging detector (2-colour) as

- very high time resolution (jitter of less than 50 ps, maybe in multiphoton case)
- no signal strength dependent time walk effect (or, if present, a controllable one to a few ps)
- high quantum efficiency for both laser wavelengths (e.g. 1.064 and 0.53 µm)
- daylight ranging capability.

The experiments were performed with selected samples of the well-known RCA C 30902 E- and S-type APD, concentrating on the E-type finally.

General operational conditions

In all experiments performed, the APD was operated in the passive quenching mode according to the electrical scheme shown in Fig. 1. A negative bias voltage about 5 V below breakdown was applied via a 5 MΩ load resistor and gating pulses of variable height (-20...-80V) and about 2 µs length were superposed via the capacitor to overbias the diode during the receiving of the signal. In all experiments, bias voltage was -240 V for operating at room temperature and -175 V for -60 °C. A typical oscillographic recording for 40 V overbias is shown in Fig. 2. The risetime of the Geiger pulse is about 1.5 ns with a nearly linear slope between 20 and 80 per cent of the maximum height in the leading edge.

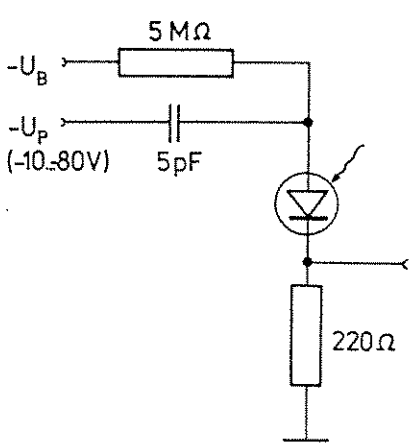

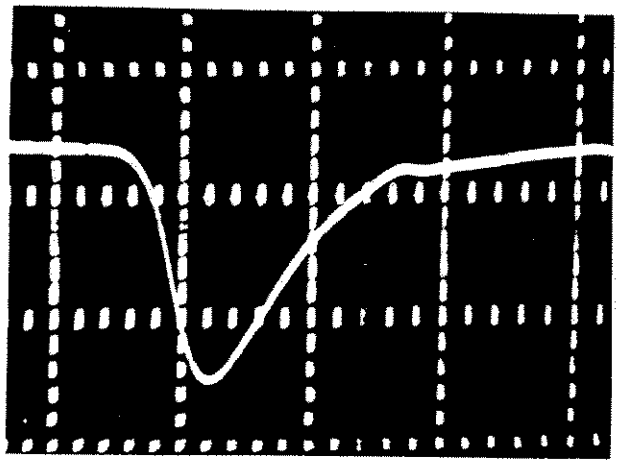

Fig. 1: Electrical scheme of APD circuit
Fig. 2: Oscillographic recording of a typical Geiger pulse. Horizontal scale is 5 ns/div

Spectral dependence of detective quantum efficiency

For measuring the spectral response, a spontaneous light source (tungsten filament lamp) was used in connection with a grating monochromator SPM-2 and calibrated neutral density filters for input signal attenuation in front of the diode. The pulser unit was operated at a constant frequency (10 kHz) driven by a pulse generator and the output signal of the diode was fed directly to the input of an HP 5370 A counter. When the gating pulses are supplied at a fixed frequency, only in some percentage of cases a photon is detected during the gate pulse time. Thus, by operating the counter in frequency mode, it shows a frequency f_s smaller than the gate pulse frequency f_p. The quantum efficiency QE can be obtained from the formula

$$QE = (1/N \cdot t_p)(\ln(1/(1-P_s)) - \ln(1/(1-P_d))$$

where

N - photon flux per second
t_p - gate time (pulse width)

$P_s = f_s/f_p$ - total detection probability of signal and noise

$P_d = f_d/f_p$ - dark pulse probability.

The photon flux incident on the diode was calibrated by a vacuum thermopile. QE - measurements were performed for wavelengths between 532 and 1064 nm.

The results both for room temperature and -60 °C are shown in Fig. 3. Generally, the maximum QE was found in the red region (700...750 nm). Taking into account, that the absolute calibration of the photon flux is accurate to about 20 % only, there is fairly good agreement with other authors, who obtained their values for selected wavelengths by fully different methods (see /1/ for 532 nm and /3/ for 822 nm). The decrease in quantum efficiency in the infrared region with lowered temperature is clearly seen. This effect is to be expected due to the decreasing probability of photon-phonon interactions in the absorption process with decreasing temperature. In any case, the quantum efficiency for both 532 and 1064 nm differs for at least one order of magnitude for the given type of diode.

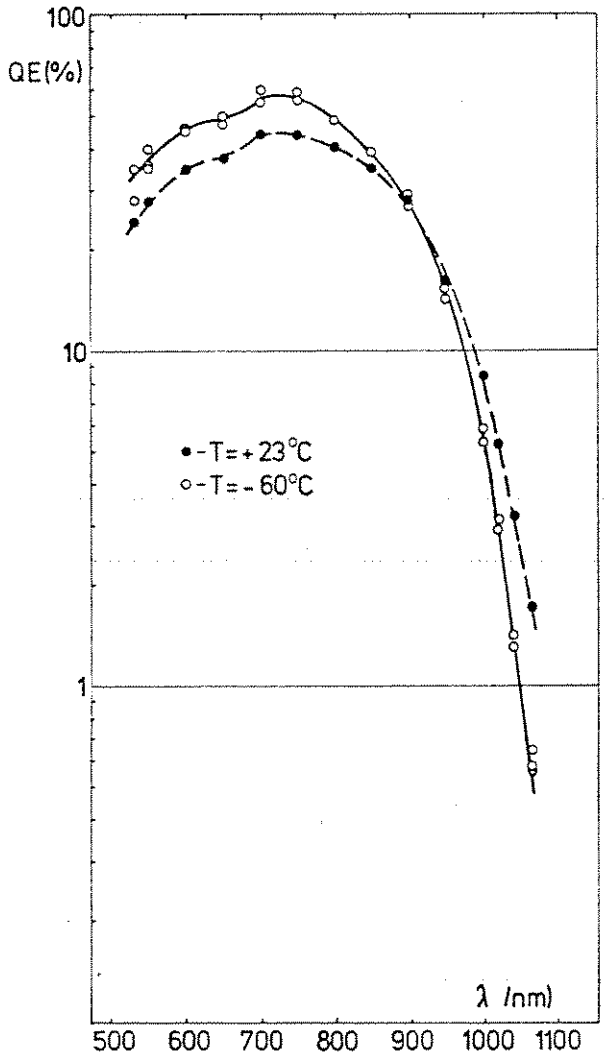

Fig. 3:
Wavelength dependence of quantum efficiency for RCA C 30902 E, No. 56320

Temporal resolution, signal dependent time shift

The temporal behaviour (jitter) of APD's operated in the Geiger mode was tested by an indoor ranging experiment using a passively mode-locked, frequency doubled Nd:YAG-laser with about 5.3 ns pulse spacing, which can be operated both in the pulse group or single pulse mode. The start signal was derived from a fast pin-photodiode SP 102. Using an identical photodiode for the stop channel, the jitter in this strong-signal case was about 60...70 ps depending on the laser pulse height stability. The laser pulse width could not be monitored during the experiment, but has been determined using both two-photon fluorescence and streak camera tube, to be in the range 30...100 ps dependent on dye concentration and adjustment. The laser signal was fed to the diode after an optical delay of about 20 m, the pulser for overbiasing the APD was triggered by the trigger signal of the pulse selector to ensure that the full voltage was applied to the receiver immediately before the arrival of the laser signal. Both start and stop signal were fed directly to the start and stop channel of an HP 5370 A counter, without further discrimination. Attenuation to a given signal level was provided by calibrated ND filters in front of the receiver. From a selectable number of returns (typically 300 for a single pulse, 1000 for a group) a histogram of time intervals was created. The width of individual histogram peaks (after a least square fit procedure with Gaussian envelope for a group or a 2 σ filtering for a single pulse) is used as a measure of the timing jitter. In general, we found no difference between pulse group and single pulse; in all results shown here a selected single pulse was used.
To operate the APD at the single photon level the signal was attenuated down to a detection rate of 20 % or below. Two typical histograms for different values of the gating pulse voltage are shown in Fig. 4. For low gating voltage, a remarkable asymmetry of the histogram distribution is observed. With increasing gating pulse voltage, both jitter and asymmetry decrease (see also Fig. 5). For pulse voltages around 100 V, a single photon jitter for the RCA 30902 E of about 100 ps is expected. Fig. 5 was obtained after a filtering excluding all measurements with deviations greater than two times the standard deviation. All points contain more than 90 % of the original measurements.

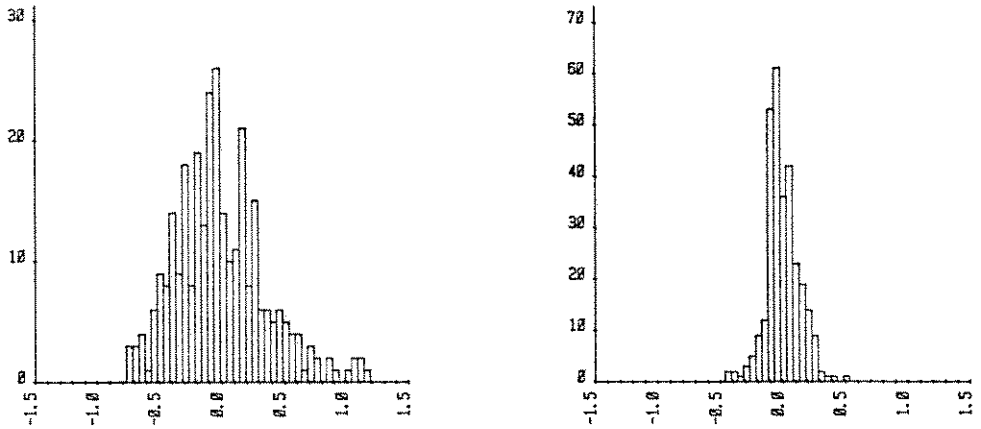

Fig. 4: Histogram of time intervals at single photon level for different gating voltages.
Left: 25 V, right: 75 V.

To test for signal strength dependent variations of jitter and time shift, the incident laser signal was varied from the single photon region up to about 1000 photons by replacing the ND filters in front of the APD. Also this measurement was carried out both for room and dry ice temperature. The timing jitter is decreasing from 120 ps in the single photon region to about 60 ps at several hundred photons and seems to be limited mainly by laser fluctuations. The signal dependent time shift is shown in Fig. 6. After a flat region for average photon numbers below 1, there is a more or less linear slope for two orders of signal magnitude. A "saturation" seems to exist for signal levels higher than 10^3 photons.
The reason for this time shift should be found mainly in the process of avalanche formation for different signal strengths, because oscillographic recordings of Geiger pulses in the case of single photon response and maximum signal showed no noticeable difference in shape and height of the pulses.

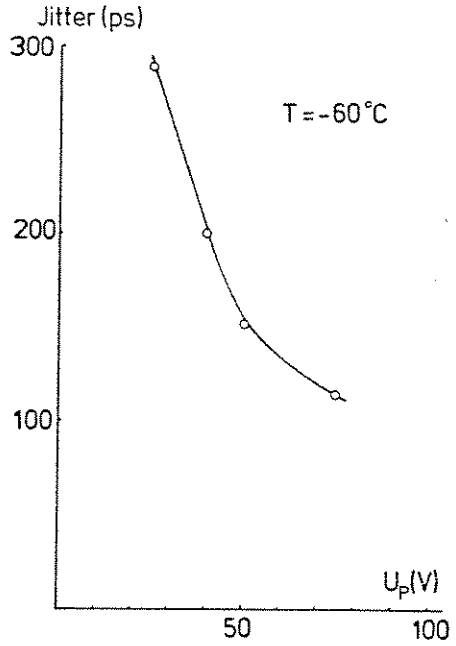

Fig. 5: Timing jitter versus voltage for RCA C 30902 E, No. 56320 operated at -60 °C

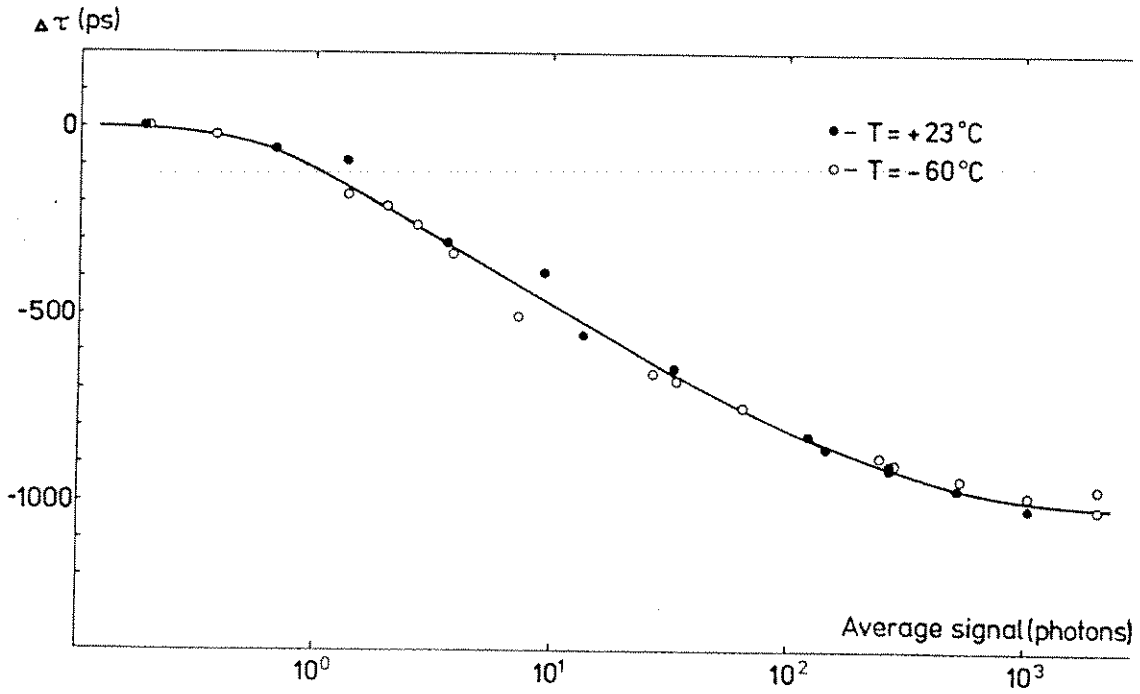

Fig. 6: Signal dependent time shift for diode RCA C 30902E No. 56320

The influence of background light on the detection of weak pulse signals

To test the daylight tracking capabilities of a GMP receiver, a special indoor ranging experiment was performed. In this case a light emitting diode (LED) was used as a pulsed signal source. The receiver was additionally illuminated with cw background light.

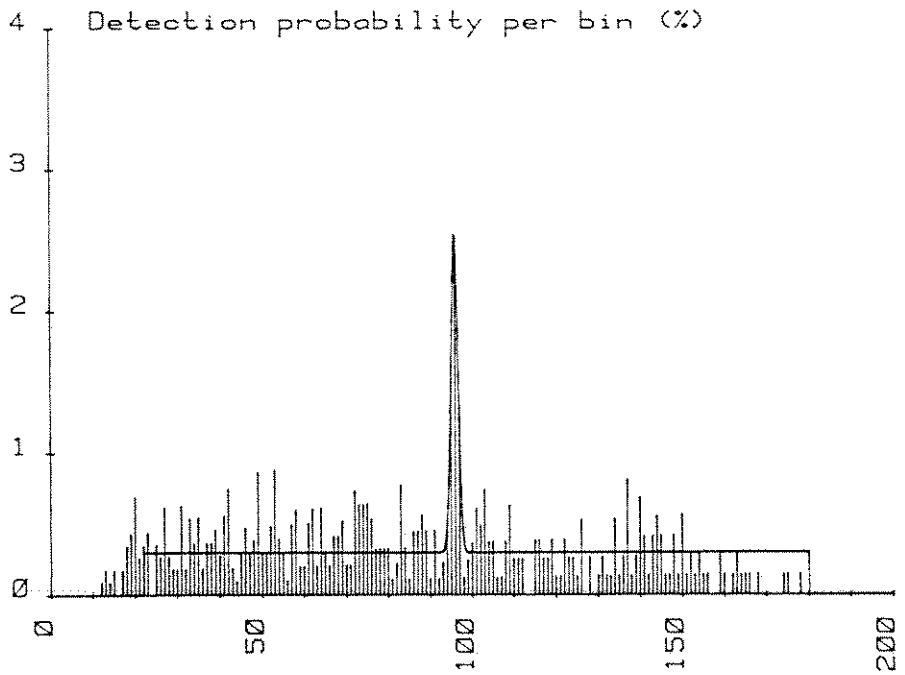

Fig. 7: A typical time interval distribution at high background level.

Background frequency	: 200 kHz
Signal detection probability	: 9.8 %
Bin width	: 15 ns
Scale on x-axis	: channel number
Scale on y-axis	: detection probability per bin

The HP 5370 counter was started with the electrical pulses from the LED supply and stopped by the output of the detector. The APD was gated with 2,5 µs long pulses of about 25 V amplitude.
After collecting sufficient time interval data in the computer memory, their distribution was calculated (see Fig. 7). The signal of the LED was attenuated to give a total detection propability of about 10 % for all runs, but the background was set to different levels up to a detection probability of 40 % within the 2,5 µs gate time. This would correspond to a background count rate of 200 kHz.
Fig. 7 represents the empirical distribution of the detection probability, calculated from the original histogram by correcting for the pill-up effect /4/ using the relation:

$$P(I) = H(I)/(N - \sum_{k=1}^{I-1} H(K))$$

where

P(I) - corrected detection probability in the I'th bin
H(I) - original number of events in the I'th bin
N - total number of trials (including cases of no return)

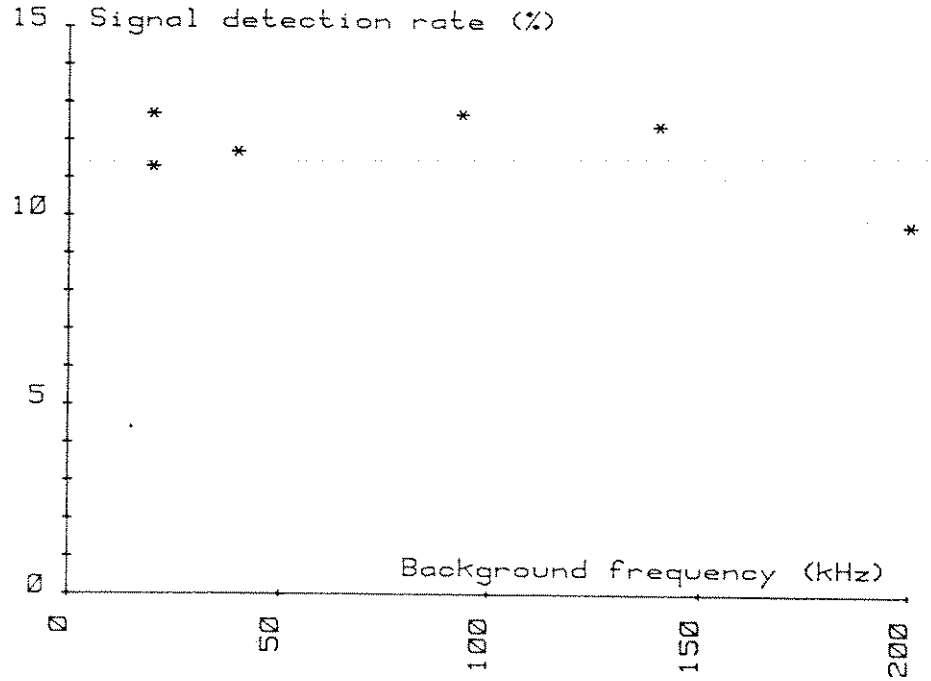

Fig. 8: Dependence of the signal detection probability from background frequency (compare text)

The resulting probability distributions P(I) for different background levels were then fitted by the sum of a flat (background) and a Gaussian (signal) distribution (see envelope in Fig. 7) using least square method. The area under the Gaussian is used as a measure of the signal intensity. This quantity is plotted in Fig. 8 in dependence from background pulse frequency. No significant decrease of the signal was observed at least up to 100 kHz background.
Reducing the gate time of the GMP below 1 μs, a background level of 1 MHz could be tolerated, which is reasonable for daylight tracking.

Acknowledgement

The authors are indebted to Mr. Z. Neumann from Ondrejov Observatory for supply of the APD-pulser, to Mr. J. Will from Institute for Optics and Spectroscopy, Berlin for the design of the pulse selector and to Mr. A. Bartels for experimental support.

References

/1/ Bowman, S.R.; Shih, V.H.; Alley, C.O.: The use of Geiger mode avalanche photodiodes for precise laser ranging at very low light levels.
Proc. 6th Intern. Workshop on Laser Ranging Instr., Antibes (1986), pp. 173-184

/2/ Hamal, K.; Jelinkova, H.; Prochazka, I.; Sopko, B.: Single photon solid state detector for ranging at room temperature.
Proc. 6th Intern. Workshop on Laser Ranging Instr., Antibes (1986), pp. 185-188

/3/ Robinson, D.L.; Metscher, B.D.: Photon detection with cooled avalanche photodiodes
Appl. Phys. Lett.51 (1987) No. 19, pp. 1493-1494

/4/ Saleh, B.: Photoelectron Statistics
Springer Series in Optical Sciences Vol. 6, Berlin 1978

Contribution of the Central Institute for Physics of the Earth No.1776

The Application of Semiconductordetectors in the WLRS

U. Schreiber
Forschungseinrichtung Satellitengeodäsie
der Techn. Univ. München
Fundamentalstation Wettzell
D-8493 Kötzting

N. Brandl, D. Feil, K.-H. Haufe
Institut für angewandte Geodäsie
Fundamentalstation der
Forschungsgruppe Satellitengeodäsie
Wettzell
D-8493 Kötzting

Abstract:

Avalanche diodes in general have the property of very short risetimes and can be used in microwaveapplications for frequencies exeeding several hundred GHz. **A**valanche **P**hoto**d**iodes (APD) placed in the Geiger mode can be used for single photon detection over a broad spectral range, showing only little variation in their response behaviour. In the modular design of the WLRS at Wettzell, the use of APD' s seemed desirable for ranging capability at the fundamental frequency of the Nd:YAG Laser (Quantel). Using a APD RCA 30902s at the WLRS, preliminary results are presented in brief.

Introduction:

Since the WLRS was designed to be a lunar tracking station, it uses the optical telescope for both transmitting the laser pulse and receiving a return from the remote target object. This requires a switch to select either a transmitting path or a receiving path. A rotating mirror disc with holes in it, serves for this purpose (fig. 1).

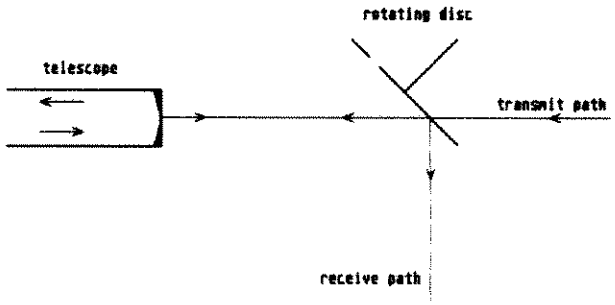

Fig. 1: A schematic sketch of the transmit/receive switch at the WLRS

For this reason, the detector is placed on an optical table in the lower level laboratory. To allow the change between a MCP (microchannelplate) and a PMT (photomultiplier), there are two permanent detector ports which are selected by flipmirrors. The design can be modified to allow the use of 2 detectors simultaneously. With the help of a frequency sensitive beam-splitter (dichroic mirror), ranging with a laser system transmitting both fundamental and second harmonic frequency can be achieved.

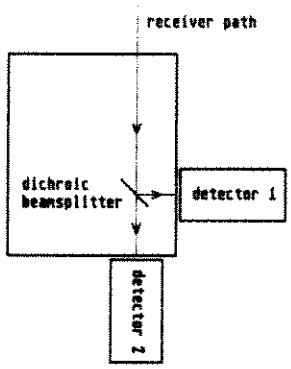

fig. 2: the simultaneous operation of two detectors allows the registration of laser pulses containing 2 distinct frequencies.

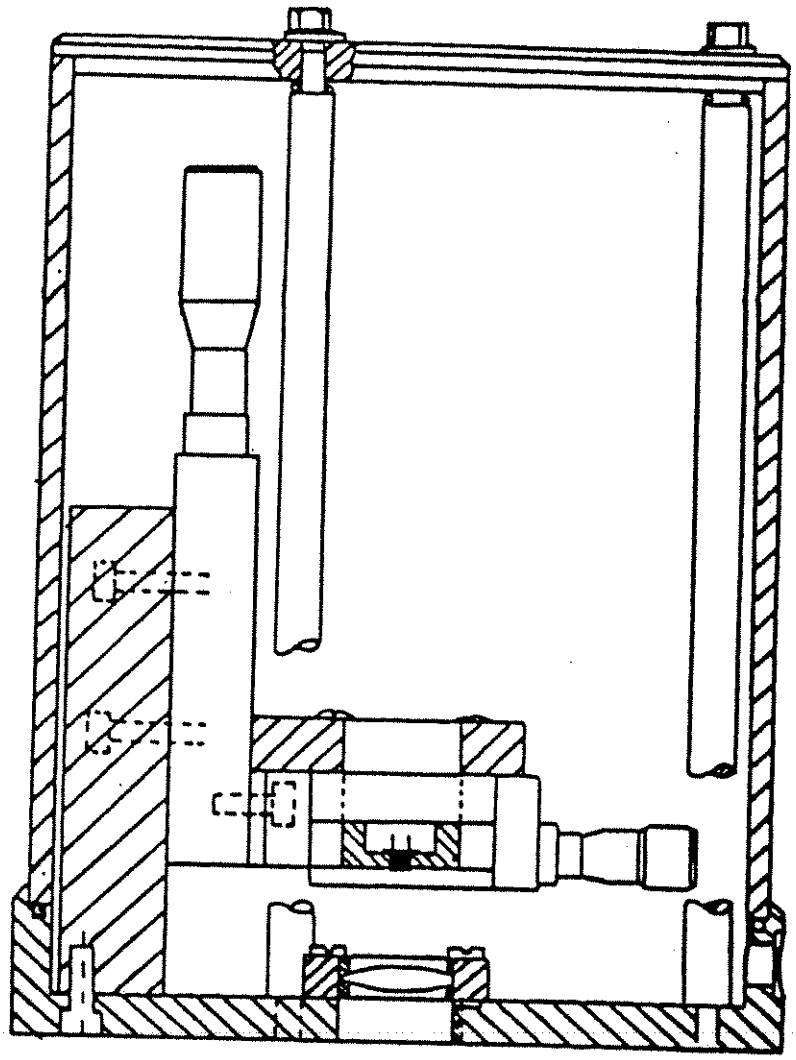

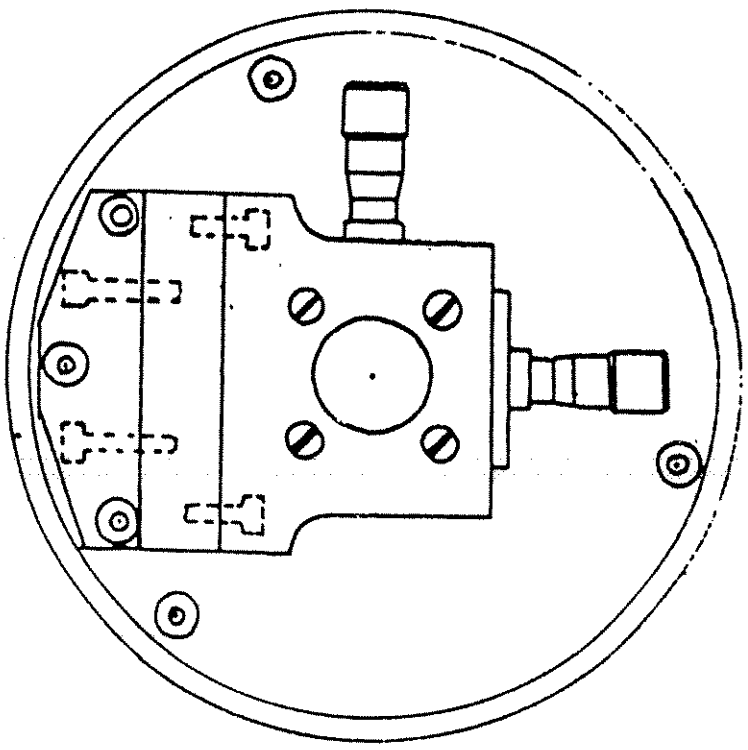

Fig.: 3 Cross-section of the housing of the avalanche diode

The APD detector RCA 30902 S

As a first approach, a suitable mount for the APD, which has a very small light sensitive area of ~ 0.2 mm^2 was made (fig. 3). A convex lens was used, to focus onto the sensitive area of the diode, which can be adjusted precisely with the help of a precision XYZ- translator table. Two different modes of operation have been examined. At first, the voltage at the APD was set to a value close to the breakdown voltage. The presence of photoelectrons are causing a fast rising current, which soon drops to zero as all the electrons are removed from the neutral region by the strong external electric field. This results in short pulses of a few millivolts in amplitude, the signal was adjusted in level by a low noise broadband amplifier (20 dB Avantek 10 - 1000 MHz) and is fed to a constant fraction discriminator (Tennelec TC 454). The Geiger mode (2,4) is much more sensitive and adequate for the detection of 1 to 10 photons. The voltage at the diode is raised above its breakdown voltage by roughly 100 volts and for a short time in the μsec. range only. When there is a photoelectron created in the depletion region, a fast rising pulse of several hundred millivolts is obtained, which always shows the same risetime characteristics and amplitude. However, as long as the externally applied voltage stays above the break-down level, the initially high current at the semiconductor drops down to a constant level. For the measured voltage at the APD this time dependent behaviour is sketched in fig. 4. To reactivate the diode, the external applied voltage must drop below the breakdown level again, which happens at least at the end of the applied gate pulse. The maximum timeduration of the gating voltage, is given by the probability of injecting an unwanted electron into the diode depletion region for example by thermal effects. At room temperature this time interval is roughly around 5 μsec for the RCA 30902 S. Both the risetime and the uncertainties caused by jitter effects, were found to be well below 1 nsec.

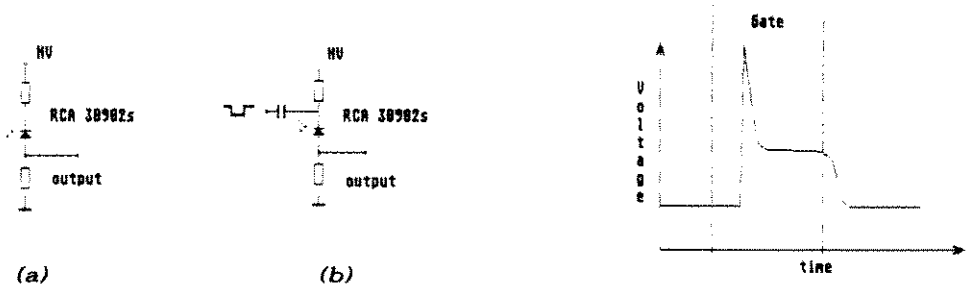

figure 4: The APD operated below the breakdown voltage level (a) and in the Geiger mode (b). The characteristic voltage- time relation is shown in principle

Experimental Setup and results

The detector housing was mounted to the receiver port in line with the optical axis and a low voltage of about 20 V was applied to the diode. The lightsensitive region of the APD was exposed to the attenuated light pulses of the laser' s oscillator coming in via the receive path. Using the XYZ- translator, the obtained signal was adjusted to the maximum in amplitude. The fact that the sensitivity of the detector was reduced for some hours, due to the relatively high photon input during this procedure, was taken into account.

In March 1989 EOS PTY. LTD. provided a calibration tool, which allows ranging along an optical rail in the laboratory for calibration purposes. The system's PMT, MCP and the APD in the Geiger mode were examined with the help of this tool. It turned out, that the MCP and the APD showed quite similiar results with less than 100 psec standard deviation per 100 measurements for the stability of the round trip times obtained. The PMT was not better than 0.5 nsec. An exact quantification has to follow, when the construction phase of the WLRS is completed. The same experiment carried out for the APD operated on the fundamental frequency of the Nd:YAG Laser gave the same results. Shortly afterwards, measurements have been carried out, to range to a groundtarget 1,2 km away from the station. Laser pulses of ca 150 psec. duration containing an energy of $\sim$ 0,1 mJ at a wavelength of 1,06 μm were transmitted, using the Carl-Zeiss-telescope. Since the startdetector of the WLRS is not sensitive enough at this energy level, a BPX65 photodiode was used as a compromise. The APD was driven below the breakdown voltage. The start- and stop events were directly fed into a Time Interval Counter HP 5370B. Out of 500 measurements, there were 372 valid responses, showing a standard deviation of $2.87 \cdot 10^{-2}$ m for the double distance. This result must be considered a worst case estimate, since no use was made of the receiving electronics of the WLRS.

After the installation of the WLRS has been completed, the characteristics of the APD (and other types) will be studied quantitativeiy and with respect to the "classical" detectors, such as PMT and MCP. It is our goal to make the WLRS at Wettzell operational both at the second harmonic, as well as at the fundamental frequency of the Nd:YAG laser. In particular, the simultaneous use of both frequencies is being considered.

Summary:

The avalanche photodiode RCA 30902 S has been tested as an additional detector for the new laser ranging system in Wettzell. The objective of these tests has been to investigate the use of its capabilities in the infrared spectral range. The results obtained show a resolution in time which is about the same as that of a micro-channel plate. With regard to the photosensitivity, quantifications still need to be done, when the installation of the whole system has

been completed. However, it seems, that the RCA 30902s can be operated at the single photon detection level. A fast risetime and a reproducible characteristic response seem to qualify the APD for ranging purposes over a broad spectral range. Ranging measurements to a nearby groundtarget showed the same result for the two different wavelengths (1,06 μm and 0,53 μm).

This work has been carried out within the frame of the work of the "Forschungsgruppe Satellitengeodäsie".

References:

(1) EOS PTY. LTD.: "Hardware Design Manual, WLRS"
(2) Application and Datasheet Avalanche Diode RCA 30902 S
(3) Hamal et. al.: Single Photon Solid State Detector For Ranging At Room Temperature
(4) J. F. Margin (CERGA): private communications
(5) G. Kirchner (Graz): private communications

COMPARISON OF THE THEORETICAL AND MEASURED PROPERTIES FOR AVALANCHE PHOTODIODE

Z. Neumann

Astronomical Institute
Czechoslovak Academy of Sciences
telephone: (204) 85201 telex: 121579

ABSTRACT

Theoretical analysis of time properties for avalanche photodiode is performed. Concrete values are computed for RCA c30921s. The measured values are compared with these theoretical ones. Recommendations are written in conclusion.

Comercial silicion APD usually consists of absorption and avalanche layer, as for example RCA c30921s.

A photon falls into the photodiode and penetrates through the absorption layer. In some place it is absorbed. The depth of this place in the absorption layer determinates the transit time (due to the different velocity of photon and electron).

The transit time through the absorption layer tabs can be calculated as

$$tabs = tp + te$$

where tp is the photon transit time and te is electron t.time.

$$tp = xa \,.\, (nsi/c)$$

where xa is the depth in abs.layer, where the photon is absorbed, nsi is the refractive index and c is light velocity

$$te = (da - xa) \,.\, K \,.\, T^{2.6}$$

where da depth of the absorption layer, K is material constant independent on the temperature and electric field (saturated velocity) and T is absolute temperature.

The average transit time and its jitter depends also on the absorption probability with respect to the depth in absorption layer. Absorption probability R can be calculated as

$$R = a \,.\, \exp(-a \,.\, xa)$$

where a is absorption coefficient, see fig. 1 . To include the recombination process, R is multiplied by a factor f

$$f = (1 - ku) \,.\, \frac{da - xa}{xa}$$

where ku is photodiode quantum efficiency.

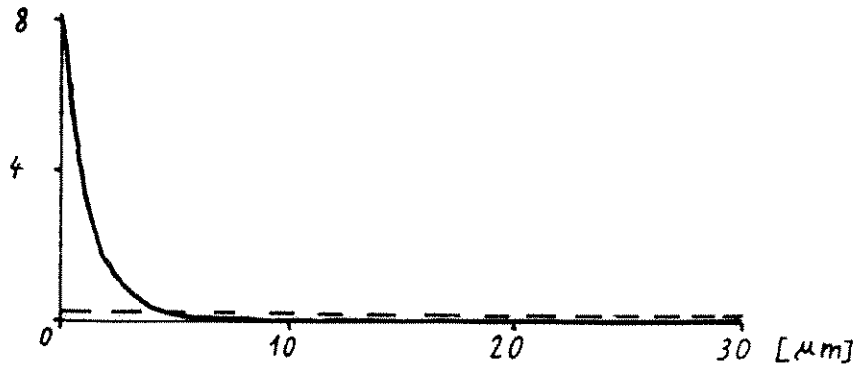

Fig. 1 Absorption probability with respect to depth in absorption layer. —— 530 nm, --- 1060 nm.

The average transit time att can be calculated as

$$att = \frac{\int_0^{da} tabs \cdot R \cdot f \cdot dx}{\int_0^{da} R \cdot f \cdot dx}$$

and jitter rms as

$$rms = \frac{\int_0^{da} (tabs - att)^2 \cdot R \cdot f \cdot dx}{\int_0^{da} R \cdot f \cdot dx}$$

The concrete values for 30 μm silicon absorption layer are writtin in tab. 1 . The saturated velocity for electrons is expected.

T [K]	att [ps]	rms[ps]
253	307	14
233	248	12
212	194	9

Tab. 1 Transit time and jitter with respect to temperature for absorption layer.

Impact ionization is the basic phenomenon for multiplication of electrons and holes in avalanche layer. Since the probability for a scattering collisions is much greater than for an ionizing collision, the ionization coefficients decrease with increasing temperature and the avalanche gain also decreases for a given electric field. According to the lit./1/ , the formulas for hole (α) and electron (β) ionization coefficients can be written

$$\alpha = 6.2 \times 10^5 \times \exp(-(1.05 \times 10^6 + 1.3 \times 10^3 \times t)/E)$$

$$\beta = 2.0 \times 10^6 \times \exp(-(1.95 \times 10^6 + 1.1 \times 10^3 \times t)/E)$$

where t is temperature in degrees of Celsius and E is electric field in V/cm .

The avalanche amplification can be described in three cases; near down, near over and far over the breakdown voltage.

In the case of near down breakdown voltage, the avalanche diode operates as a linear amplifier. An electron reaches energy high enough to cause ionization after some hunderds scattering collisions. As the ionization coefficient for electrons in silicon is much greater than for holes, only electons are able to cause impact ionization. Resulting gain reaches up to 500 or more.

In the case of near over breakdown voltage, also some holes reach energy high enough to cause impact ionization. Electrons originated by this ionization initiate the train of further ionizations. This positive feed-back realizes growing of the charge and current. Two negative feed-backs take part in process, too. Arised electons and holes performed electric field decreasing internal electric field and current of the diode decreases voltage over the diode. The duel between this feed-backs determinates resulting diode current. As the impact ionization is very random process, resulting current has also very random time behaviour, in this case.

In the case of far over the breakdown voltage, most of holes cause impact ionization, too. Originated electrons initiate the trains of further ionizations and originated holes cause new ionizations. This strong positive feed-back creates in short time (theoretically only 3-4 loops) great charge decreasing internal electric field down the threshold level. In this case the diode current is determined by external electric circuit (serial resistance and inductance and parasitic capacitance).

Using simple modeling the value of approximately 10 ps for avalanching grow was computed. The voltage two times breakdown and thickness 3 μm for avalanching layer was expected.

Measured Values

Dependence of transit time and jitter on trigger level, temperature and voltage was measured for RCA c 30902 s . Drawing of the electric scheme is in Fig. 2 . Cables were connected directly to HP 5370 B counter.

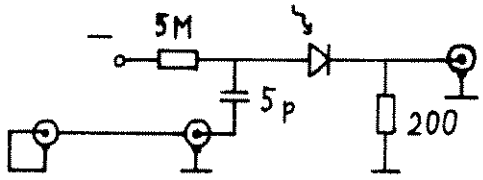

Fig. 2 Electric scheme

Dependence of transit time and jitter on trigger level is drawn in Fig. 3 .

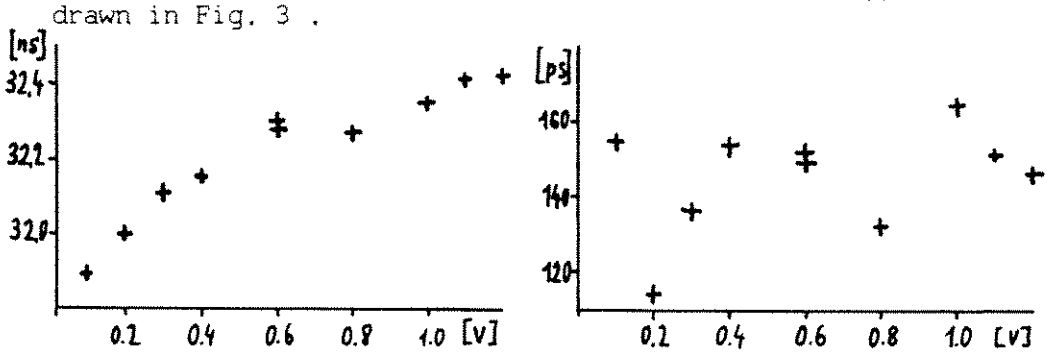

Fig. 3 Transit time and jitter dependence on trigger level

Original reason of this measurement was determination of photodiode pulse front shape. I think that Fig. 3 shows more apmlitude dependence of HP 5370 B than real front shape of pulses.

Dependence of transit time and jitter on temperature is drawn in Fig. 4 . Deconvolution of the amplitude decreasing is not included.

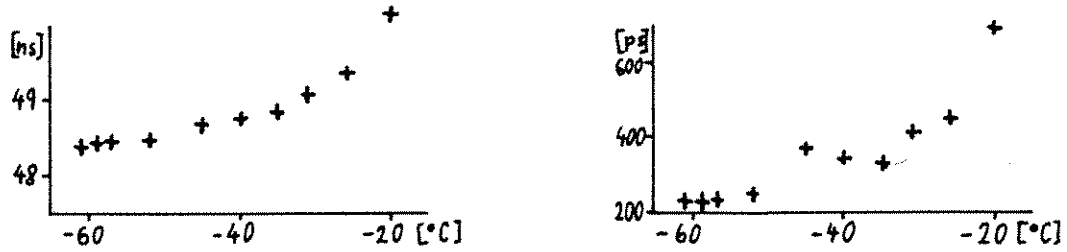

Fig. 4 Transit time and jitter dependence on temperature

Dependence of transit time and jitter on voltage is drawn in Fig. 5 . Example of 4 histograms used for determination of this dependence is in Fig. 6 .

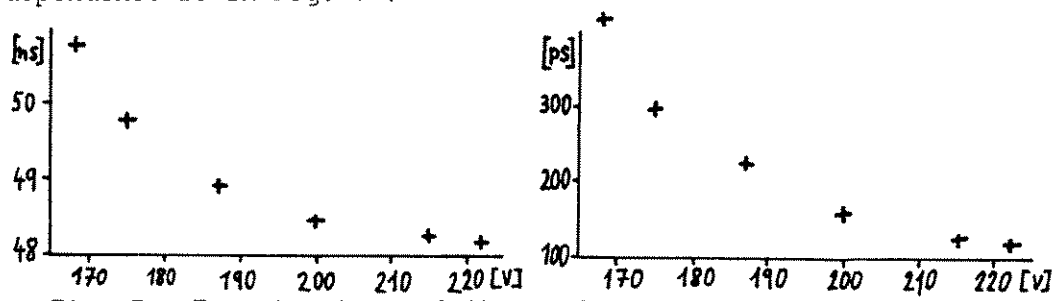

Fig. 5 Transit time and jitter dependence on voltage

Dependence of pulse width on the voltage is drawn in Fig. 8 . The electronic scheme for this measurement is drawn in Fig. 7 . The measurement was realized with 350 Mhz oscilloscope PM3295 on

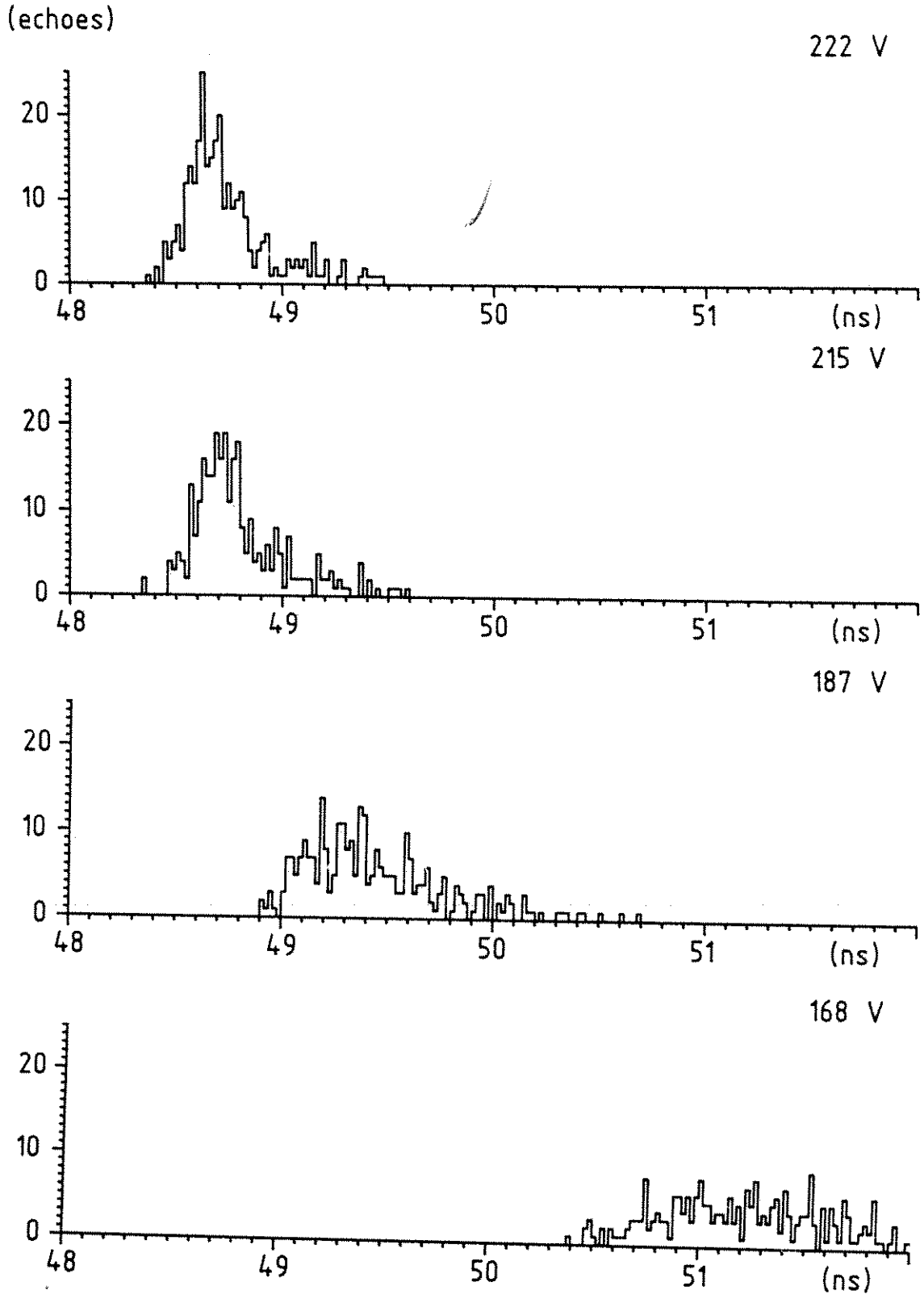

Fig. 6 Histograms

RCA c 30921 s , temperature from -60 to -65 degrees of Celsius.

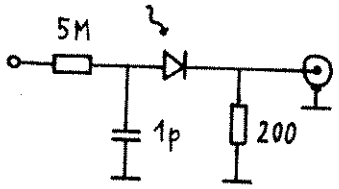

Fig. 7 Electric scheme

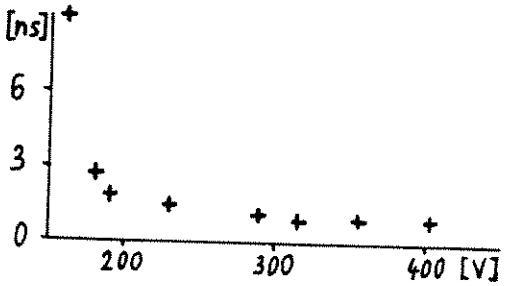

Fig. 8 Pulse width dependence on voltage

Conclusion

It would be better to use avalanche photodiodes with thinner absorption layer (approximately 3 μm) for green to reach lower jitter and higher quantum efficiency.

Comercial avalanche photodiodes as RCA c 30902 ought to reach low jitter of order 20-30 ps using high voltage (approximately two times breakdown) and electric circuit with short time constant and low impedance.

Acknowledgement

The author is indebted to Dr. R. Neubert, Dr. L. Grunwald and others from Potsdam Observatory for enabling and cooperating to obtain most of used data.

Literature

/1/ Tsang.W.T.: Lightwave Communications Technology, Photodetectors. Vol.22. New Jersey, 1985. Russ.tr., Moskva 1988.

Multiple wavelengths ranging

TWO WAVELENGTH RANGE DIFFERENCE JITTER LIMIT

I.PROCHAZKA, K.HAMAL, H.JELINKOVA

Czech Technical University
Faculty of Nucl Sci and Physical Engineering
Brehova7,115 19 Prague
Czechoslovakia

Telex 121254 fjfi c
Phone +42 2 848840

General

There is a considerable interest to provide subcentimeter laser ranging to ground targets and to satellites, as well. To determine the atmospheric dispersion, the time interval between the received signals at different wavelengths has to be determined within 1-3 ps [1] depending on the pair of wavelengths we have chosen in a particular experiment. We were providing several experiments to optimize the color pair with respect to existing high power solid state lasers and to existing photodetectors,as well (0.53/0.35um [2], 0.53/0.68um [3], 1.06/0.53um [4]).

Goals

Here we are reporting on the experiment to determine the two color delay measurement jitter as a function of the laser pulse duration and to measure the atmospheric dispersion of the 100 meters horizontal path. To determine an ultimate limit for ranging, avoiding atmospheric propagation fluctuations, this experiment was carried out in an indoor configuration.

Experimental setup

To get various pulse duration, several laser oscillator configurations have been used. In the first one, the Nd:$YAlO_3$ laser was mode-locked using the ML51 [5] and Q5 dyes, Fig.1. The pulse duration was 8.7+-1.5 psec on the fundamental and 8.1+-1.2 psec on the second harmonic. However, to optimize the dyes transmission and to get day by day reproducibility, this configuration was not acceptable for desired field operations. In the second experiment, avoiding Q5 dye and optimizing the gain and dye absorption, the mean pulse duration

was 11 psec at 1.08 um. To increase the pulse duration up to 240 psec an appropriate resonant front reflector has been chosen instead of the glass wedge. To avoid the walkoff of the second harmonic beam, the $LiNbO_3$ crystal at noncritical matched angle has been chosen [5]. To avoid the pulse distortion due to the crystal dispersion, the crystal was one millimeter long. In such a setup the both wavelengths are collinear what is a critical task for far targets two color ranging. Additionally, to avoid pulse shape distortion of the fundamental wavelength pulse, the conversion efficiency was kept low.

Streak camera system

The IMACON 500 linear sweep streak camera equipped with the soviet provience tube PV-001 / S1 [4] having the ultimate temporal resolution better than 1.5 picosecond has been used.The camera was interfaced to the TV readout consisting of the SIT vidicon, the video grabber 256x256x8bits and minicomputer. The sweep nonlinearity and the speed has been carefully calibrated and software compensated. The sweep speed 30mm per millimeter was used for laser pulses shorter than 100 psec,what turns to 1.68 picosecond per channel. The sweep speeds 100 psec/mm and 200 psec/mm were used for laser pulses length of 100 psec and 240 psec, respectively. These settings were found to give the lowest jitter in the two color delay measurement.

The streak input optics is imaging the slit on separate places for each color,and in this way an independent streak records are obtained for both colors in each shot. Due to the chromatic aberration of the optics involved the pulse record is slightly broadened.- The streak record of indoor ranging is on Fig. 2. The two color time delay is evaluated from the maximum of the convolution function of the two readings. As the both readings are smooth functions, the maximum position of the convolution may be precised by means of polynomial fitting of the convolution function values near the maximum. In this way, the time delay of the two colors may be determined with the resolution of fraction of one readout channel.

Results

Ranging the indoor target at the distance 2 meters,the results are summarized on Fig.3. Each cross represents the measurement of 100 shots. The curve shows the ultimate limit of the jitter of the two color ranging versus the pulse duration. The real ranging results are expected to appear above this line due to several additional disturbing factors - temporal / angular relation [6], the atmospheric turbulence, retrotarget characteristics and others.

Ranging to the outdoor target at the distance 102 meters, the two color time delay jitter was 1 psec. Taking into account the 2 meter indoor two wavelength time delay, the dispersion of the 100m external atmospheric path was measured to be 10.4 psec, while the theoretical value of the dispersion was about 9 psec. The source of such a discrepancy is unresolved, probably, it is caused by the swepp speed and linearity temporal and tempearature dependence.

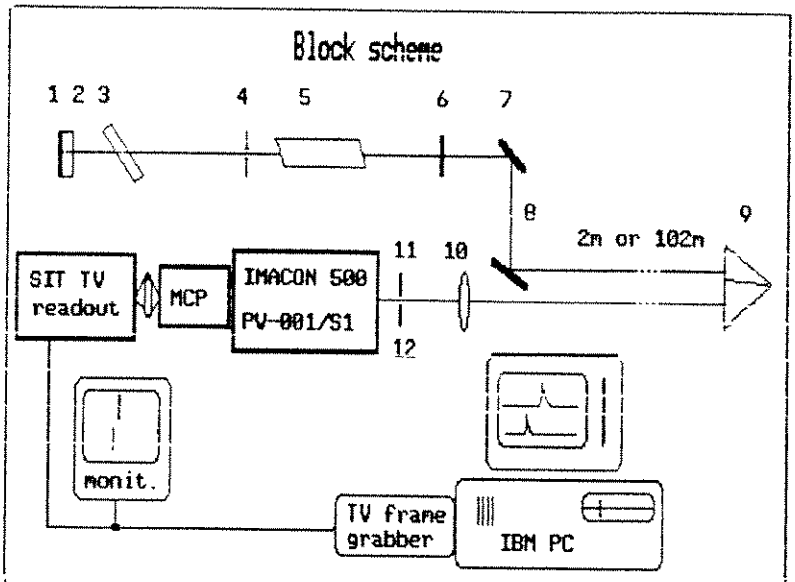

1 rear HR flat mirror

2 contact dye cell,ML51 dye

3 brewster angle dye cell QS optional

4 aperture

5 Nd YAP 4x75mm in pump.head

6 front mirror * wedge shaped for the shortest pulses

* variable thickness etalon

7,8 HR flat mirrors

9 corner cube diam. 50mm

10 collecting optics

11 filter transmitting 1.08 nm only

12 filter transmitting 0.53 nm only

Fig. 1

Literature

[1] J.B.Abshire,Applied Optics,Vol.19,No20,3436-3440 (1980)

[2] K.Hamal,I.Prochazka,J.Gaignebet,Proceedings of the Fifth International Workshop on Laser ranging Instrumentation, Herstmonceux Castle,published in Bonn,(1985)

[3] J.Gaignebet et al.,Proceedings of the Sixth International Workshop on Laser Ranging Instrumentation, Antibes, edited by J.Gaignebet (1986)

[4] K.Hamal et al.,Proceedings of the 18 Congress on High Speed Photography and Photonics,Xian,China,SPIE,1988

[5] Ji. Kvapil, et al.,proceedings of CLEO' 87,60 (1987)

[6] I.Prochazka et al., Streak camera as a laser radar receiver, its performance and limitations,in [3]

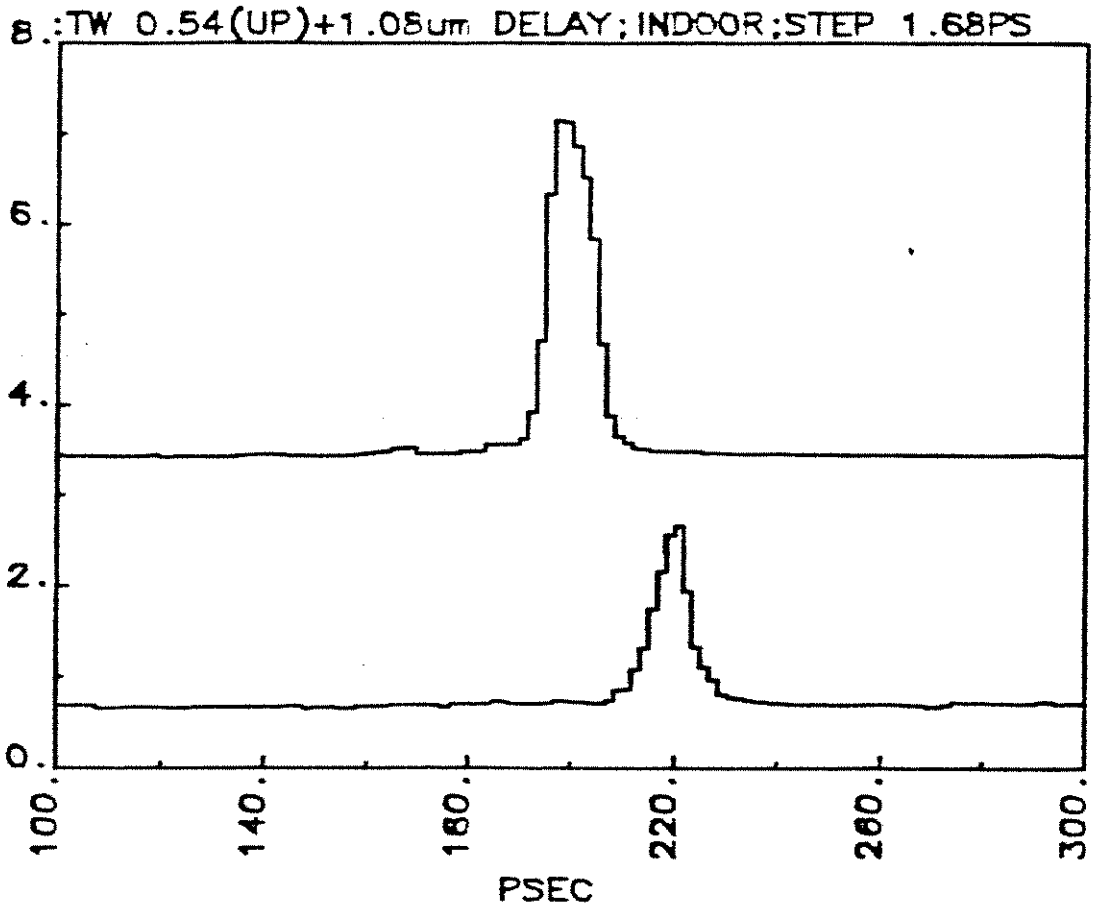

Streak record of two wavelength 1.08/0.54um indoor ranging Fig.2

Two color time delay jitter limit
versus the pulse length

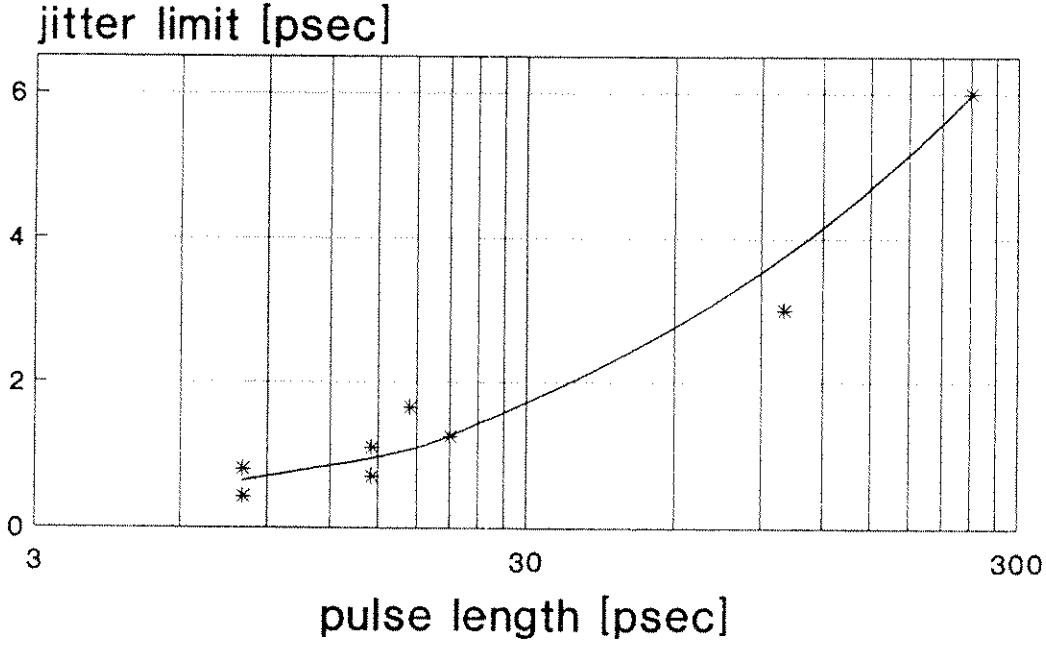

Fig. 3

MODULAR STREAK CAMERA FOR LASER RANGING

K.HAMAL, I.PROCHAZKA

Faculty of Nuc Sci and Physical Engineering
Czech Technical University
Brehova 7,115 19 Prague
Czechoslovakia
Telex 121254 fjfi c Phone +42 2 848840

M.SCHELEV, V.LOZOVOI, V.POSTOVALOV

General Physics Institute
Academy of Sciences of USSR
Vavilov Street,Moscow
USSR

General

There is a continuous effort to exploit the streak camera as a detector for laser ranging. As a final goal, the millimeter precision is expected. To obtain valuable data for the atmospheric correction, the multiple wavelengths ranging may be used [1]. The time interval of the returned pulses at different wavelengths (the range difference) has to be determined within several picoseconds. Considering the existing photocathodes, laser technology available and the ranging conditions K.Hamal et al [2], obtained for the wavelengths 0.53 um and 0.35 um the range difference RMS=2.5 psec, J.Gaignebet et al [3], using second harmonic of the Nd YAG at 0.53 um and Raman shifted pulse at 0.68 um, obtained the range difference RMS=1 psec. The ultimate limit for 1.08/0.54 um pair has been obtained 420 femtoseconds [4],[5].

Camera requirements

To choose the optimum sweep speed, the pulse duration and the number of detected return photoelectrons have to be considered. The existing technology of picosecond lasers restricts the available pulse duration to the range between 10-100 psec and the peak power up to 10GW/cm2. Consequently, the sweep speed between 40 psec/mm and 400 psec/mm has to appear.

To solve the problem of the streak camera, assuming the reliability required in field conditions and in space applications, both, a linear and circular scan streak camera has been treated. The advantage of the linear streak is a relatively simple readout, however the

necessity of the delay within the range of 20-30 nsec may cause several problems. On the other hand, using the circular streak, the main limitation is the maximal available sweep speed and the nonsymmetry of the deflection and consequently the complexity of the image readout and processing.

Camera construction

We developed the modular streak camera capable of both, linear and circular sweep, Fig 1. The PV-006 streak tube with S25 photocathode and the microchannel plate image intensifier fiber optically coupled together are used. The camera is equipped by the circuitry for ranging purposes, as well. For the linear deflection generator we exploited the chain of 14 avalanche transistors. At the sweep speed of 40 psec/mm, the temporal resolution of 5 psec and the range difference jitter 420 femtoseconds have been achieved. At the sweep speed 200 psec/mm, the temporal resolution of 35 psec and the range difference jitter 6 psec have been achieved. To obtain the circular sweep we applied 320 MHz RF signal, 13 Watts of pulsed RF power. The maximal RF power applicable on the deflection system is limited by the internal ionisation inside the tube. The diameter of the circle was 6 mm resulting in 155 psec/mm sweep speed. The temporal resolution was 20 psec and the range difference jitter 6 psec.

Timing and gating circuitry

The application of the streak camera for ranging purposes is accomplished by the timing / gaiting circuitry, Fig. 2. The timing of the circular version is shown. The RF deflection signal is ON for only few microseconds before laser transmition and again few microseconds before expected arrival of the satellite echo. All the remaining time the camera is working in the static mode and may be used for guiding / alignment purposes, as well. The 320MHz deflection signal is produced by multiplication of the 5MHz sine wave output of the station Cs beam clock, which simultaneously is acting as an oscillator for all the station timing electronics. This way, the phase synchronism of the radar electronics and the camera circular deflection is maintained.

The microchannel plate intensifier gain is controlled in three steps. During the laser transmition, the gain is set to minimum to avoid the blinding of the system by the atmospheric backscattered light, most of the time the MCP gain is set to 100, a compromise between the static image mode gain and the background noise contribution. At the expected echo arrival time, the MCP gain is set to maximum of 10000 for 300 usec to achieve maximum detection sensitivity.

Readout system

To readout the tube screen image we did compare the Haimann SIT camera and Proxicam Intensified CCD camera and we did not find any difference. The output signal from the TV readout was fed to the Visionetics Frame Grabber card (512x512x8bits) inserted in the IBM PC. To solve the problem of a deflection nonsymetry, the software package [6] allows the *full frame* image processing of both, the linear and

circular readings and accomplishes the software modelling of the image distortion, the sweep nonlinearity, the gain nonuniformity etc. Once the center of the deflection circle is marked by the satellite image in the static mode, the temporal/angular effect [7] may be compensated by the software.

Experimental results

The example of the circular streak record of the train of mode locked pulses is on Fig.3, the 3D image projection and the conversion of the image into the temporal curve. The sweep linearisation was not applied at this stage. The dynamical range of the circular sweep streak camera has been tested using a mode locked pulse, second harmonics Nd YAP, pulse width 12 psec FWHA. The dynamical range curve is shown of Fig.4a. The system dynamical range is affected by focussing of the input radiation on the small spot. The camera range difference jitter limit has been tested using two pulses separeted by the fixed interval. Completing a series of measurements, the sweep speed nonlinearity and the range difference jitter limit may be estimated, Fig.4b. Undulation of the curve is caused by the higher order harmonics in the driving RF wave, the dual pattern within the position 200-600 channels is caused by the subharmonics content in the driving wave. Compensating these effects, the range difference jitter of 6 picoseconds has been achieved.

References

[1] J.Abshire,Applied Optics, Vol.19,No20,3436-3440 (1980)

[2] K.Hamal,I.Prochazka,J.Gaignebet,Proceedings of the Fifth International Workshop on Laser Ranging Instrumentation Herstmonceux Castle,published in Bonn,(1985)

[3] J.Gaignebet et al.:Two color ranging on the ground target using 0.53 um and Raman 0.68um pulses,CLEO '89, Baltimore,1989

[4] K.Hamal at al., proceedings of the 18tn Congress on High Speed Photography and Photonics,Xian,China,1988 published in SPIE (1988)

[5] I.Prochazka,K.Hamal,H.Jelinkova: Femtosecond two color laser ranging to the ground target. CLEO' 89, Baltimore May,1989

[6] P.Valach : Streak camera full frame image processing. in this proceedings

[7] I.Prochazka,K.Hamal: Streak camera as a laser radar receiver,its performance and limitations. proceeding of the 6th International Workshop on Laser Ranging Instrumentation,Antibes,Sept.1986

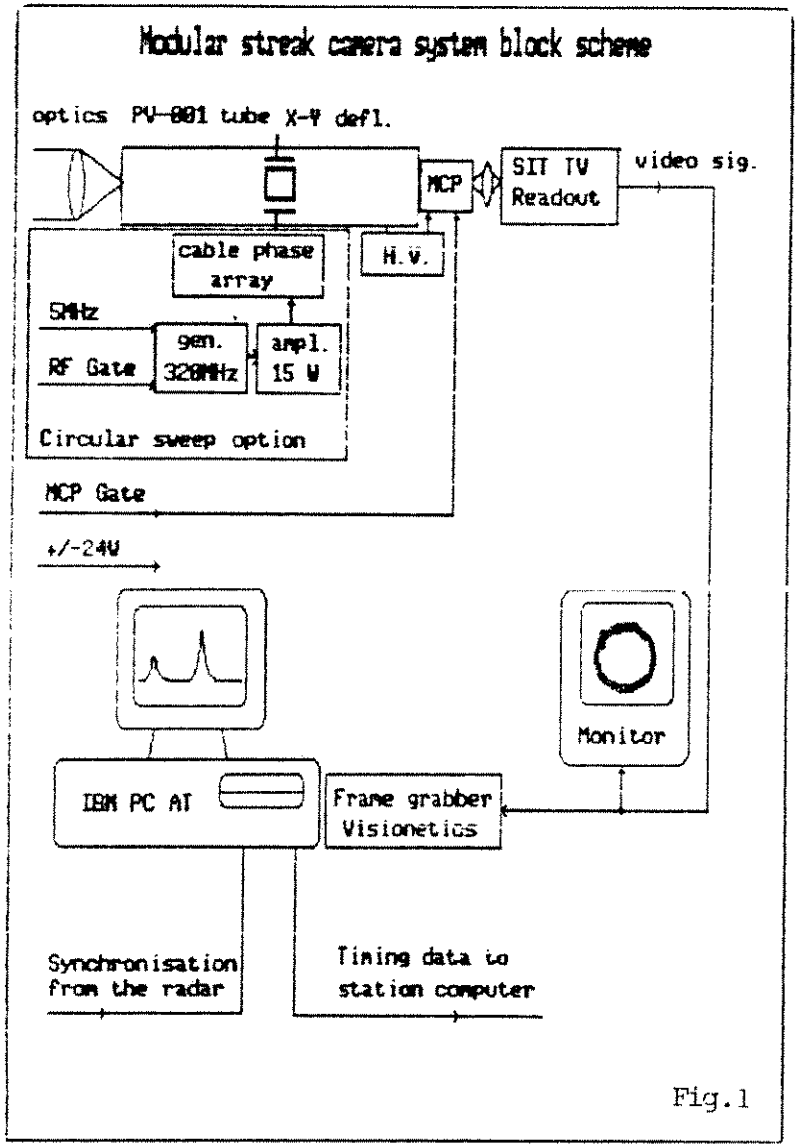
Modular streak camera system block scheme
optics PV-001 tube X-Y defl.
MCP
SIT TV Readout
video sig.
cable phase array
H.V.
50MHz
RF Gate
gen. 320MHz
ampl. 15 W
Circular sweep option
MCP Gate
+/-24V
Monitor
IBM PC AT
Frame grabber Visionetics
Synchronisation from the radar
Timing data to station computer

Fig.1

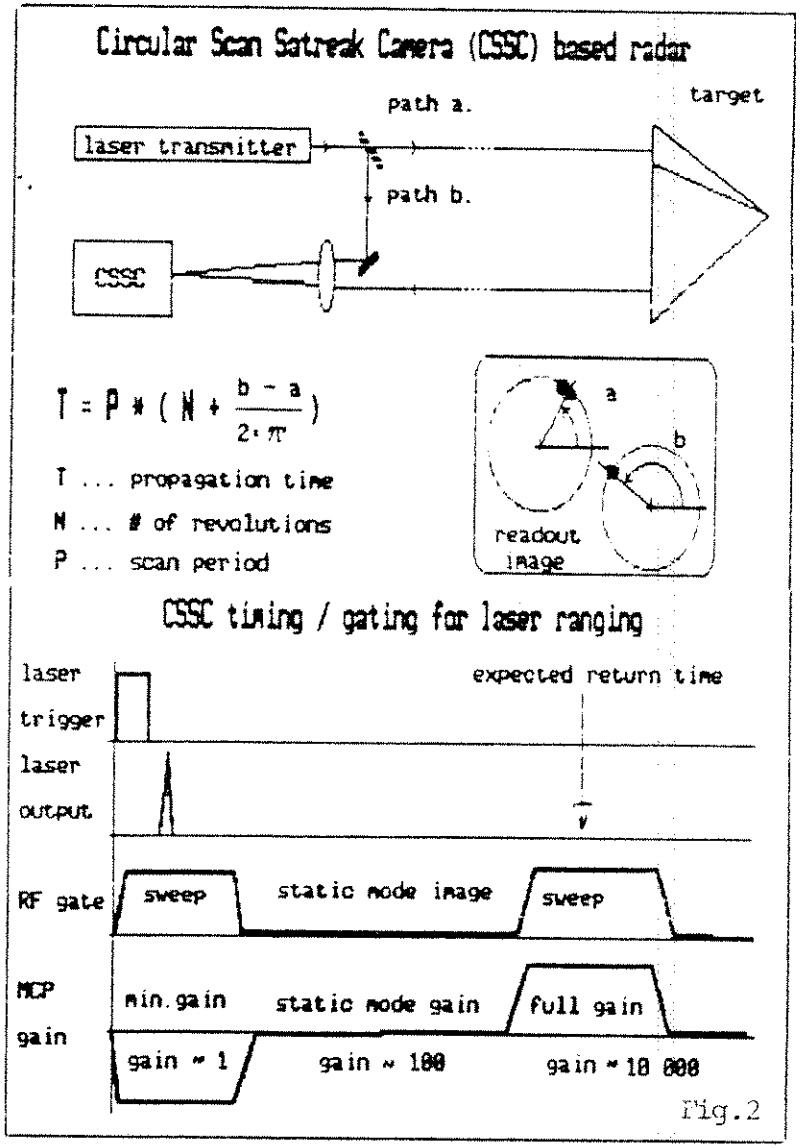
Circular Scan Satreak Camera (CSSC) based radar
path a.
target
laser transmitter
path b.
CSSC
T = P * (N + (b - a) / (2 * π))
T ... propagation time
N ... # of revolutions
P ... scan period
a
b
readout image
CSSC timing / gating for laser ranging
laser trigger
expected return time
laser output
RF gate
sweep
static mode image
sweep
MCP gain
min. gain
static mode gain
full gain
gain ≈ 1
gain ≈ 100
gain ≈ 10 000

Fig.2

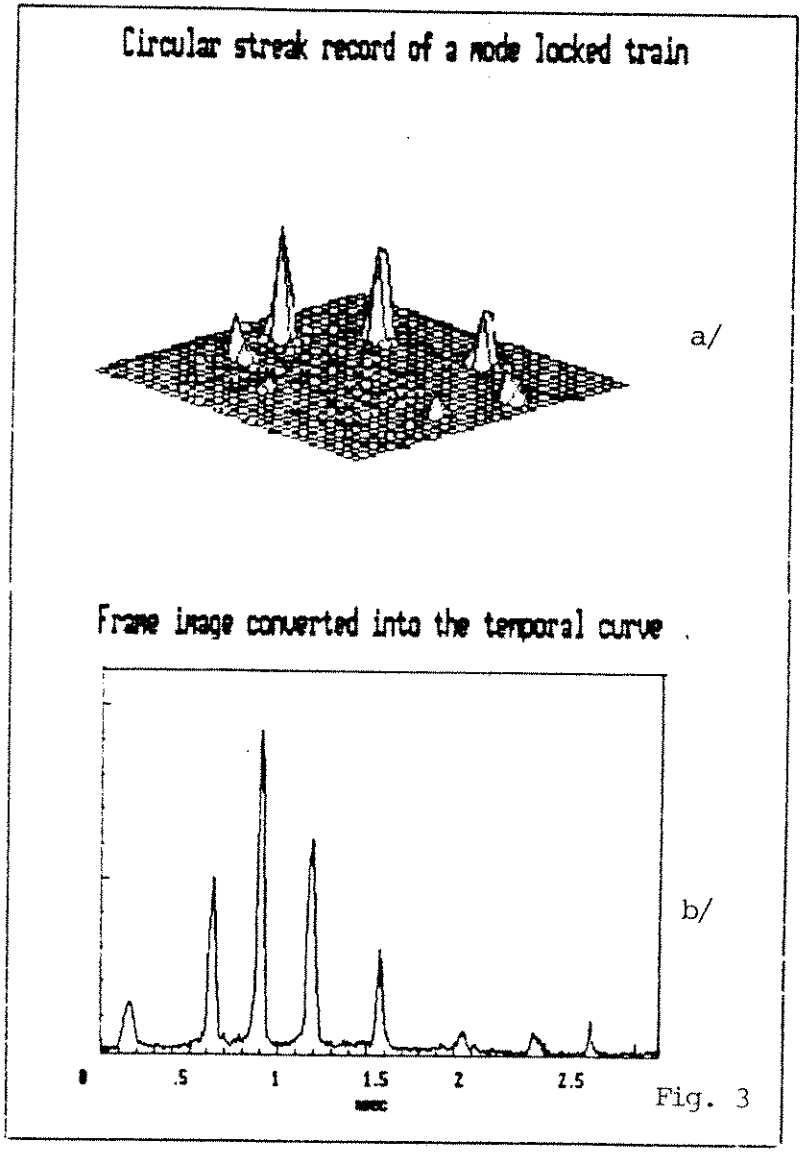
Circular streak record of a mode locked train
a/
Frame image converted into the temporal curve
b/
0
.5
1
1.5
2
2.5
nsec

Fig. 3

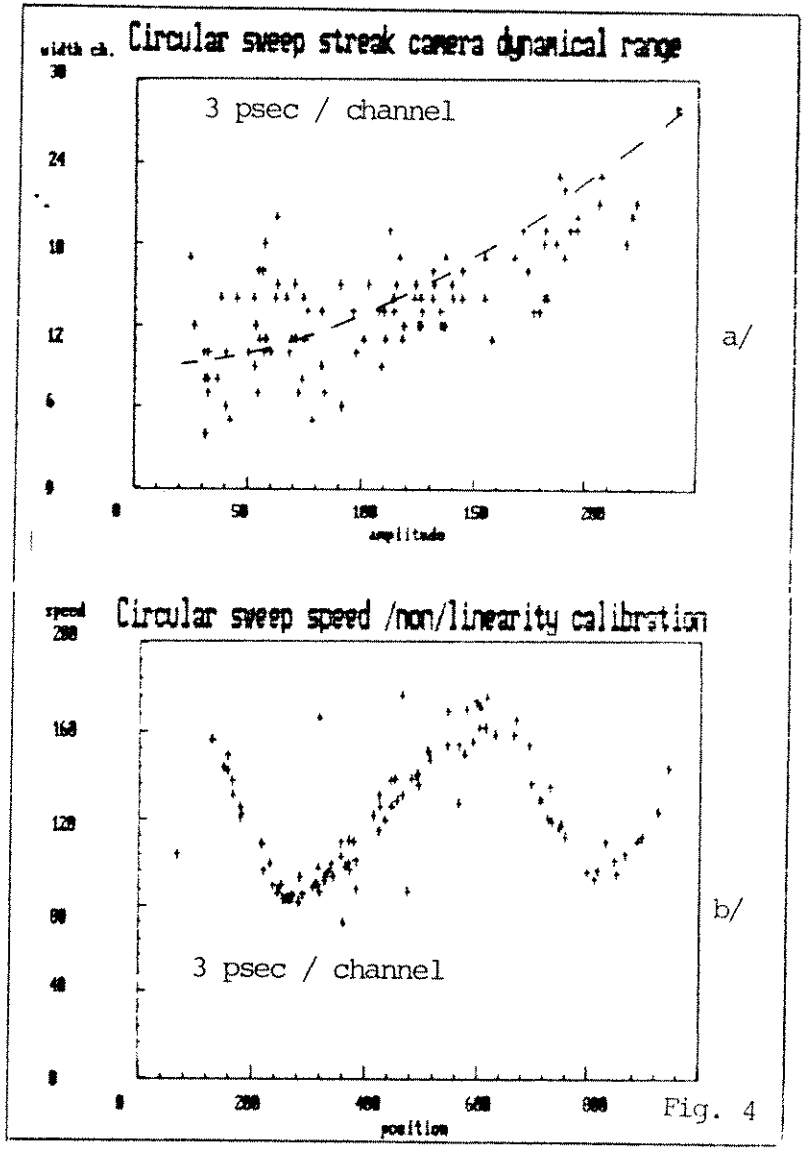
Circular sweep streak camera dynamical range
3 psec / channel
a/
0
50
100
150
200
amplitude
Circular sweep speed /non/linearity calibration
3 psec / channel
b/
0
200
400
600
800
position

Fig. 4

First two colour ranging results

at CERGA LLR station

C. Veillet

J.F. Mangin

J.M. Torre

CERGA/OCA
Av Copernic F-06130 GRASSE

1 - Why two colour ranging ?

In order to test the possibility of ranging the Moon by using the fundamental wavelength of the YAG laser, a detector package has been made (see these proceedings in 'detection' Section') with an RCA C30954 photodiode in Geiger mode. The detector package has been implemented on the telescope of the LLR station. Since the beginning of the YAG operations on this telescope, both the green and the infrared are transmitted to the Moon. When returning, the green photons are sent on an PMT, and the infrared ones go through a dichroic glass on the photodiode. Taking benefit of the multichannel event-timer, it is possible to receive returns in both the colours from a same shot.

In fact, this two-colour ranging doesn't permit any determination of the tropospheric delay, as the laser pulse length is long (300 ps), and the detectors and timing devices are not able to provide the required temporal resolution and stability. But it is a first step, even if the main goal of these studies is mainly the efficiency of the infrared ranging of the Moon.

2 - First tests on satellites ...

As a first step to the Moon, it has been decided to start ranging satellites. Among the various satellites available in the sky over Grasse, Meteosat P2 with the reflectors of the LASSO package (see the paper in the 'international cooperation' Section of these proceedings) is probably the most convenient, as it doesn't move too much (it is geosynchronous ...).

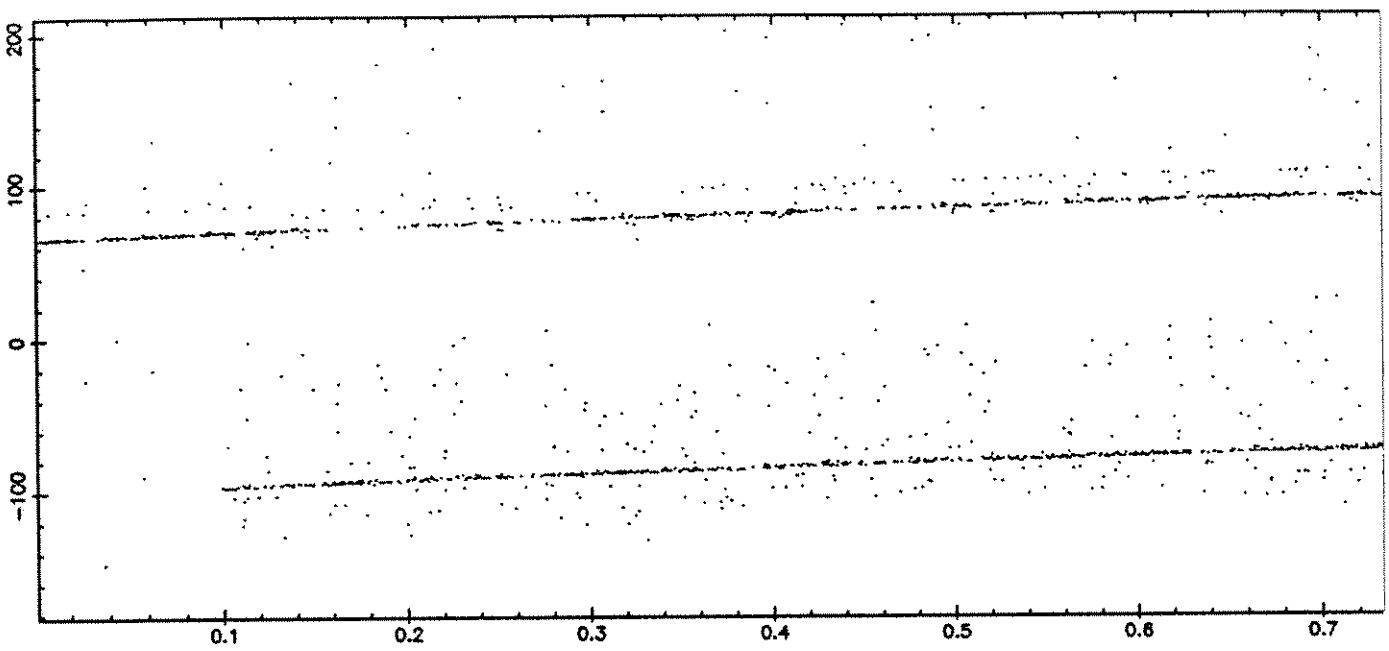

Figure .1: *Two-colour ranging session on* **Meteosat P2** *(see text for explanations)*

Fig. 1 shows echoes obtained from Meteosat. As all the plots presented here for satellites, the time is running on the x-axis (unit is 1000 seconds), and residuals on the roundtrip time are on the y-axis in nanoseconds. Every dot is an event (noise or return) detected by the PMT or the photodiode. The dotted line at the top is made from the green returns, and the dotted line at the bottom from the infrared photons. The difference in the range doesn't come from the tropospheric delay, but from different transit times in the receiving devices, cables, ...at the station itself.

Fig. 2 is another ranging session on Etalon, which efficiency as seen from the Earth is much larger, as the retroreflectors area is much larger and the satellite itself closer than Meteosat P2. The number of photons coming back is much higher than from Meteosat P2, and the pulses of the train preceding the main pulse can bee seen under the main pulse infrared returns. As the frequency doubler is not efficient at low energy, these low pulses can't be seen in green.

In order to study the sensitivity of the photodiode, a ranging session has been made, in which the laser energy has been modified. Fig. 3 shows the plot obtained. It can't be used for efficiency comparisons between the PMT and the photodiode, again because of the frequency-doubler non-linearity. The plot on Fig. 4 shows the sensitivity versus the attenuation of the transmitted beam.

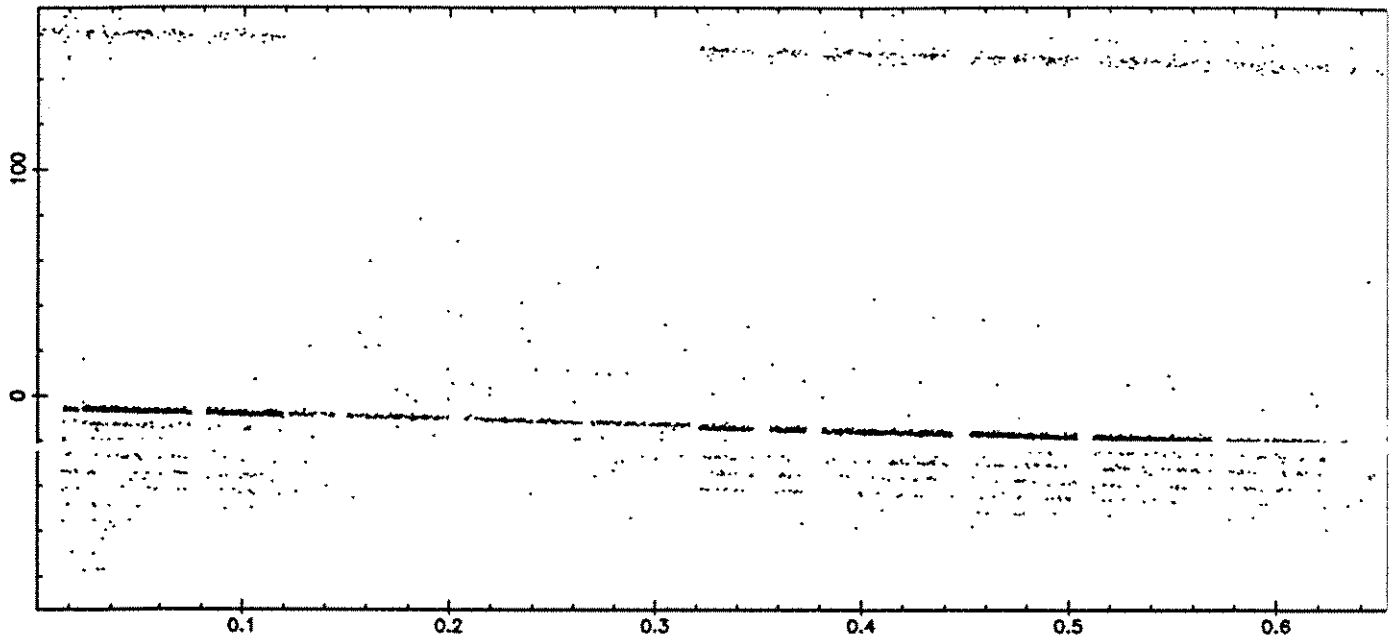

Figure .2: *Two-colour ranging session on* **Etalon** *(see text for explanations)*

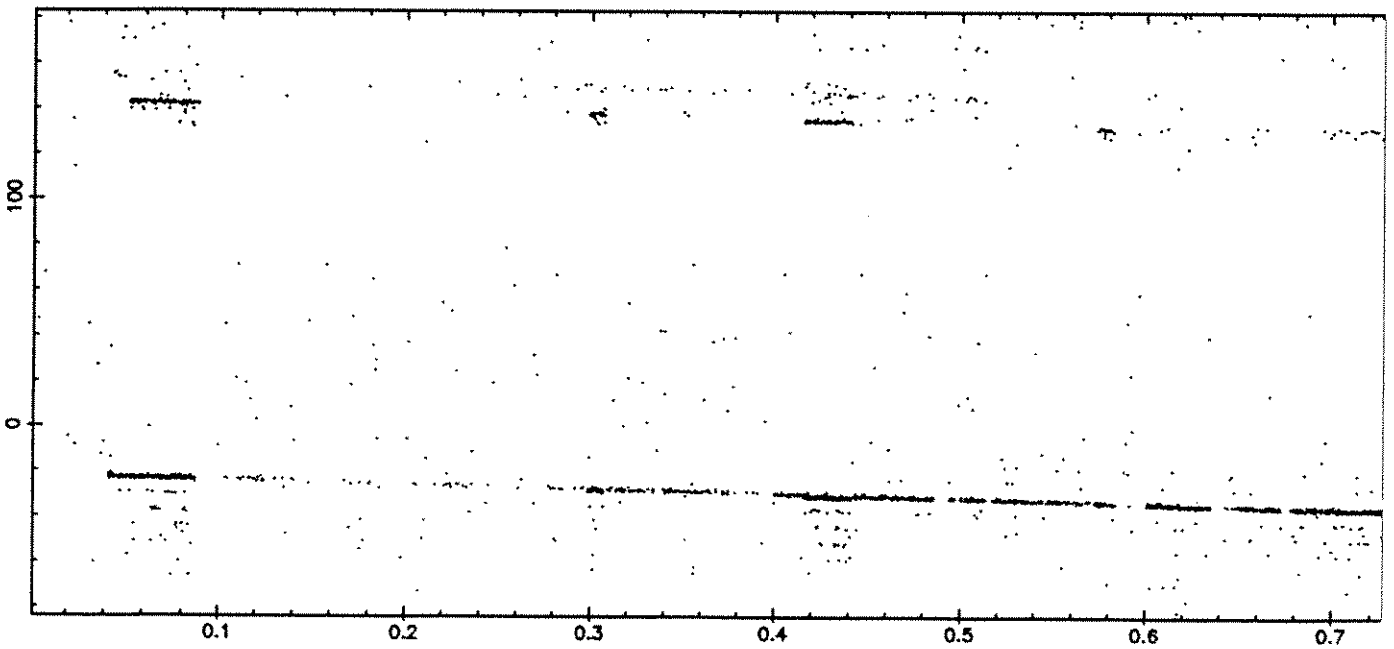

Figure .3: *Sensitivity tests on a two-colour ranging session on* **Etalon** *(see text for explanations)*

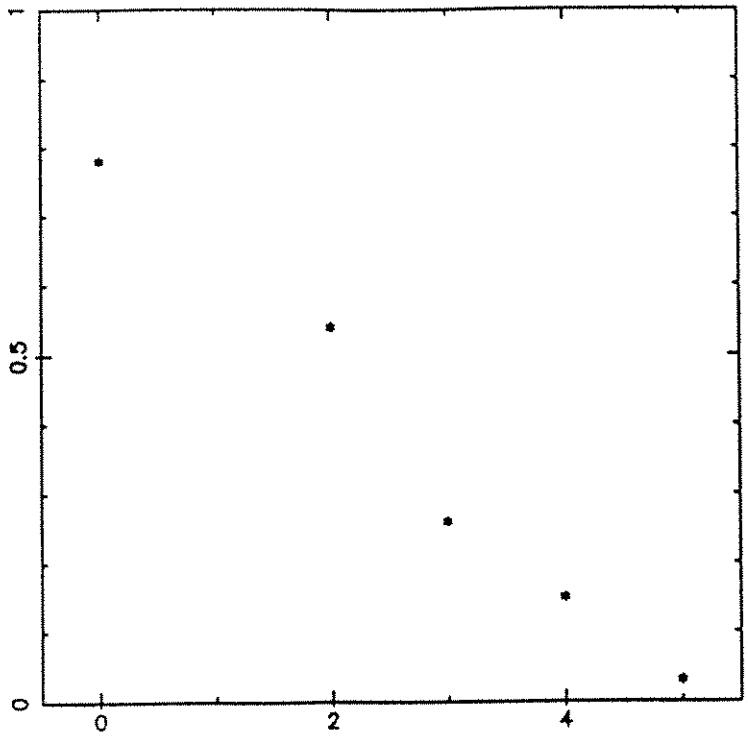

Figure .4: *Sensitivity of the photodiode (return detection per shot) versus the attenuation of the laser beam sent to* Etalon.

On another session, an enlargement has been made on the pulses of the train detected by the photodiode. Fig. 5 displays this enlargement (the time span is roughly 40 seconds), and an histogram with 1 ns bins adds the returns, and gives on the left an image of the train. The large peak at the top of the histogram corresponds to the main pulse. As the photodiode can only detect one event per gate (the avalanche started on the first event prevents for more detections), it doesn't reflect the shape of the pulse train, but its convolution with the detection probability as a function of the return energy!

Fig. 6 displays a Lageos pass over 1500 seconds with a sky not yet dark (a short time after sunset). The noise in infrared is much larger than it is in green, as the photodiode is more sensitive than the PMT, and the filter used on the infrared path not as narrow as on the green one. The train can be easily seen, and the return level is varying as the energy is changed for test purposes.

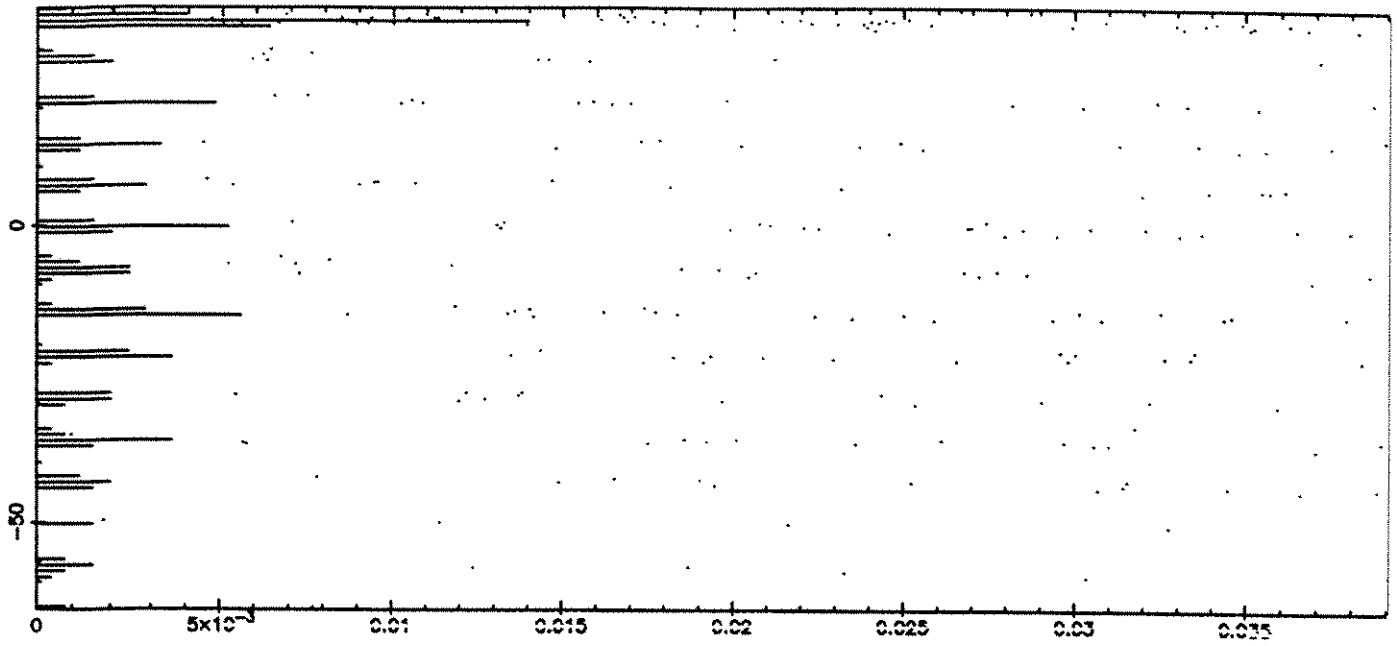

Figure .5: *Pulse train as seen on a short two-colour ranging session on* **Etalon** *(see text for explanations)*

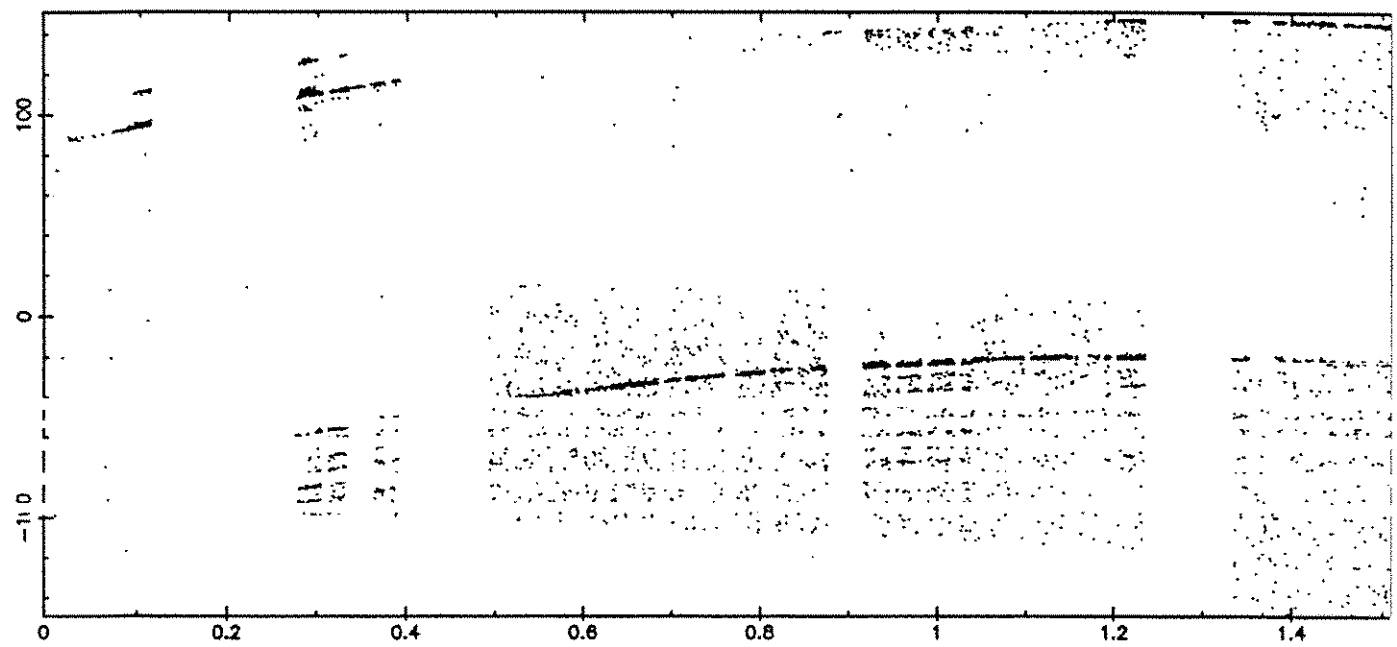

Figure .6: *Two colour ranging session on* **Lageos**.

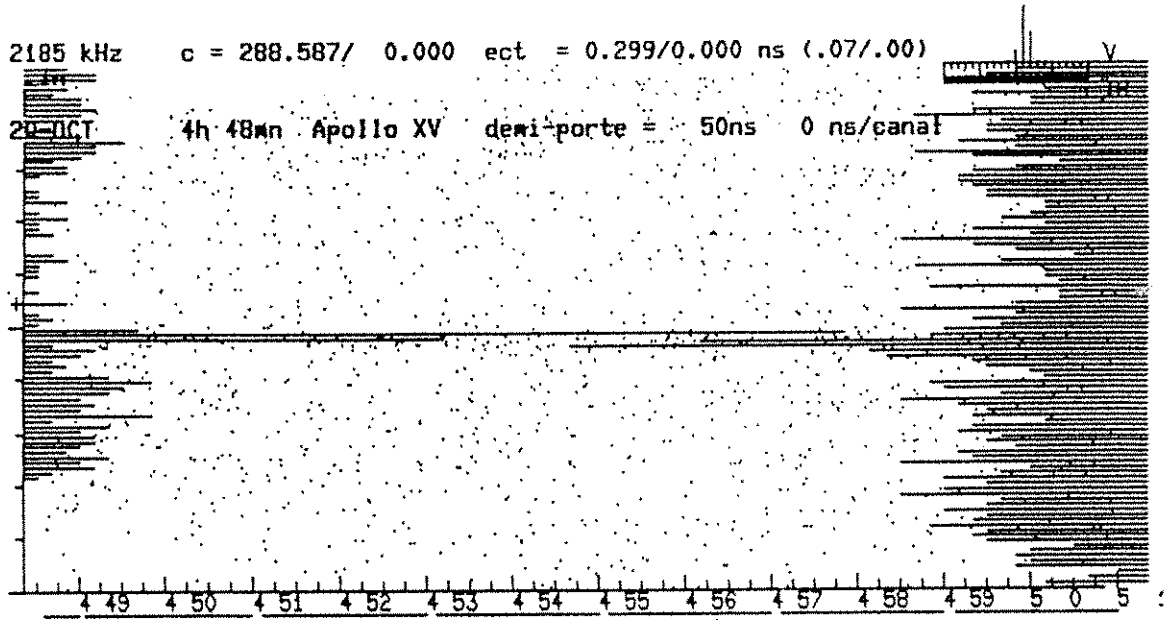

Figure .7: *A series of echoes from* **Apollo 15**. *Every dot is an event (noise or return) in the gate (+/- 50 ns) centered on the predicted range, and is green or red (on the screen, not on this copy !) according to its origin (PMT or photodiode). Time is running on the x-axis (hr mn). The histogram on the left adds the green events in 100 bins 1ns wide. On the right, another histogram does the same thing in infrared. In this series, echoes arrived in green (the large peak on the left) and in infrared (the large peak on the right).*

3 - Two colour Lunar laser ranging, now and in the future ...

After these results on satellites, the first attempts have been made on the Moon. Many series of echoes on various reflectors have been obtained, and Fig. 7 is a copy of the real-time screen displaying such a series.

These first results have to be confirmed with an extensive set of observations which will permit to check the jitters in the photodiode, and to compare the relative efficiency of the two colours. The best is still to come !...

Epoch and event timing

Single photon timing at picosecond resolution with silicon detectors

A.Lacaita, S.Cova, G.Ripamonti and M.Ghioni

Politecnico di Milano, Dipartimento di Elettronica and
Centro di Elettronica Quantistica e Strumentazione Elettronica CNR

Piazza L. da Vinci 32, 20133 Milano, Italy

Telephone (+39) 2 - 2367604
Facsimile (+39) 2 - 23996126
Telex 333467 POLIMI I

ABSTRACT

The ultimate time resolution in the timing of single optical photons is limited by the available detector and not by the electronic circuitry. The possibilities offered by silicon detectors are here discussed and investigated. Avalanche current pulses triggered in reverse biased junctions with very high electric field mark the arrival time of absorbed photons. The physics of the avalanche build-up and propagation over the sensitive area determines the resolution limits.

Theoretical studies point out the possibility of attaining resolutions of a few picoseconds. Experimental tests on specially designed silicon devices have already confirmed better than 30 ps FWHM (full-width at half maximum) resolution at room temperature, better than 20 ps with the detector cooled at -65 C.

1. INTRODUCTION

The presently available photodetectors with single photon sensitivity are either photomultiplier tubes (PMTs), or avalanche photodiodes (APDs) operating in the triggered avalanche mode biased above the breakdown voltage [1-4]. They are employed in time-correlated photon counting TCPC measurements. A parameter of primary interest in these measurements is the time resolution, currently defined as the full width at half maximum (FWHM) of the curve obtained in tests with ultrafast light pulses.

Ordinary fast PMTs having discrete dynode multiplier with electrostatic focusing give FWHM values in the range from 600 to 120 ps FWHM [5,6]. In recent

years, reliable ultrafast PMTs with microchannel plate (MCP) multipliers have been commercially available and FWHM values down to about 30 ps have been reported for them [7]. As concerns avalanche photodiodes, special devices can be designed for operating in the triggered avalanche mode [1-4,8-13], in which avalanche current pulses of standard shape and amplitude are generated by the absorption of radiation quanta. Such devices have been called SPADs (Single photon avalanche diodes) or TADs (Triggered Avalanche Diodes).

In this paper we point out the design strategies aimed at minimizing the time jitter of a SPADs. The attainable resolution turns out to depend on a number of requirements, often setting conflicting requirements. Other important parameters of the detector, such as the quantum efficiency and the noise (i.e. the dark-count rate) depend on the same quantities. Therefore trade-offs in the device design must be taken into account.

By exploiting these strategies, we were able to design detectors having better than 20 ps FWHM resolution [14].

2. SINGLE-PHOTON AVALANCHE DIODES

Single-Photon Avalanche Diodes (SPADs) are p-n junctions that operate at reverse bias above the breakdown voltage. In this bias condition, a single carrier can trigger a self-sustaining avalanche current. In case of a photogenerated carrier, the leading edge of the avalanche pulse marks the arrival time of the detected photon. The current will continue to flow until an external quenching circuit [1,3,4] lowers the bias close to or below the breakdown voltage. The voltage is then kept low for a finite hold-off interval during which the SPAD cannot retrigger. At the end of this dead time the bias is rapidly restored in order to enable the detection of another photon under well-defined conditions.

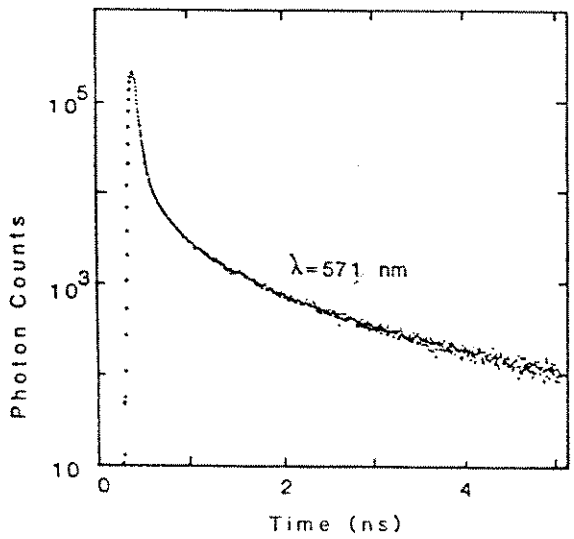

Fig.1 Typical resolution curve of a prototype SPAD device, measured with picosecond optical pulses from a cavity-dumped mode locked dye laser at 571 nm wavelength.

The avalanche can also be triggered by thermally generated carriers in the depletion layer of the active junction, that cause the inherent dark-count rate of the device. The dark-count rate is further enhanced by the presence of trapping centers in the depletion layer. In order to avoid an excessive dark-count rate, the concentration of trapping centers and generation centers must be kept low. Optimized processes with suitable gettering steps must therefore be employed in the fabrication of SPADs.

We had previously implemented and tested silicon SPAD with the geometry proposed by Haitz [1]. The response of these prototype SPAD devices is shown in Fig. 1. It is characterized by a fast peak and a slow tail. The peak is caused by the carriers photogenerated within the depletion layer of the active junction. The tail is due to carriers photogenerated in the neutral region below the active junction, some of which reach the active junction considerably delayed, after diffusion. By using a new epitaxial device structure the diffusion tail has been effectively reduced, as is elsewhere reported [10,12,15].

In order to improve the time resolution of the peak, we have studied both theoretically and experimentally the problem of the build-up and the propagation of a self-sustaining avalanche current. As a result, we achieved an improved resolution of 20 ps FWHM.

3. TIMING RESOLUTION LIMITS

The detector time resolution is due to different contributions:

(a) the carrier transit time in the depletion layer

(b) the statistical fluctuations in the avalanche build-up

The depth of the depletion region causes a first geometrical contribution to the time resolution. In fact, the avalanche process is triggered by the multiplication of the first photogenerated pair. This multiplication occurs with a statistical delay depending on the distance between the point at which the photon is absorbed and the multiplication region, at which the impact-ionization can occur. This consideration suggests that the thinner the depleted region, the better the timing resolution. The carrier saturated velocity is about 0.1 μm/ps , therefore, the devices designed to achieve the highest time resolution must have a depletion region less than one micron deep.

The contribution (a) is dominant if the multiplication reaches such high value, that the number of free carriers rises to a detectable value within the transit time of the primary photogenerated carrier. In these conditions the statistical fluctuations in the other steps of the multiplication process do not affect the the time resolution. At the operative bias, the impact ionization per carrier transit is, however, slightly greater than one, when thin space charge layers are employed. This means that the number of carriers does not increase rapidly, on the time scale of the depletion region transit time. Several transit times after the photon absorption, in the depletion region there are no more than a few tens of carriers. In these situation, the statistical behavior of the build-up process will limit the time resolution of the devices.

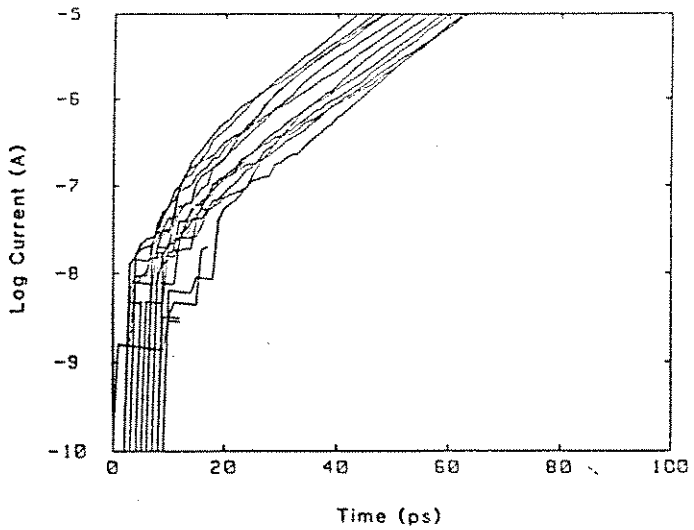

Fig.2 Simulation of the avalanche current leading edge logarithm of the current vs. time.

In order to check this hypothesis, we have developed a simplified Monte-Carlo simulation of the process. A typical result of the simulation of the avalanche current leading edge is shown in Fig. 2. The timing resolution can be inferred from the spread of the delay from the photogeneration of the primary carrier to the crossing of a given avalanche current level. The primary carriers are generated at random positions within the depletion layer. The Monte Carlo simulation takes also into account the spatial fluctuations of the electric field over the active area. These fluctuations are estimated to be $\pm$10% of the maximum electric field, and are due to technological limits in the dopants distribution.

The results of the Monte Carlo simulation were that the contribution to the time resolution due to the statistic of the avalanche build-up does not exceed 10 ps, at the operating bias conditions of SPAD devices with a depletion region one micron deep. This contribution decreases as the electric field increases. This result is physically evident. In fact, the avalanche multiplication rate increases with the electric field. Therefore, increasing the electric field reduces the fluctuations in the avalanche build-up, thereby improving the timing resolution. The Monte Carlo simulation also confirmed that the build-up statistics strongly worsens if the depletion region thickness is increased.
In order to evaluate quantitatively the dependence of the attainable timing resolution on the electric field, experiments were performed with samples having different doping i.e. breakdown voltages. Results are shown in Fig.3 for batch 3, having breakdown voltage BV=28V, and for batch 9, having BV=13V. Relevant parameters for these SPADs are shown in Table 1.

The choice of the horizontal scale, that is, the excess electric field above the breakdown one, deserves some comment. At the breakdown voltage, the multiplying region can be considered as a positive feedback amplifier having unit loop gain. In this situation the average number of carriers in the multiplying region is constant in time. Since we were comparing samples having different BV,

Table 1. Active region parameters

Batch #	Breakdown field (V/cm)	Multiplic. width (micron)	Depleted width (micron)
3	4.6×10^5	0.5	1.0
9	5.5×10^5	0.35	0.9

the normalization to the breakdown allows the performance comparison in similar multiplication regimes. The choice of the electric field depends on the considerations that the ionizations happen in the highest electric field region. Since the samples have very similar geometries of the multiplying region (a shallow diffused junction), the maximum electric field well defines the multiplication process.

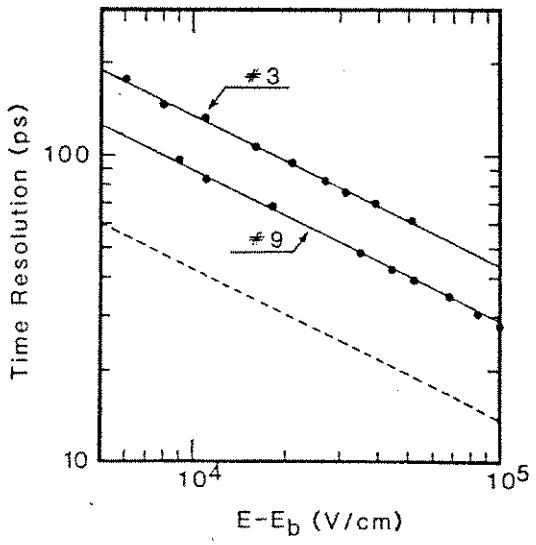

Fig.3 Dependence of the FWHM resolution on the electric field for two SPAD structures. The dashed line indicates a square root dependence.

From Fig.3 we can deduct the formula:

$$FWHM = A\ (E-E_b)^{-k}$$

where E_b is the maximum electric field at the breakdown voltage; k is 0.5 in shallow diffused junctions; A is a parameter dependent on the device breakdown voltage. It is evident from Fig.3 that a high excess field, and therefore a bias voltage well above the breakdown, strongly increases the timing resolution.

Furthermore, the operating temperature was observed to influence the observable resolution. In particular, a better resolution was observed for lower temperatures. We carried out experiments in the temperature range -60 C to +20 C by using a controlled temperature chamber. We noted the well-known temperature

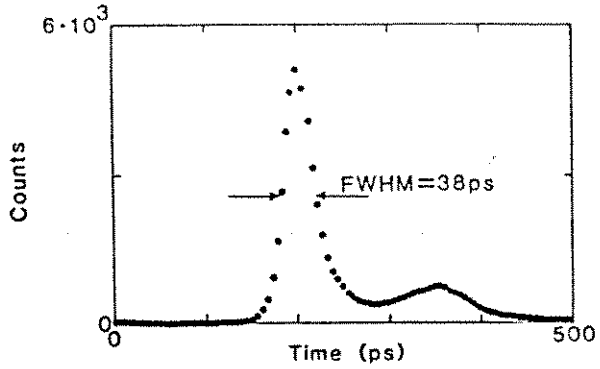

Fig.4 Measurement of the waveform of a gain switched laser diode emitting at 785 nm, performed with the epitaxial SPAD cooled at -65 C and biased at 6V excess voltage above breakdown.

dependence of the breakdown voltage, and therefore the breakdown field, and a timing resolution improvement of about 25% betweeen the two temperature extremes. The reason why this change in the attainable resolution is observed lies probably in the greater efficiency of the ionization process at reduced temperature, as compared with other energy-exchanging processes, such as optical phonon emission. Moreover, at low temperature higher bias voltages can be employed without a steep increase of the dark count rate.

The best time resolution that we measured is 20 ps FWHM (see Fig. 4). This result has been obtained in SPADs having low (13 V) breakdown voltage, that is, high breakdown electric field and thin depleted region; small area, 5 μm diameter. The operating conditions were: bias voltage 19V (limited by the steep increase of the dark count rate, above 100 kcps) and temperature of -65 C.

4. CONCLUSIONS

We have demonstrated that solid-state single-photon detectors are capable of 20 ps FWHM timing resolution. This result places these detectors at the same resolution level of the fastest available MCP-PMT. Physical quantities that allow to obtain such resolution have been investigated. From these studies, it is expected that the time resolution can be pushed to a few picoseconds FWHM.

REFERENCES

1. R.H.Haitz, *J.Appl.Phys.* **35**, 1370 (1964); **36**, 3123 (1965)
2. R.J.McIntyre, *IEEE Trans.Electron.Devices* **ED-19**, 703 (1962)
3. P.Antognetti, S.Cova and A.Longoni, *Proceedings of the 2nd Ispra Nuclear Electronics Symposium, Euratom Publication* EUR 5370e, 1975, pp. 453-456
4. S.Cova, A.Longoni and A.Andreoni, *Rev.Sci.Instrum.* **52**, 408 (1981)
5. V.J.Koster and R.M.Dowben, *Rev.Sci.Instrum.* **49**, 1186 (1978)
6. S.Canonica, J.Forrer and U.P.Wild, *Rev.Sci.Instrum.* **56**, 1754 (1985)
7. D.Bebelaar, *Rev.Sci.Instrum.* **57**, 1116 (1986)

8. S.Cova, A.Longoni, A.Andreoni and R.Cubeddu, *IEEE J.Quantum Electron.* **QE-19**, 630 (1983)
9. S.Cova, G.Ripamonti and A.Lacaita, *Nucl.Intrum.Meth.* **A253**, 482 (1987)
10. M.Ghioni, S.Cova, A.Lacaita and G.Ripamonti, *IEEE International Electron Device Meeting IEDM, Washington D.C., 1987 (IEEE, New York, 1987), Techn.Digest*, pp. 452-455
11. S.Cova, A.Longoni and G.Ripamonti, *IEEE Trans.Nucl.Sci.* **NS-29**, 599 (1982)
12. M.Ghioni, S.Cova, A.Lacaita and G.Ripamonti, *Electron.Lett.* **24**, 1476 (1988)
13. W.O.Oldham, R.R.Samuelson and P.Antognetti, *IEEE Trans.Electron.Devices* **ED-19**, 1056 (1972)
14. S.Cova, A.Lacaita, M.Ghioni, G.Ripamonti and T.A.Louis, *Rev.Sci.Instrum.* **60**, 1104 (1989)
15. A.Lacaita, M.Ghioni and S.Cova, *Electron.Lett.* **25**, 841 (1989)

FEW PS JITTER 100 MHZ TIME BASE FOR TIME INTERVAL MEASUREMENTS - DESIGN AND MEASUREMENTS

W.A.Kiełek, J.Jarkowski, S.Wygoda

Department of Electronics
Warsaw University of Technology
Warsaw, Poland, 00-665

Telephone 48 22 253929
Telex 813 307 PW PL

ABSTRACT. The report describes the design of 100 MHz time scale source of few ps jitter. Measurements methods used here were: direct measurements of multiplied by 10 000 time scale deviation, and the measurements of spectral density of phase, using phaselock loosely coupled loop method, from which the time scale deviation was calculated. Measurements in the time domain allow to confirm experimentally the relation $\sigma_x = \tau\sigma_y$, where σ_x, σ_y are the time scale and Allan deviation, respectively.

1. Description of 100 MHz time scale source constructed

For time interval measurements in laser ranging there is the need to use time scale of adequate long - and short - term accuracy and stability. Long - term stability can be assured by atomic standards. Short - term stability is frequently better in quartz crystal frequency standards. To obtain sufficient time interval measuring accuracy there is the need of having clocks of 100 MHz or higher frequency. There exist the opinions [1] that for short averaging times (up to 100 ms) high frequency quartz standards (as 100 MHz) have got better stability than low frequency ones (as 5 MHz). To employ all that possibilities for the accuracy and stability we use the scheme at Fig. 1.

Rubidium frequency standard of the 5 MHz output synchronizes 5 MHz quartz standard of good quality, using 2-nd order PLL (phase lock loop) of approx. 10 s time constant. Such time constant assures the independence of short - time (up to 5 s) stability of the time scale source on short - time stability of the synchronizing atomic clock.

Frequency multipliers are the source of unwanted deter-

ministic time modulation with the frequency multiplied and its harmonics. For the frequency multiplier we use, that modulation is of the order of 1,3 ps for the 5 MHz component and 6 ps for the 10 MHz component. That values can be decreased using more filtration, for instance quartz filters. For the same purpose we use the filtration by second PLL loop working at 100 MHz. Additional opportunity obtained in such case, there is that when changing the time constant of simple single pole RC filter in that loop, there exists the possibility to move the border between averaging time ranges, for which the origins of output time scale fluctuations are 5 MHz or 100 MHz frequency standards. That allows to employ fully the best short term stability possibilities of both of them. At this moment we use 0,3 s time constant.

5 MHz and 10 MHz components of deterministic time position modulation at the output of the 100 MHz synchronised by PLL quartz standard are 0,4 and 0,18 ps, respectively.

2. Spectral analysis of the voltage in PLL loop

Below are summarized the useful relations between some parameters, as spectral densities of: phase S_ϕ, relative frequency offset S_y, deviations: Allan σ_y, time scale σ_x, frequencies: Fourier f, nominal ν_o, and u_1, PLL phase detector voltage in the B Fourier frequency band. K_d is the phase detector gain, τ is the averaging time, T is the measurements repetition period.

$$S_y(f) = S_\phi(f) \cdot f^2/\nu_o^2 \; ; \quad S_\phi(f) = u_1^2/(B\,K_d^2)$$

$$\sigma_y^2(\tau) = \frac{2}{\pi^2}\int_0^\infty \frac{S_y(f)}{(\tau f)^2}\, W\, df \; ; \quad \sigma_x^2(\tau) = \frac{2}{\pi^2}\int_0^\infty \frac{S_y(f)}{f^2}\, W\, df \qquad (1),(2)$$

$$\sigma_x^2(\tau) = \frac{9{,}65}{K_d^2\,\nu_o^2}\int_0^\infty \frac{u^2(f)}{f}\, W\, df \qquad (3)$$

In (3), u it is the PD output voltage in the 2,1% wide band of the actual Fourier frequency. In (1) ÷ (3), W it is the spectrum weighting function, equal

$$W = \sin^4(\pi\tau f) \quad \text{for the case when } T = \tau \text{ , or} \qquad (4)$$

$$W = \sin^2(\pi\tau f)\left[1 - \left(\frac{\sin 2\pi T f}{2\sin\pi T f}\right)^2\right] \text{ for the case when } T \neq \tau. \qquad (5)$$

The shape of weighting function following (4) is given at the Fig. 3. Its averaged in f value is 0,375. The value of $\sin^2(\pi\tau f)$ averaged in τf is 0,5.
There exists the possibility to measure spectral density of phase fluctuations $S_\Phi(f)$ of synchronised by PLL oscillators, via the measurements of spectral density of the voltage at phase detector output in PLL loop, for Fourier frequencies well above loop cutoff frequency. Authors obtained such results for the right (100 MHz) and left (5 MHz) PLL loops of Fig. 1. The results of σ_x vs averaging time τ, obtained in approximate manner using known simple translation formulas and partially the formula (2), are given at Fig. 4 for the right PLL loop of Fig. 1. The results are from 0,16 ps to 2,5 ps for averaging times 4 μs and 100 ms, respectively, when assuming equal quality of both oscillators. To obtain $\sigma_x(\tau)$ values from the spectrum analysis for the case of left PLL loop we used formulas (3), (4) and (5). Between the experimental points of U(f), linear change of U^2 vs Fourier frequency was assumed. These results are given in the Table 1, together with the results of § 3.

3. Measurements of the time scale jitter in the time domain

These measurements were done using special apparatus developed by dr Jarkowski. Block scheme of this instrument is given at Fig. 7. We used the comparison of frequencies of two synchronized in PLL oscillators of 5 MHz. 100 MHz frequency was divided to obtain 5 MHz. Using the frequency synthesis methods this instrument multiplies the instantaneous frequency difference between oscillators by two, and decreases the mean frequency 5 000 times. In that manner the Allan deviation σ_y and time scale deviation σ_x are multiplied by 10 000. Then, 2 ps time scale fluctuations at the inputs produce easily measureable 20 ns fluctuations of the period of 1 kHz output frequency. These fluctuations were measured using multiple period meter (gated counter) with 100 MHz clock. The period meter mentioned must use one of the oscillators compared as the external clock. Changing the number of periods measured one can change the averaging time τ. But PLL filter time constant sufficiently bigger than τ must be used.
The results for the first (left) PLL loop of Fig. 1 are given in Table 2, and for the second (right) loop - in Table 1. For both cases, two oscillators included in the first (5 MHz) PLL loop are OCXO 10 oscillators. Due to the use of another oscillators in the first loop, the results for 2-nd loop obtained here are not comparable with the spectrum analysis results of § 2. But these results are similar (compare

Table 2 and Fig. 4 results).

Such comparison is possible for the 1-st loop. In that case, both results of Table 2 are obtained for the same pair of OCXO 10 oscillators. The results of § 3 are smaller than respective values of § 2. That can be partially explained by the insufficient selectivity of selective nanovoltmeters used. The error from that reason was estimated as at least + 26% for the values obtained from spectrum analysis.

All results are obtained for two oscillators. Assuming their equal quality, $\sigma_x(\tau)$ from time domain measurements equals approx.: 1; 1,7; 2,1; and 4,2 ps for averaging times: : 1; 10; 100 ms and 1 s, respectively.

4. Experimental proof of the relation between σ_x and σ_y

Using the method described in § 3, we measure the differences of time moments in the time scale from nominal ones. Taking the standard deviation of the sample we obtain directly standard deviation of the time scale generated.

Using the same samples of time scale deviations there exists the possibility to check in our case the relation $\sigma_x = \tau \sigma_y$, as explained below.

When measuring the period using counter, averaged period for averaging time $\tau = k\, T_o$, (k being the integer number of periods measured) is measured.

The differences of frequency and period are connected in that manner:

$$\frac{\Delta T_o}{T_o} \simeq - \frac{\Delta \nu}{\nu_o}$$

For the mean values,

$$\frac{\overline{\Delta T_o}}{T_o} = \frac{k\,\overline{\Delta T_o}}{k\, T_o} = \frac{(\Delta\tau)_i}{\tau} \simeq \frac{\overline{\Delta \nu_i(\tau)}}{\nu_o} = - \overline{y}_i(\tau)$$

$$(\Delta\tau)_i = -\tau \overline{y}_i(\tau) \qquad (6)$$

The samples of mean fractional frequency offset for the averaging time τ, $y(\tau)$, can be obtained from the time scale differences $\Delta\tau$, as indicated above.

From [3], p. 22, Allan variance

$\sigma_y^2(2,T,\tau) = \frac{1}{2}\,\overline{(\overline{y_{i+1}}(\tau) - \overline{y}_i(\tau))^2}$. Using (6), we obtain: $\tau^2 \sigma_y^2(\tau) = \frac{\tau^2}{2}\,\overline{(\overline{y_{i+1}}(\tau) - \overline{y}_i(\tau))^2} = \frac{1}{2}\overline{\left[(\Delta\tau)_{i+1} - (\Delta\tau)_i\right]^2}$

Then, comparing the standard deviation of $\Delta\tau$ with the square root of half of the mean value of squares of the differences of successive $\Delta\tau$ - s, one can check the relation between $\sigma_x(\tau)$ and $\tau\sigma_y(\tau)$.

Small part of the results for the relation between σ_x and $\tau\sigma_y$ obtained by authors for the samples of 50 measurements one can see in Tables 3 and 4. Excluding one sample in Table 3, all results are within 0,9 ÷ 1,1.
In [4], [5] and [6] one can find the opinions, that σ_x should be equal $\tau \cdot \sigma_y$. Our experimental results indicate, for our case, that σ_x equals within the ±10% error, $\tau \cdot \sigma_y$ (2,T,τ), where T is of the order of 3 seconds.

5. Conclusions and plans

100 MHz time scale source of few picoseconds jitter was constructed and partially measured. The improvement of results reported up to ten times is expected after using less noisy components in PLL loops.
Some experimental confirmation of the relation $\sigma_x = \tau \cdot \sigma_y$ was obtained.
We plan to measure the jitter also using tightly coupled PLL loop method in time domain, as described by Allan [7] or Kartaschoff ([3], p. 176).

References

1 R.A. Baugh, L.S.Cutler, Microwave Journal, June 70, p.55.
2 J.Rutman. Proc. IEEE vol. 66 No 9, Sept. 78, p. 1059.
3 P.Kartaschoff. Frequency and Time. Academic Press, 1978, p. 27.
4 J.Barnes et all. IEEE Trans. on IM, vol. IM-20 No 2, May 71.
5 P.Kartaschoff. IEEE Trans, on IM, vol. IM-28 No 3, Sept. 79.
6 J.Kalisz. IEEE Trans. on IM, vol. 37 No. 2, June 88.
7 D.W.Allan. National Bureau of Standards Technical Note 669, May 75.

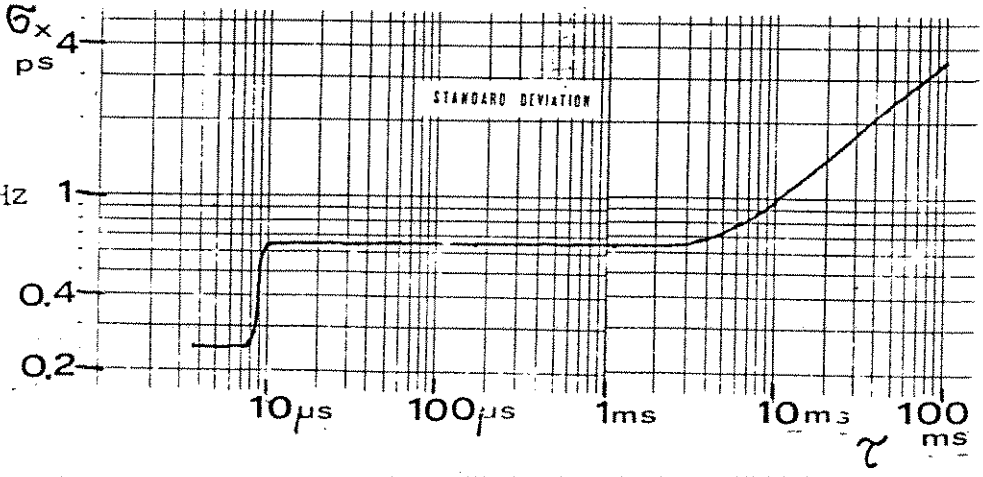

Fig. 4. σ_x values for the pair of 5 MHz and 100MHz oscillators.

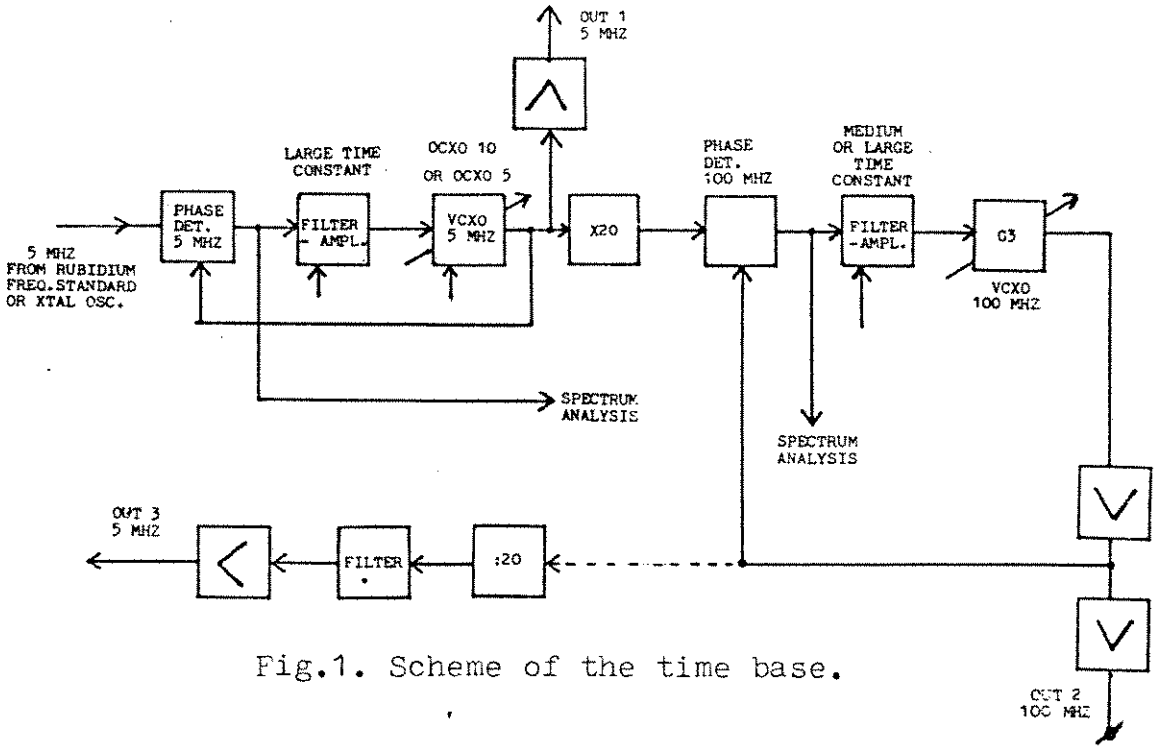

Fig.1. Scheme of the time base.

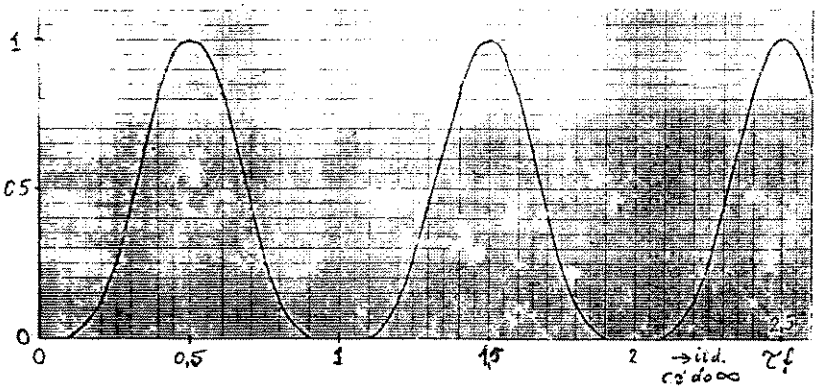

Fig.3. $\sin^4(\pi\tau_f)$ values vs τ_f

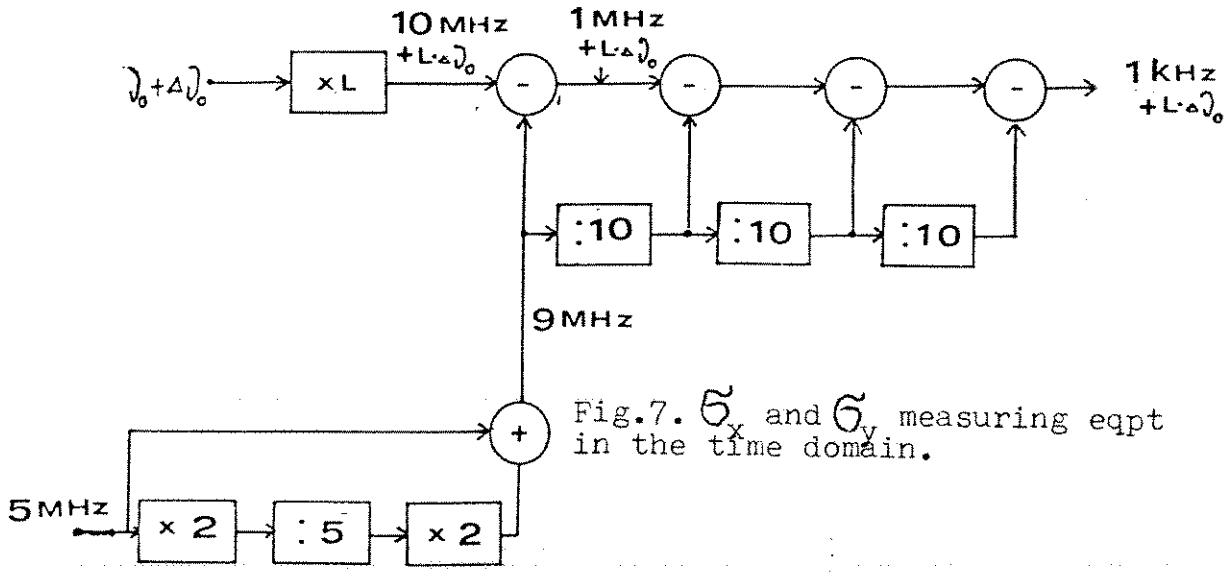

Fig.7. σ_x and σ_y measuring eqpt in the time domain.

$\tau \cdot \sigma_y(\tau)$ vs τ, 2 x OCXO10 5 MHz

TABLE 1

τ	Results from 50 meas. in sample, ps.						Averaged	Values from phase spectrum		
								Weighting accord. (5) 250 kc end	Weight. acc. (4) 250 kc end	Weight. acc. (4) 500 kc end
1 ms	1,013	1,485	1,439	0,937	2,266	1,161	1,525	3,760	4,598	5,037
10 ms	5,227	1,846	2,312	2,102	2,775	3,007	2,446	3,803	4,646	5,081
100 ms	1,396	1,672	3,120	4,677	2,701	1,852	2,951	3,847	4,690	5,120
1 s	4,803	6,492	7,420	4,221	4,974	--	5,911	3,988	4,871	5,286

$\tau \cdot \sigma_y(\tau)$ vs τ, 5 MHz 100 MHz OCXO10 + G3

TABLE 2

τ	Results from 50 meas. in sample				Averaged
1 ms	1,442	1,528	2,808	1,321	1,874
10 ms	4,466	3,762	6,179	3,769	4,252
100 ms	3,240	4,307	8,121	3,634	5,201

(ps)

$\frac{\sigma_x(\tau)}{\tau \cdot \sigma_y(\tau)}$ vs τ, 2 x OCXO 10 5 MHz

TABLE 4

	Results from 50 measurements in sample					
1 ms	1,010	0,916	0,924	1,024	0,927	1,039
10 ms	0,821	0,965	1,056	1,130	1,105	0,839
100 ms	1,047	0,985	0,948	0,907	1,039	0,935
1 s	0,992	0,926	0,988	1,005	1,072	—

$\frac{\sigma_x(\tau)}{\tau \cdot \sigma_y(\tau)}$ vs τ, OCXO10 5 Mc + G3 100 Mc

TABLE 3

τ	Results for samples of 50 meas.			
1 ms	0,9998	0,976	1,021	0,981
10 ms	1,151	1,530	1,096	1,194
100 ms	0,951	0,954	1,031	0,903

AVANCED TIME-INTERVAL DIGITIZER WITH PC CONTROL AND AUTOMATIC CALIBRATION

J. Kalisz, R. Pełka

Warsaw Academy of Technology
ul. Kaliskiego, 01-489 Warsaw Poland

Telephone : (Warsaw) 369016, 369602
Telex : 812535 WAT PL

J. Latka

Space Research Centre
Polish Academy of Sciences
ul. Ordona 21, 01-237 Warsaw Poland

Telephone : (Warsaw) 360119
Telex : 815670 CBK PL

ABSTRACT

The report first describes the current status of the Laser Ranging Station at the Borowiec Observatory of the Polish Academy of Sciences. After a general discussion of the modern time-interval digitizers for laser ranging applications the hardware and software details of the new time-interval digitizer T-1810B are described. The PC-based instrument features the automatic calibration, dynamic programmable range/window gate, and comprehensive software provinding pull-down menus, HGC/EGA/VGA autodetection, windows, and statistics/graphics processing.

(This is the condensed version of the original text. Full text is available on request).

1. Introduction

The report describes the new time-interval digitizer (TID) being developed for the Laser Ranging Station at the Borowiec Observatory of the Polish Academy of Sciences. The instrument is fully controlled by the IBM PC computer which is also utilized as the main input/output device.

To obtain picosecond accuracy and stability our unique statistical calibration method has been used (first published in 1985). It is based on a stochastic approximation search for precise determination of the current values of each interpolator's paramaters. The improved version includes an adaptive algorithm which tests the dynamic status of the instrument and sets its calibration rate withhout any intervention of the user. The other improvement is the compensation of the linearity error contributed by the analog time interpolators. The computer programmable range and windox gate makes possible the dynamic selection of optimally chosen measurement windows to reject unwanted noise signals. The systematic error is train of Poissonian pulses is applied internally to both inputs of the digitizer.

2. Current status and future plans of the Laser Ranging Station at the Borowiec Observatory

The second generation laser station at the Borowiec observatory has been developed during last decade.

Basic system operation is the automatic motion controlled by minicomputer but a manual operation mode is also provided. The computer program provides control for all involved actions like setting the instrument in starting position with anticipated correction, laser firing, closure of appropriate neutral filtres, and recording of time readings.

In the receiving system the Cassegrain telescope has been used with the spherical mirror of 635 mm active diameter and the focal length F of 5000 mm. A Galileus telescope has been adopted as the transmitting sytem corrected for the wavelength of 532 nm with the beam expansion factor of 8.6. This resulted in the initial beam divergence of 0.2 mrad. Main optical parameters are listed in the following table :

Receiving system - CASSEGRAIN	
Diameter of the mirror	636 mm
Diameter of the auxiliary mirror	198 mm
Transmitting system - GALILEUS	
Diameter of the objective	175 mm
Input diameter	20 mm
Beam expansion factor	8.65

The laser transmitter is placed near the central pillar in the lower part of the pavilion. A granite plate forms the transmitter base securing the mechanical stability of the

system. Main parameters of the transmitter are presented below.

Energy of pulses	150-200 mJ
Pulse length	4-5 ns
Wave-length	1060/530 nm
Beam divergency	10^{-3} rad
Repetition rate	1 Hz

3. Description of the digitizer T-1810B

To obtain high flexibility and fast operation at low cost we decided to design the TID in the form of a "black box" (i.e. the rack mounted case without dedicated display and keyboard) connected to the typical IMB PC XT/AT clone via a dedicated interface. Functionally the digitizer realizes the Nutt principle (START-STOP) without epoch timing) with dynamic programmable range gate and window to facilitate the rejection of unwanted noise signals. The epoch timing and the multi-stop real-time calibration were taken into consideration in the early stage of design but finally have been abondoned. The main reason for that was cost and time of dedelopment, which appearred greater in case of incorporating those features. From the user point of view the so-called real-time calibration also has been not necessary, since the potential gain in stability of about 5 mm/9 was is possible to make a true real-time calibration by timing the return from a small mirror placed at the elevation axis of the telescope/10 in, say, 10% of all measurements. It should be noted that the true system calibration of that or some other form is always necessary, since the classical real-time calibration, involving the use of some fibre optics led to the PMT, is able to discover only the relative changes of the system offset during the satellite passage but not the absolute values ot that offset.

The realization of high-resolution, dual-slope TDC's featuring the stretch factor of 10^4 is complex and expensive. To diminish the complexity of the converters and enhance their operational capabilities (better stability and reliability, shorter conversion time, lower cost) we have designed the TAC-ADC version of the TDC module, where two separate time-to-amplitude converters and two integrated, low-cost 12-bit A/d converters have been incorporated. The maximal conversion time is also lowered from about 300 μs to 35 μs. The best digital resolution is 11 ns/$2^{12} \approx$ 2.7 ps or in pratice 3 ps per channel.

As an external communication interface the dedicated I/O interface to the PC bus has been designed. Using the IBM PC bus extension the only limitation of that speed is the frequency of computer clock (for the PC XT Turbo with 8MHz clock the I/O transmission rate is equal to about 2 Mbytes/s, while the RS-232 and IEC-625 interfaces have the throughput of only 1200 bytes/s and 500 Kbytes/s, respectively).

4. Calibration

The calibration of the TID is accomplished internally to obtain (1) current values of the time offset and conversion gain of both TDC's involved, and (2) the time delay offset between the START and STOP inputs.

In 1985 we presented/[6] a unique method for precise autocalibration of picosecond TIDs using embedded microcomputer control. Applying this method to the design of the time interval digitizer T-1600 with 1 ps resolution and utilizing time stretchers with the stretch factor of 10^4 we obtained the standard deviation s_k of that factor equal to

0.85, or the calibration uncertainty below 1ps. We have used the same method in the currently developed time interval digitizer tT-1810B based on the TAC-ADC interpolation principale.

We also had to solve the problem of the calibration repetition rate strategy since this influences the measurement error caused by the time drift of TDC's characteristics between successive calibrations and determines the effective duration of the ready-state of the instrument. It has been accomplished by steady evaluation of drift of each TDC's conversion factor K and selection of the calibration rate so as to keep the changes δk between the subsequently identified values of K below a fixed value δ kmax. It means that the measurement uncertainty contribution resulted from driff of the TDC's conversion factors is kept below an assumed worst-case value. Thanks to the adaptive process a high calibration rate is needed only after power-on, or in the presence of very nonstable thermal conditions. Since the optimal calibration rate is being set by the control computer, the user is no longer forced to guess and find some (probably poor) solutions by manual setting.

To take full benefit of that higt precision calibration procedure also the remaining error sources, i.e. both the systematic error (time interval offset) and the linearity error should be compensated. For this purpose we have used an asynchronous pulser, which generates the burst of Poissonian pulses fed to the START and STOP inputs simultaneously. In that way a number of measurements of the true zero time interval can be performed and then the statistical estimate of the mean systematic error of the instrument can be calculated and saved to correct the following range measurements.

5. Software

The present implementation of the software provides following functions :
- failure detection,
- communication checking,
- self-test of operating papameters (long- and short-term error estimation),
- operating mode control,
- automatic calibration,
- acquisition of measurement data,
- calculation of measurement results,
- linearity error correction,
- statistical processing,
- graphics presentation of measurement results,
- file management.

The software has been written in the Turbo Pascal 4.0 programming language. Only few time-critical procedures for hardware control during the calibration and measure. The current version supports the HGC/EGA/VGA adapters and the IBM PC XT/AT I/O channel configuration . We presently utilize the Super VGA card and the NEC Multisync II monitor to achieve clear multiwindow displays and sharp graphics.
According to the general trend observed in development of the PC software we have employed the menu-driven user interface, which is easy to use without any user's experience in computer programming (Fig. 1).

Calibration procedure/[6] may be performed in three ways, as synchronous, asynchronous or involving both modes. At least one complete synchronous/asynchronous calibration is required before the measurement session.

The repartition rate of the calibration process is determined by the switchable parameter "Calibration trigger". In the "on" state, one out of four automatic trigger modes may be selected :
-immediately after each event,

-after each n-th event,
-after each n seconds,
-adaptive mode.

The first mode offers the best measurement accuracy but the dead time of the instrument may then be extensively long. The shortest dead time, while keeping a low measurement uncertainty, can be achieved with the use of the adaptive calibration mode.

The "Measurement modes" window in the main menu has been designed as an all-purpose control panel for setting the measurement, display, and data acquisition modes. We can choose between four main measurement modes : Start- Stop mode with a dedicated Start input or without such a distinction, and two measurement modes using the Common input for measurements of pulse width or time interval between two successive pulses on this input. Each of these modes can be used with an external synchronization.

Using the measurement control panel we can also define current values of the range gate and window. In addition, three display modes of results are available : Time Interval, Cable, and Range. Some user-defined calculation routines may also be incorporated, e.g. for tropospheric correction. The measurement results can be expressed in selectable length or time units.

There are four statistical functions available for processing the measurement samples : the mean, minimal and maximal value as well as the standard deviation. The automatic calculation of the efficiency (i.e; the radio of the total start pulse number to be received stop pulse number) is also provided.

The described software was tested during many laboratory experiments using the T-1800 TID as well as the currently developed T-1810 model. Figure 2 shows an example of the measurement histogram obtained when the delay of few metres of the coaxial cable RG-58C/U was measured.

6. References

1. Degnan J.J. "Satellite Laser Ranging : Current Status and Future Prospects", IEEE Trans. on Geoscience and Remote Sensing, Vol. GE-23, N^o 4, July 1985, pp. 398-413

2. Greene B.A. "Epoch timing for laser ranging", Proc. 5th International Workshop on Laser Ranging Instrumentation (Herstmoncex Castle 1984), pp. 247-250

3. Steggerda C.A. "The development of a dual frequency event timer", Proc. Sixth International Workshop on Laser Ranging Instrumentation (Antibes - Juan les Pins 1986), pp. 225-243

4. Turko B. "A picosecond resolution time digitizer for laser ranging", IEEE Trans. Nucl. Sci., V . NS-25, N°1, February 1978, pp. 75-80

5. Turko B. "Space borne event timer", IEEE Trans. Nucl. Sci., V. NS-27, N° 1, February 1980, pp. 399-404

6. Kalisz J. , Pawłowski M. , Pełka R. "A method for auto-calibration of the interpolation time-interval digitizer with picosecond resolution", J. Phys. E. : Sci. Instrum.,

V. 18, 1985, pp. 444-452

7. Kalisz J. , Pawłowski M. , Pełka R. "A multiple interpolation method for fast and precise time dizitizing", IEEE Trans. Instrum. Meas. , V. IM-35, N^{o}2, June 1986, pp. 163-169

8. Kalisz J. , Pawłowski M. , Pełka R. "Error analysis and design of the Nutt time-interval digitizer with picosecond resolution", J. Phys. E. : Sci. Instrum., V. 20, 1987, pp. 1330-1341

9. Greene B.A. "Calibration of sub-millimetre precision satellite laser ranging systems", Proc. Sixth International Workshop on Laser Ranging Instrumentation (Antibes - Juan les Pins 1986)

10. Rayner J.D., Bowman S.R., Alley C.O. "Zero-range real-time calibration", ibid., pp. 373-376.

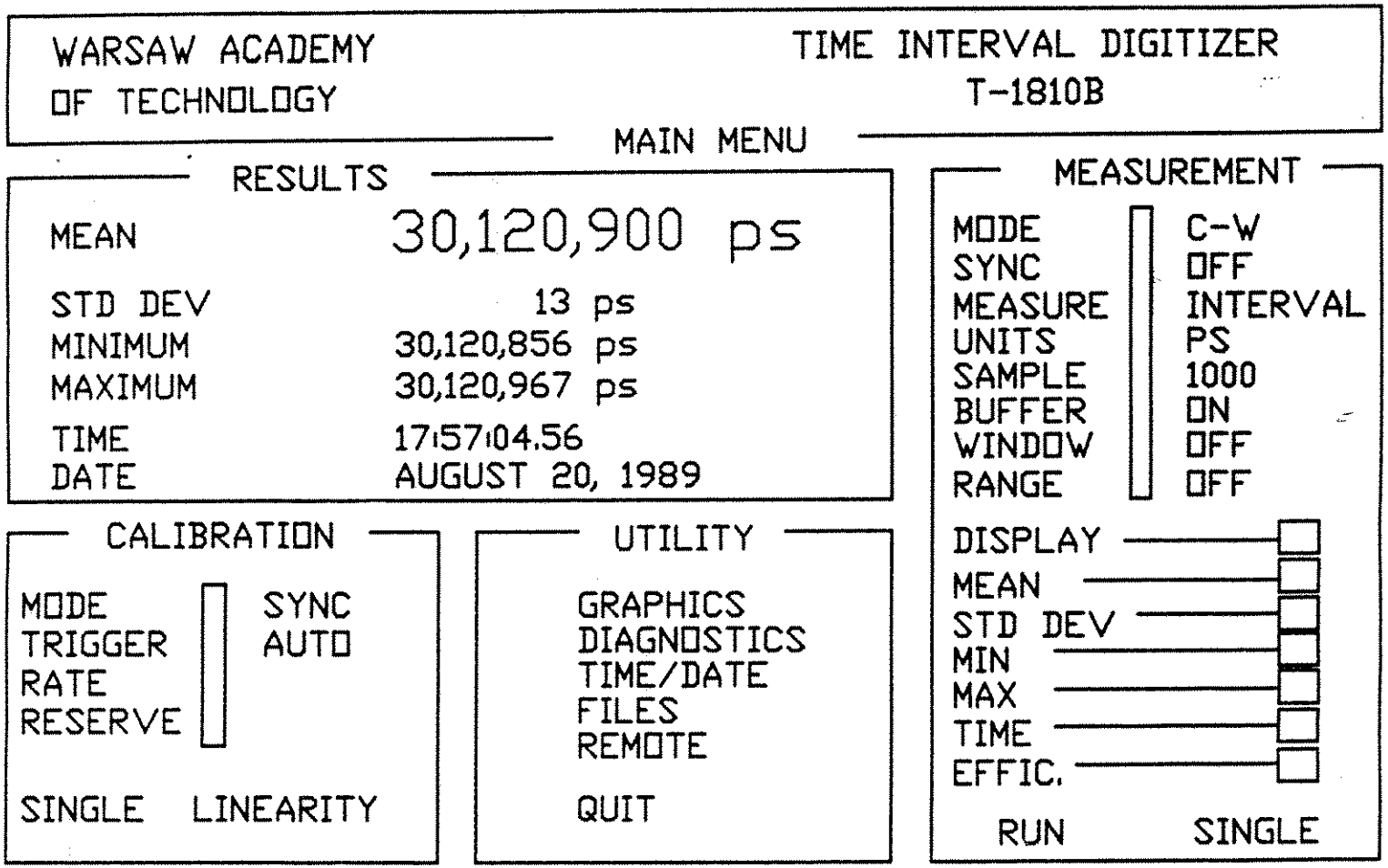

FIG.1 MAIN MENU OF THE T-1810B CONTROL PROGRAM

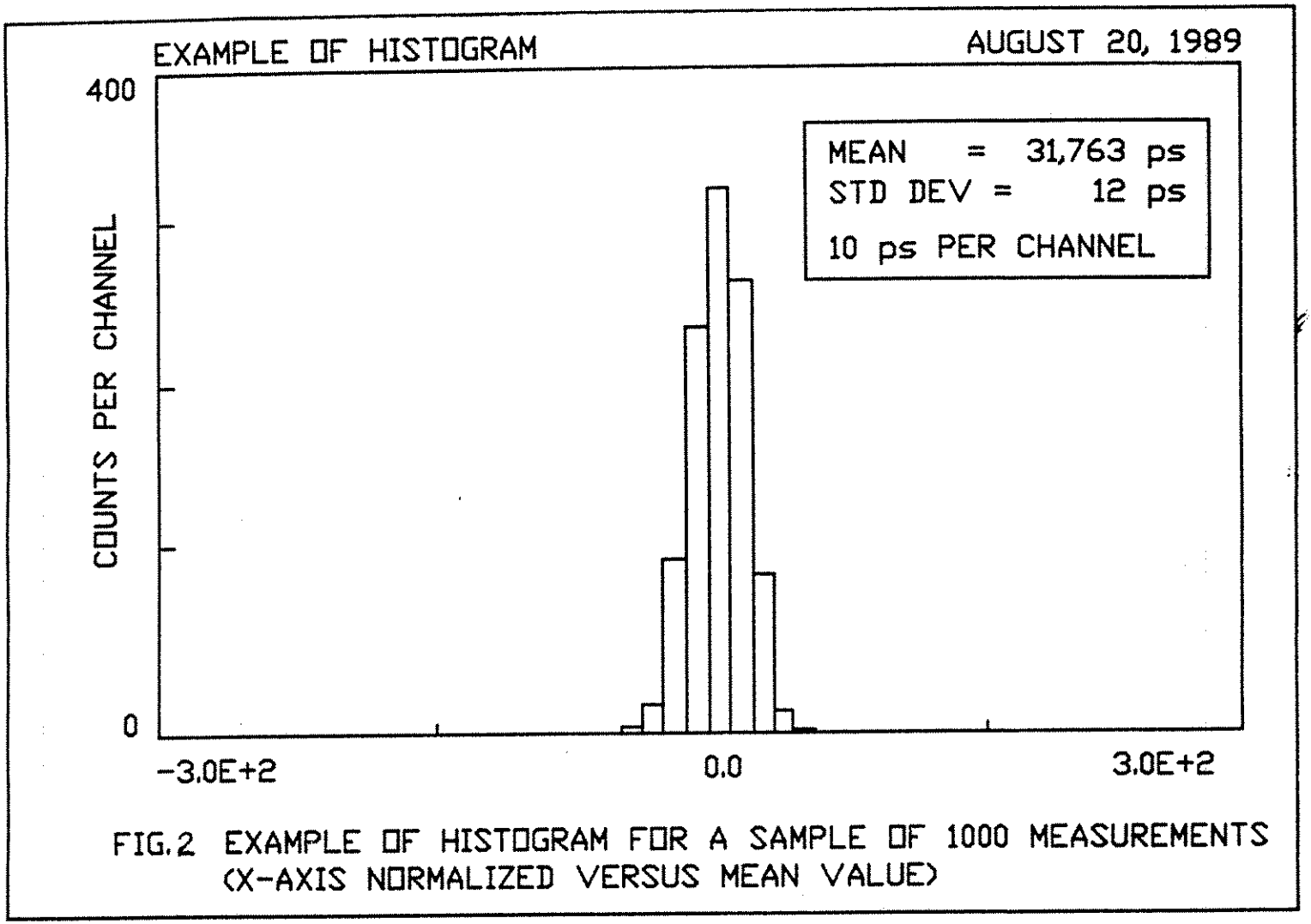

FIG.2 EXAMPLE OF HISTOGRAM FOR A SAMPLE OF 1000 MEASUREMENTS (X-AXIS NORMALIZED VERSUS MEAN VALUE)

SOME RESULTS FOR FEW- AND MULTI-PHOTOELECTRON RECEIVED SIGNAL PROCESSING

W.A. Kiełek
Department of Electronics
Warsaw University of Technology
Warsaw, Poland, 00-665

Telephone 48 22 253929
Telex 813 307 PW PL

ABSTRACT. Some author's results are given for the influence of signal processing on the accuracy of satellite laser radar for such processing methods as constant and proportional threshold of current and charge crossing discrimination, ORTEC & TENNELEC constant fraction and short circuited delay line shaping and zero crossing discrimination. Theoretical and simulations results are given for the dependence of error on the processing methods and parameters and photoelectrons number in the received signal.

1. INTRODUCTION. In the case of pulse laser satellite rangefinder, the received signal at the photomultiplier PMT (or other photodetector) output can be modeled as the unhomogeneous filtered stochastic Poisson point process. Single realisation of that process is of the form

$$f(t) = \sum_{i=1}^{K} g_i \, f_{SER}(t - \underline{t}_i - \underline{\tau}_i) \tag{1}$$

where: K - Poissonian number of photoelectrons (PE) realised, g_i, $\underline{t}_i$, $\underline{\tau}_i$ - random variables: PMT gain, moments of time of PE generation at the photocathode, and delay in PMT, respectively; $f_{SER}(t)$ - deterministic shape of single PE (photoelectron) response of PMT.
For the processes of that type the formulas for expectation, covariance and variance were given in [1], [5] and [7].

$$E\left[\underline{f}(t)\right] = \int_m^n s(v) E\left[\underline{f}_{SER}(t - v)\right] dv \tag{2}$$

$$Cov\left[\underline{f}(t_1), \underline{f}(t_j)\right] = \int_m^r s(v) E\left[\underline{f}_{SER}(t_1 - v)\underline{f}_{SER}(t_j - v)\right] dv \tag{3}$$

$$Var\ \underline{f}(t) = \int_m^n s(v) E\left[\underline{f}^2_{SER}(t - v)\right] dv \tag{4}$$

where: $E[...]$ - expectation of $[...]$, $\underline{f}_{SER}(t) = \underline{g}\, f_{SER}(t)$ where $\underline{g}$ - stochastic PMT gain, and, in case of absence of additive noise and satellite retroreflector coherent interference, s(t) it is the convolution of the laser pulse shape and photomultiplier delay probability

density (pdf) curve. Integration limits are chosen in the manner to contain all non-zero values of respective products.
In the case of such delay estimation methods as fixed threshold or threshold proportional to maximum value of photomultiplier current or charge, or Gedcke - Mc Donald "constant fraction" discriminator, or short - circuited delay line shaping and zero-crossing discriminator [3], the variance of the value of the process at the decision point, it is the (finite or infinite) linear combination of variances and covariances following (3) and (4). Then, that variance is proportional to N, mean photoelectron number in the signal s(t) (due to existence of s(v) in (3) and (4)). The variance is also proportional to α, mean square of normalised to unity photodetector gain, due to existence of $E\left[f_{SER}^2\right]$ or $E\left[f_{SER}(a) \cdot f_{SER}(b)\right]$ in (3) and (4).
The decision in the discrimination process is undertaked in dependence on the value of some stochastic process D, which is, for all above - mentioned methods, of the type of linear combination of the values of the process of the type (1), eventually shifted in time by strictly definite values. Taking, instead the amplitude of the process (1), its expectation, one can compute the derivative of the expectation of the process D, named D_1. Computer simulations show, that for sufficiently high N, it is possible to linearize the transition from the variance of the amplitude of the process D, to the decision time variance, using the square of the derivative D_1 in the vicinity of decision time point. That derivative is proportional to N and indepedendent on α, and we obtain for the normalised standard deviation of the error, for all practical shapes of pulses of interest (s(t) and $f_{SER}(t)$),

$$\sigma_\Delta / T = g_1 \alpha^{1/2} N^{-1/2} \qquad (5)$$

where T it is the half of width of the "equivalent" laser pulse (convolution of laser pulse and PMT delay probability density function). The g_1 coefficient is dependent on processing method, shape of the signal, and parameters of processing such as fraction, linear filtration (relation of f_{SER} width to the width of equivalent laser pulse), and delay. Simulations show, that g_1 is almost independent on N, when integration takes place, as in half area, and center of gravity methods, or sufficient filtration exists. For other cases there is some dependence on N in the small N region, especially for small or no filtration. The validity of (5) is preserved when the relation $t_R \gg t_N$ holds, where t_R - smallest rise or fall time of the laser pulse, t_N - mean time distance between photoelectrons within laser pulse.
Author published the curves and formulas for g_1 vs parameters for gaussian laser pulse and constant fraction of current and charge, fixed threshold of current, and center of gravity in [4]. Simulation results for g_1 and mean value of results change vs photoelectron number are given in [2], [3], and [4]. Further results are given here.

2. CONSTANT FRACTION OF CURRENT (VOLTAGE AT 50Ω). For the filtered case, any shape of the pulses of interest, and constant fraction of PMT current (voltage at 50Ω) crossing methods, using approximation described above, author obtained the formula for random error as follows:

$$\sigma_\Delta^2 = \frac{\alpha}{N}\Big\{ s_1(t_f) * f_{SER}^2(t_f) + f^2\, s_1(t_s) * f_{SER}^2(t_s) +$$

$$- 2f \int_{-\infty}^{\infty} s_1(\tau)\, f_{SER}\,(t_f - \tau)\, f_{SER}\,(t_s - \tau)\, d\tau \Big\} \cdot$$

$$\cdot \left\{ \frac{d}{dt} \left[s_1\,(t_f) * f_{SER}\,(t_f) \right] \right\}^{-2} \qquad (8)$$

where s_1 - shape of the equivalent laser pulse (convolution of the laser pulse and PMT delay p.d.f.), normalised as follows:

$$\int_{-\infty}^{\infty} s_1\,(t)\, dt = 1. \qquad \text{Also} \int_{-\infty}^{\infty} f_{SER}\,(t)\, dt = 1.$$

t_f - moment of time of reaching the fraction of its top value of the convolution of equivalent laser pulse and f_{SER}
f - fraction value
t_s - moment of time of reaching the top value of the convolution of equivalent laser pulse and f_{SER}
$*$ - convolution operator

The formula (8) is more complicated than Hyman formula (9) given below, because in the case of interest there are two processes of type (1), signal and threshold, and they are partially dependent (dependency is higher when higher is the filtration value, f_{SER} width). In that case there is the need additionally to use (3) to obtain the variance of amplitude of the process D, which in that case is the difference of the signal and the adaptive threshold at the crossing point.

3. CONSTANT THRESHOLD OF PMT CURRENT CROSSING DISCRIMINATION. The formula and curves for g_1 of (5) for Gaussian laser and f_{SER} pulses versus parameters was given in [4] and will be not repeated here. For the other than gaussian pulses of interest shapes, there exists the Hyman formula [14]

$$\sigma_\Delta^2 = \frac{\alpha}{N} \cdot \frac{s_1\,(t_p) * f_{SER}^2\,(t_p)}{\left\{ \frac{d}{dt} \left[s_1\,(t_p) * f_{SER}\,(t_p) \right] \right\}^2} \qquad (9)$$

where s_1 as above,
t_p - moment of time when the convolution of equivalent laser pulse and f_{SER} crosses the threshold.

Author obtained many curves using (8) and (9) vs parameters for light pulse shapes characteristic for scintillation counters, using clipped Gaussian delay pdf and f_{SER}. The amount of results is too big to show them here. The results show, that smaller error can be obtained not always in the constant fraction method. It is dependent on parameters, such as the amount of clipping, and relations of widths of light, delay pdf, and f_{SER} pulses.

For the filtered case, and gaussian laser pulse, the mean value changes with signal energy can be obtained from the formulas given in Table 2 obtained by author for the cases of fixed threshold and constant fraction crossing method for current and charge. In some cases that results are limited to some energy region.

4. CONSTANT CHARGE THRESHOLD CROSSING DISCRIMINATION OF PMT OUTPUT. The formulas and curves for g_1 coefficient in (5) for that case, obtained by author when using (2) + (4) for the case of no filtration before integration of PMT current, are given in Table 1 and at Fig. 1 for 7 different shapes of "equivalent" laser pulse. These results are valid for no filtration case.
For the filtered case, and any pulses of interest shapes, there exists old (1957) Gatti - Hyman formula [13], [14]

$$\sigma_\Delta^2 = \frac{\alpha}{N} \cdot \frac{s_1(t_p) * \left(\int_{-\infty}^{t_p} f_{SER}(t)\,dt\right)^2}{\left\{s_1(t_p) * f_{SER}(t_p)\right\}^2} \qquad (14)$$

where s_1, t_p as above.

5. CONSTANT FRACTION OF TOP VALUE OF THE CHARGE CROSSING DISCRIMINATION OF PMT OUTPUT. This method can be implemented using integration of PMT output (for instance using appropriate transversal filter) and constant fraction discrimination. In the case of fraction value 0,5 this method is called half - area or median. Some results obtained by author for mean value of results change with energy for half - area discrimination (Gaussian laser pulse) are given in [2], [3], and [4]. The formulas and curves of g_1 coefficient in (5) versus parameters for the case of no filtration before integration are given in Table 1 and Fig. 1. Some results for filtered case are given in [4].

6. ORTEC, TENNELEC AND SIMILAR GEDCKE - Mc DONALD TYPE "CONSTANT FRACTION" DISCRIMINATORS. For the gaussian pulses of interest, author obtained and published in previous VI-th Workshop Proceedings [3], many results for that case. These results will be not repeated here. For the case of other than gaussian pulse of interest shapes, author obtained the formula for random error as follows:

$$\sigma_\Delta^2 = \frac{\alpha}{N}\Big\{s_1(t_c) * f_{SER}^2(t_c) + f^2\, s_1(t_c + T_d) * f_{SER}^2(t_c + T_d) + \\ - 2f\int_{-\infty}^{\infty} s_1(\tau)\, f_{SER}(t_c - \tau)\, f_{SER}(t_c + T_d - \tau)\, d\tau\Big\} \cdot \\ \cdot\left\{\frac{d}{dt}\left[s_1(t_c) * f_{SER}(t_c) - f\, s_1(t_c + T_d) * f_{SER}(t_c + T_d)\right]\right\}^{-2} \qquad (15)$$

where t_c - moment of time, for which, for the first time when increasing time t, one obtains

$$s_1(t_c) * f_{SER}(t_c) = f\, s_1(t_c + T_d) * f_{SER}(t_c + T_d)$$

f - "fraction" (Not the real fraction, but only the coefficient in the equation realised within that scheme

$$f \cdot \psi(t) = \psi(t - T_d)$$

T_d - delay time of delay line at Fig. 1 of [3], others as above.

$\Psi(t)$ - PMT output current.
(15) is more complicated than (8), because the delay T_d of delay line of the discriminator is free parameter here.

7. SHORT - CIRCUITED DELAY LINE SHAPING AND ZERO CROSSING DISCRIMINATOR (SCDL). According the author's knowledge, for laser ranging that method was used for long time at the Potsdam station only. Block scheme of that discriminator is given at Fig. 2. The random error for any pulses of interest can be obtained from author's formulas (15) of this report and (4) of 3 for the "fraction" f value equal 1, and T_d equals double delay time of the line at Fig. 2, when there ere no jumps described also in 3 . But jumps are possible for the laser signal of small contrast only. The formulas 8, 9, 14, 15 are obtained using the approximation described at the Page 2.

8. CONCLUSION. This report completes the series of author's reports about the error from stochastic discrete generation, delay and gain of photoelectrons in few - and multi - photoelectron case (see Proceedings of 4-th, 5-th and 6-th Laser Workshops). When gathered together, they give the totality with some completness. Most of ideas and results given here are original.

REFERENCES

1. E.Parzen. Stochastic processes. San Francisco, Holden-Day, 1962, p. 156
2. W.Kiełek et al. 4-th Laser Workshop Proc. (Austin), p. 418
3. W.Kiełek. 6-th Laser Workshop Proc. (Antibes), p. 189
4. W.Kiełek. 5-th Laser Workshop Proc. (Herstm.), p. 122
5. D.L.Snyder. Random point processes. N.Y., Wiley, 1975, p. 171, 172
6. H.David. Order statistics.N.Y., Wiley, 1970
7. A.B.Sharma. Reports of the Finnish Geodetic Institute, No 75; 10, 1975
8. I.Bar David, M.Levy. IEEE Trans. on IT, vol.24, No 1, Jan. 78
9. J.B.Abshire. NASA Technical Paper No 1315, Sept. 78
10. W.Kiełek. Influence of processing of the received signal on the accuracy of laser satellite rangefinders (in Polish). Wydawnictwa Politechniki Warszawskiej, Warszawa 1988
11. F.D.Ghigo et al. Applied Optics, v. 15, No 11, Nov. 76, p. 2631
12. I.Bar David. IEEE Trans. on IT, May 75, p. 326
13. S.Colombo, E.Gatti et al. Nuovo Cimento 5 (1957), p. 1739
14. L.G.Hyman et al. Rev. of Sc. Instr. v. 35 No 3, March 64, p. 393

Table 2. Mean value of the result change, Δ/σ_i, normalised to σ_i parameter of Gaussian signal pulse, vs filtration coefficient $F = \sqrt{8\ln 2}\,\sigma_F/\sigma_i$, fraction f, and energy in photoelectrons K. σ_F it is the parameter of Gaussian filter response.

		of the current or voltage (at 50Ω)	of the charge
Fixed threshold	for energy change from K1 to K2 when K_{pr} - sensitivity limit $(K1, K2 \geqslant \frac{20}{F^2}$; $K_{pr} \geqslant 10)$	$-\left[\left(\ln\frac{K2}{K_{pr}}\right)^{1/2} - \left(\ln\frac{K1}{K_{pr}}\right)^{1/2}\right] \cdot \left[2\left(1 + \frac{F^2}{8\ln 2}\right)\right]^{1/2}$	$\left(\text{inv erf}_{*}\frac{K_{pr}}{K2} - \text{inv erf}_{*}\frac{K_{pr}}{K1}\right) \cdot \left(1 + \frac{F^2}{8\ln 2}\right)^{1/2}$
	for energy change from 1 to K2 (f_1 - sensitivity limit as the part of the single photoelectron)	$-\left[\left(1 + \frac{F^2}{8\ln 2}\right)^{1/2} \cdot \left(2\ln\frac{K2}{f_1}\right)^{1/2} + -\left(\frac{F^2}{8\ln 2}\right)^{1/2} \cdot \left(2\ln\frac{1}{f_1}\right)^{1/2}\right]$	$\left(1 + \frac{F^2}{8\ln 2}\right)^{1/2} \cdot \text{inv erf}_{*}\frac{f_1}{K2} + -\left(\frac{F^2}{8\ln 2}\right)^{1/2} \cdot \text{inv erf}_{*} f_1$
Constant fraction of top value	for energy change K from 1 to ∞ f - fraction of top value	$-\left[\left(1 + \frac{F^2}{8\ln 2}\right)^{1/2} - \left(\frac{F^2}{8\ln 2}\right)^{1/2}\right] \cdot \left(2\ln\frac{1}{f}\right)^{1/2}$	$\left[\left(1 + \frac{F^2}{8\ln 2}\right)^{1/2} - \left(\frac{F^2}{8\ln 2}\right)^{1/2}\right] \cdot \text{inv erf}_{*} f$

K - number of photoelectrons in the received signal

Definition of the erf_{*} function one can find in Table 1.

Table 1. Coefficient g_1 of (5) for fixed threshold and constant fraction of charge methods. No filtration before integration of the PMT current. In the first case, f it is the threshold value divided by the expectation of max. value of the charge.

	i(t)	g_1 Constant fraction of charge	g_1 Constant threshold of charge
1		$2[f\,(1-f)]^{1/2}$	$2\,f^{1/2}$
2		$(2-2f)^{1/2}$ $f = 0 \div 0{,}5$ | $(2f)^{1/2}$ $f = 0{,}5 \div 1$	$\sqrt{2}$ $f = 0 \div 0{,}5$ | $\left(\frac{2f}{1-f}\right)^{1/2}$ $f = 0{,}5 \div 1$
3		$2f^{1/2}$	$2\left(\frac{f}{1-f}\right)^{1/2}$
4		$2\,(1-f)^{1/2}$	2
5	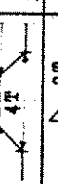	$\frac{2}{\ln 2}\left(\frac{f}{1-f}\right)^{1/2}$	$\frac{2}{\ln 2}\frac{f^{1/2}}{1-f}$
6	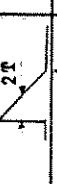	$\frac{[2\pi f(1-f)]^{1/2}}{M}$ $M = (2\ln 2)^{1/2} \cdot \exp\left[-(\text{inv erf}_{*} f)^2/2\right]$ $\text{erf}_{*}\,x = \frac{1}{\sqrt{2\pi}}\int_{-\infty}^{x}\exp(-y^2/2)\,dy$ inv - inverse function	$\frac{[2\pi f]^{1/2}}{M}$
7		$\frac{[f(1-f)]^{1/2}}{1(t_f(f))}$ $t_f + \frac{1}{2\pi}\sin\left(\frac{\pi}{2}t_f\right) + \frac{1}{2} = f$ $i(t) = \frac{1}{4}\left[1 + \cos\left(\frac{\pi}{2}t\right)\right]_{-2}^{2}$	$\frac{f^{1/2}}{1(t_f(f))}$

* $\frac{\ln 2}{2}\exp\left(-t\frac{\ln 2}{2}\right)$

* $\frac{1}{\sqrt{2\pi}\sigma}\exp\left(-\frac{t^2}{2\sigma^2}\right)$

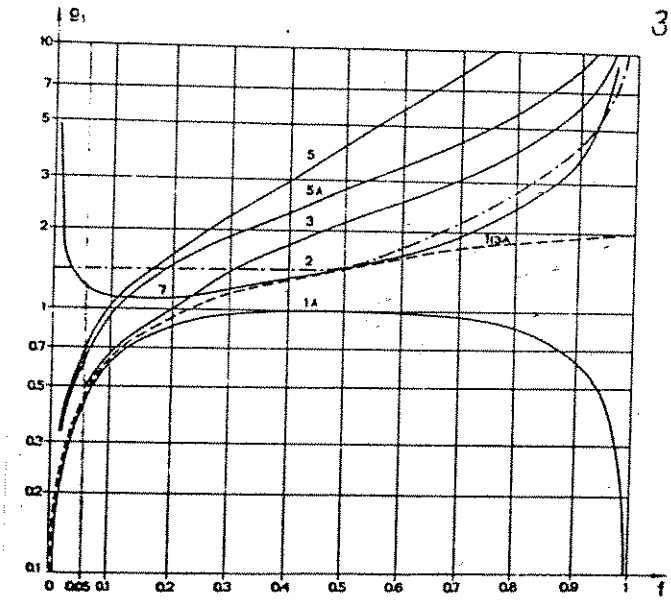

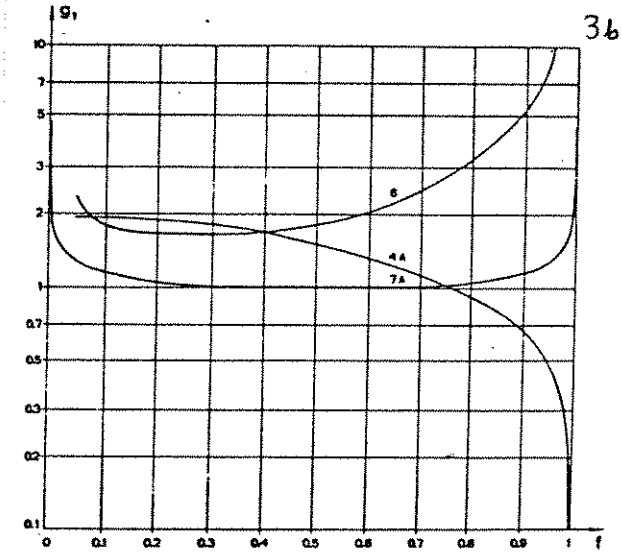

Fig.1. g_1 versus fraction and pulse shape following Table 1.A-marked curves are for the constant fraction case. Normalisation in (6): to the parameter σ for Gaussian pulse, and to the half-width of the pulse for rest.

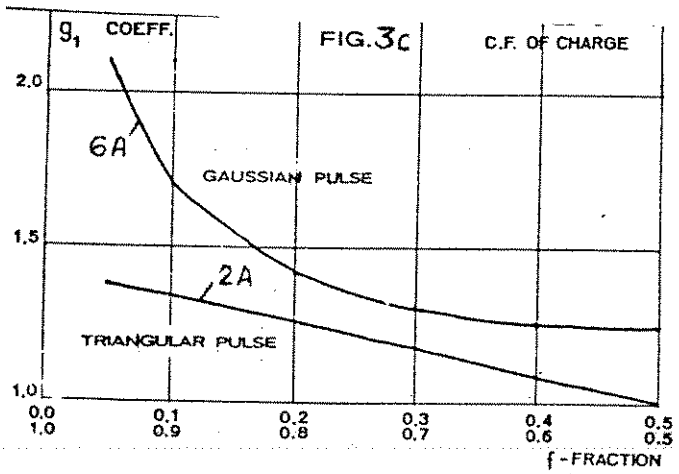

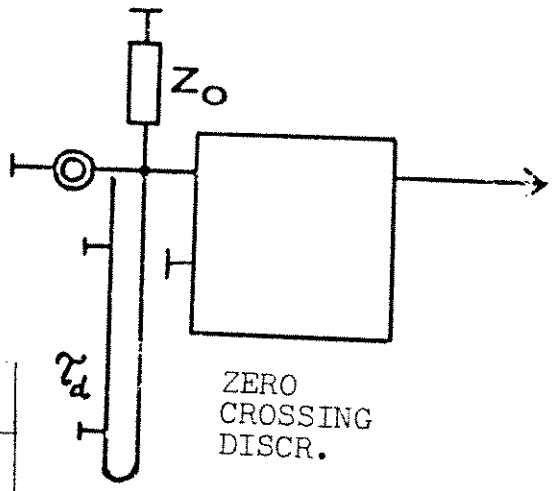

Fig.2. Scheme of the short - circuited delay line shaping and zero crossing discriminator.

Calibration

An Analysis of Range Calibration Values from the UK SLR System, 1985-1989

G.M.Appleby and W.E.Matthews
Royal Greenwich Observatory
Herstmonceux Castle
Hailsham
East Sussex BN27 1RP
England

Abstract. We give an account of observed variations in the range calibration values that are used to refer raw satellite ranges to the reference point of the UK SLR System at Herstmonceux. These variations are mostly attributable to system changes or to changes in the background-noise rates encountered during satellite and calibration ranging. We describe how most of the effects of these variations are accounted for in the reduction of the observations. The short-term stability of the calibration value is also demonstrated.

1. Introduction. The UK SLR system began regular operations during 1983 October. Since then it has become one of the most productive 3rd-generation systems in the world, regularly obtaining ranges from more than 50 passes of LAGEOS per month, with a current single-shot precision of 3.5cm RMS. In common with many similar systems in the network, raw satellite ranges are converted to distances refered to the system's invariant point by measuring the system delay, or calibration value, using local-target ranging. The precise distance of the local target from the system's invariant point, incremented by the calculated atmospheric delay along the light-path, is subtracted from the mean of the observed ranges to the target to yield a system calibration value. For the UK system, the principal calibration target is a 1m square reflective plain board, mounted on a disused telescope dome, at a distance of 596.342m from the telescope. In this paper we investigate variations in the observed system delay. We discuss the discovery and removal of a background-related variation in the delay. We identify system changes that have altered the delay, and investigate its short-term stability, noting that for any SLR system the behaviour of this calibration value has a direct impact upon systematic errors inherent in deduced satellite ranges.

2. The Calibration Values. A full description of the use and software-calibration of the 4-stop Maryland Event Timer in both local-target and satellite ranging modes has been given by Sinclair (1983). Observational policy is to obtain a set of about 300 range measurements to the local target before and after every satellite pass, using the same laser energy for all measurements. The mean value of these measurements is treated as the current best-estimate of the system calibration. To ensure that laser returns are at the single-photon level during calibration ranging, the receiver aperture-stop is set to its minimum diameter, maximum laser-beam divergence is selected and neutral-density filters are inserted into the transmit laser path to attenuate the beam. The effect on the calibration of these filters is about 3mm, which to date has not been taken into account in the subsequent reduction of the observations, which is described in Appleby and Sinclair (1985). From 1985 April, all system calibration values obtained from local-target ranging sessions have been stored in machine-readable form. These data are the raw materials for the present investigation.

3. Impact of System Changes on Calibration Values. During the period of time considered in this investigation, several modifications to the timer-detector sytems have been caried out. The principal modifications are given in the Table. Since any such changes potentially modify the electronic delay of the system, their effects should be apparent in our data set. Shown in Figure 1(a) are individual values of the system calibration from 1985 April 24 to 1988 July 2. Some scatter is evident in the values, but for the first 920 days of the period the values are seen to be fairly constant, with an average of about 16.42m.

The discontinuity at MJD 47102 , 1987 November 3, marked (c), is caused by the replacement of the RCA 8850 photomultiplier tube by a spare device of the same type, as noted in the Table. On MJD 47346, 1988 July 4, this RCA PMT was again replaced, by a Hamamatsu type 1949 PMT. The characteristics of this 12-stage tube show a reduced time response, of 1.3 ns compared to 2.5ns for the RCA tubes, and a reduction in transit time-spread. Following this change, further improvements were made to the detector sytem over a period of a few months, as detailed in the Table. The result of these improvements was a reduction in the single-shot scatter from 5.5 to 3.6cm RMS. However, these changes did affect the calibration values by up to 3 meters after each significant modification, and it is not practicable to plot their true values on a single graph. Instead we give in Figure 1(b) the values plotted as differences from a series of piecewise mean values. In Figures 1(a) and 1(b) labeled arrows refer to specific events listed in the Table. It is apparent that there are sytem changes that had no detectable effect on the calibration values, and conversely there are apparent changes in the data set which do not have a listed cause. It should be emphasised that the changes in the calibration values particularly evident in Figure 1(b) did not adversely affect the satellite range data obtained during that period, since the policy of obtaining pre- and post-pass calibration measurements was followed at all times.

4. Effect of Background Noise on Calibration Values. Late in 1984 it was discovered (Standen, private communication) that the system delay appeared to vary with the amount of background noise being detected by the photomultiplier; the delay was less by the equivalent of 1-2 cm in daylight compared to that at night. The cause of this change is not fully understood, but is probably related to the geometry of the PMT.

To quantify the situation, the software controlling the calibration ranging operation was modified to obtain the background rate by sampling noise pulses from the PMT which fall within a specified time-window. The results, obtained during normal operations (and hence all at the single-photon level) from the first 3 months of 1985, were averaged over intervals of 0.05MHz, and are shown in Figure 2. The standard errors of each of the mean values were also calculated, and are displayed as error bars in the figure. There is a clear decrease in the system calibration value with increasing background rate, amounting to over 2cm at a rate of 2MHz. A parabola fitted to the results has equation

$$F(r) = (16.424 - 0.014r - 0.0018r^2)\text{m},$$

where r is the background rate in MHz, and this applies for the RCA PMTs.

Following the installation in 1988 July of the Hamamatsu photomultiplier tube, a new calibration curve was required immediately; we could not wait for several months to accumulate data over a wide range of conditions during normal operations. Hence a series of experiments was carried out to determine the detector's characteristics under changing background noise conditions. A series of daytime local target ranging runs was carried out during a period of less than 1 hour. In order to vary the background noise rate, the field-of-view iris was altered in steps from its smallest diameter of 1′ (normally used for calibration ranging) to its maximum value of 4′. In this way a large range of noise rates from 0.2 to 4.2MHz was obtained. The system-delay values derived from this experiment are plotted in Figure 3 against the corresponding background rates and iris settings (on a linear scale from zero to 100). A parabola (labeled (a)) has been fitted to these results. This experiment also showed that the laser return rate from the target increased from approximately 15% with the smallest diameter iris, to nearly 80% with the iris fully open. Poisson statistics suggest that at a return rate of 15%, most of those returns will be at the single photon level, which is also the situation during most satellite passes. However, the higher rates obtaining for much of the experiment imply that many multiple-photon events are present, and it is important to determine their effect on the

deduced system delay. Thus the experiment was repeated at night when the changes to the iris diameter had no effect on the near-zero background rates. The deduced system delays are plotted as triangles also on Figure 3, where a clear linear relationship with iris setting (equivalent to signal strength) is apparent. The fitted straight line is labeled (b) in the figure. We now remove from the data of curve (a) the signal-strength dependent part of the observed function by evaluating the linear function (b) at each iris setting of the corrupted data. The result is curve (c) in the Figure, which has been fitted to each corrected data point formed as described. The fitted function is

$$F(r) = (11.402 - 0.016r + 0.0022r^2)\text{m}.$$

4.1 Removal of Background Effect from Satellite Ranges. Since background rates of up to 2MHz are common during daytime satellite ranging, it is imperative that ranges are corrected for the effect. During satellite ranging, the software counts all noise points falling within the range gate, and hence computes a pass-averaged background rate, P MHz. The correction to be applied to the calibration value will depend on the *difference* between this rate and the observed rate during the pre- and post-pass calibration measurements. If for a given calibration value the background rate is C MHz, then the correction is $F(P) - F(C)$. The appropriate correction is added to the pre- and post-pass calibration values, before the mean of the two calibration values is subtracted from each observed satellite range. All observations obtained by the system since 1985 January have been corrected in this way. Typical daytime corrections are of the order of 1 or 2cm. A refinement to the system which will shortly be introduced is the measurement of background rates over short intervals of time during passes, and the use of those data to correct calibration values, rather than using the pass-averaged rate as at present. Data prior to 1985 have not been corrected, and so daytime ranges will be long by 1-2 cm, and night-time ranges will be correct.

5. Variation in Corrected Calibration Values. To investigate further the long-term stability of the system calibration value, we took the data shown in Figure 1(a) and reduced each result to a background rate of zero, using the method described in section 4. The short-term excursions of the data points were excluded from subsequent analysis. The data obtained since 1988 July, shown in Figure 1(b), were treated similarly, but since so many system changes were carried out whilst these data were being accumulated, a useful data set could not be formed for long-term study. The corrected data from Figure 1(a) were averaged at intervals of 10 days, the overall mean value was removed, and the results were plotted against time as shown in Figure 4.

The plot suggests that the system calibration varies with a near-annual periodicity, with semi-amplitude about 2cm. Such a variation suggests a meteorological origin. For horizontal ranging, temperature is the most critical parameter in calculating the atmospheric delay to be removed from the measured target range: however, an error of 1°C in the measurement of temperature along the light path will lead to an error of only 1.2mm in the computed 2-way delay to our local target (Sinclair 1982). Air-temperature measurements are made using an aspirated psychrometer situated in the dome. It is unlikely that the temperature along the 600m light-path to the target will be different by more than 1 or 2 degrees from that in the immediate vicinity of the telescope. Futher, a plot of the calibration values averaged with respect to air temperature shows no correlated variations.

It is thought unlikely that the variation could be due to a real change in the telescope-target distance; the target is securely fixed to a fairly rigid building. Short-period wind-induced variations are possible, but could not explain a sustained increase or decrease in target distance.

The most likely explanation is a slow variation in the system's electronic delay caused by small changes of

conditions in the laser and electronics room, or by ageing of for example the chemical dye used in the laser. There is some suggestion in the averaged data that the abrupt changes correspond to the times at which the bi-annual laser maintenance work is carried out. Such a real change of system calibration will of course be correctly removed from satellite ranges. However, if the observed variations of calibration are indeed due to changes in target distance, calibration values in error by up to ± 2cm will have been removed from raw satellite ranges.

A further 2 targets have been available for the last 12 months, and the results of routine measurements to all 3 targets should resolve this uncertainty. There are not as yet enough data from the 2 new targets to give any reliable information on this long-term behaviour, but the comparisons that have been possible show agreement at the few mm level.

6. Short-Term Stability of Calibration Values. It is very important that the system calibration does not vary during a pass. Significant changes of the type discused in earlier sections are unlikely as no system parameters are altered during any given pass, but in the absence of in-pass calibration, a series of calibration measurements made over a time-span comparable to a Lageos pass can indicate the probable behaviour during a pass. A series of standard 3-minute ranging sessions was made continuously for 110 minutes beginning at 1200hrs on 1989 November 17. The data were processed as before, and reduced to zero background rate from the observed low average value of about 0.15MHz. The same experiment was carried out in dark conditions beginning at 1930hrs on the same day. Both series of deduced calibration values are shown in Figure 5 plotted against time in minutes from the start of each observing session. Circles represent the daytime results, and triangles the night-time ones. The results appear random, with no apparent trends. The mean of the daytime values is 11.045m, and that of the night-time is 11.046m. The RMS of a single calibration value about the mean is 0.3cm for each data set. This level of agreement is considered excellent, and demonstrates the stability of the system on timescales comparable to satellite passes.

7. Conclusion. We have seen that small changes to the system configuration produce significant changes in system delay. We are satisfied that our policy of obtaining pre- and post-pass calibration values minimises the possibility of such changes introducing systematic errors into satellite range measurements. We have demonstrated the existance of a 'background-rate' effect in the system delay, of magnitude up to 2cm under normal ranging conditions. This effect has largely been removed from all data produced by the system since the beginning of 1985. A planned system upgrade to incorporate a micro-channel-plate detector should remove in the near-future this potential source of systematic error. However, we find that to an accuracy of a few mm, the current system calibration value may be regarded as constant over intervals of time comparable to a Lageos pass, and probably for much longer.

8. References

Sinclair,A.T. 1982. The Effect of Atmospheric Refraction on Laser Ranging Data. N.A.O. Technical Note *59*,Royal Greenwich Observatory, UK.

Sinclair,A.T. 1983. Programming and Calibration of the Event Timer for the SLR System at Herstmonceux. SLR Technical Note *4*, Royal Greenwich Observatory, UK.

Appleby,G.M. and Sinclair,A.T. 1985. Data Processing and Preliminary Analysis Software for the UK SLR Facility. SLR Technical Note *5*, Royal Greenwich Observatory, UK.

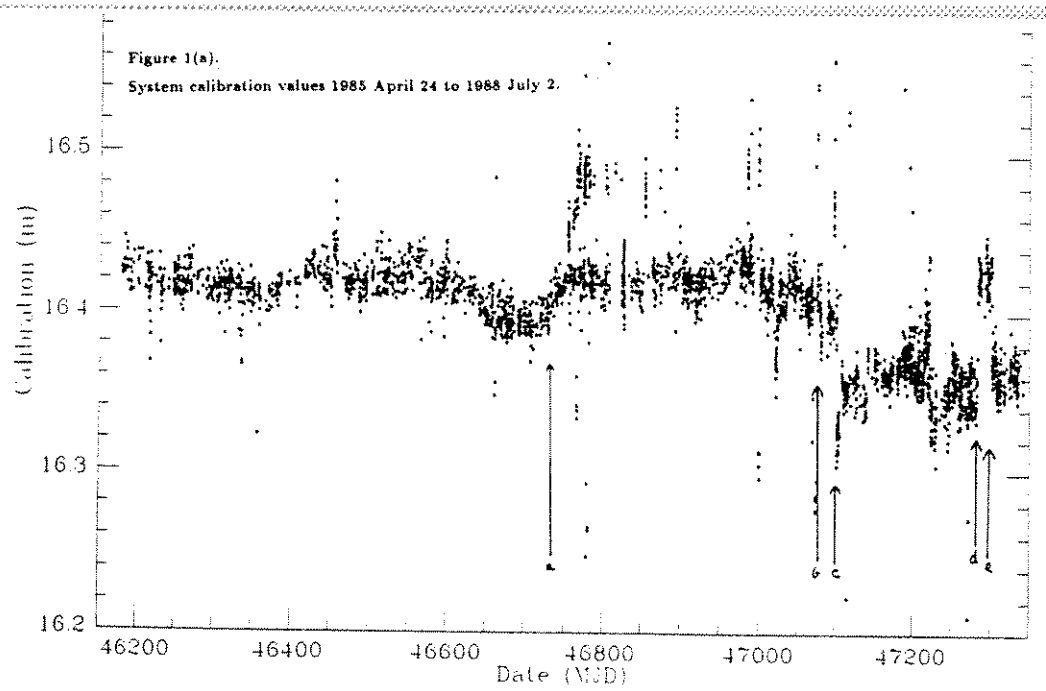

Figure 1(a).
System calibration values 1985 April 24 to 1988 July 2.

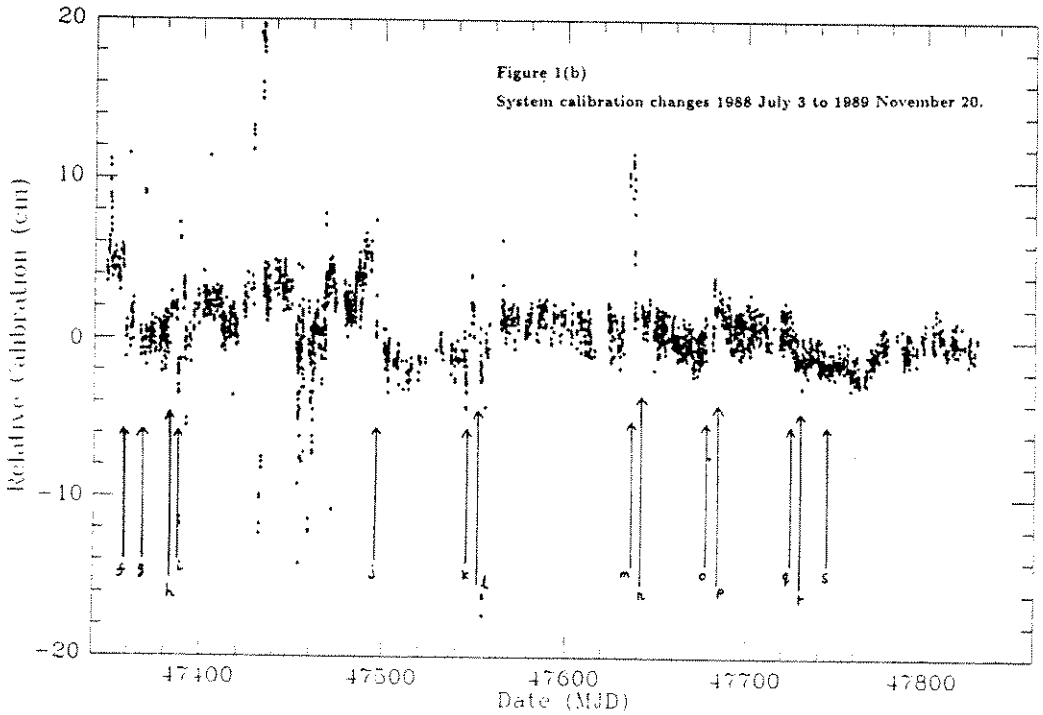

Figure 1(b)
System calibration changes 1988 July 3 to 1989 November 20.

Table of System Changes

Ref	Date	Modification	Calib. change (cm)
a	1986 Oct 30	Changes to start channel for local-target ranging	2
b	1986 Oct 13	Changes to PMT signal cable connections.	1
c	1987 Nov 3	Changed original RCA PMT for spare tube	5
d	1988 May 3	Replaced original RCA PMT	7
e	1988 May 21	Cable changes in discriminator modules	6
f	1988 Jul 14	Changed PMT to Hamamatsu type 1949	487
f	1988 Jul 15	Changed discriminator to Tennelec TC454	367
g	1988 Jul 21	Changed anode voltage on PMT	56
h	1988 Aug 10	Replaced L/E discriminator in start channel	314
i	1988 Aug 14	Changed anode voltage on PMT	9
j	1988 Nov 30	Repositioned start photodiode in laser	288
k	1989 Jan 21	Reset start diode discriminator threshold	2
l	1989 Jan 25	Reset start diode discriminator threshold	2
m	1989 Apr 18	Replaced faulty PMT supply. Changed anode volts	10
n	1989 Apr 21	Changed PMT signal cable; increase in length	251
o	1989 Jun 2	Replaced PMT supply. Reset anode volts	8
p	1989 Jun 4	Reset start diode discriminator threshold	2
q	1989 Jul 18	Replaced damaged dichroic	2
r	1989 Jul 24	PMT suffered small laser burn	0
s	1989 Aug 7	Moved PMT to avoid burn	0

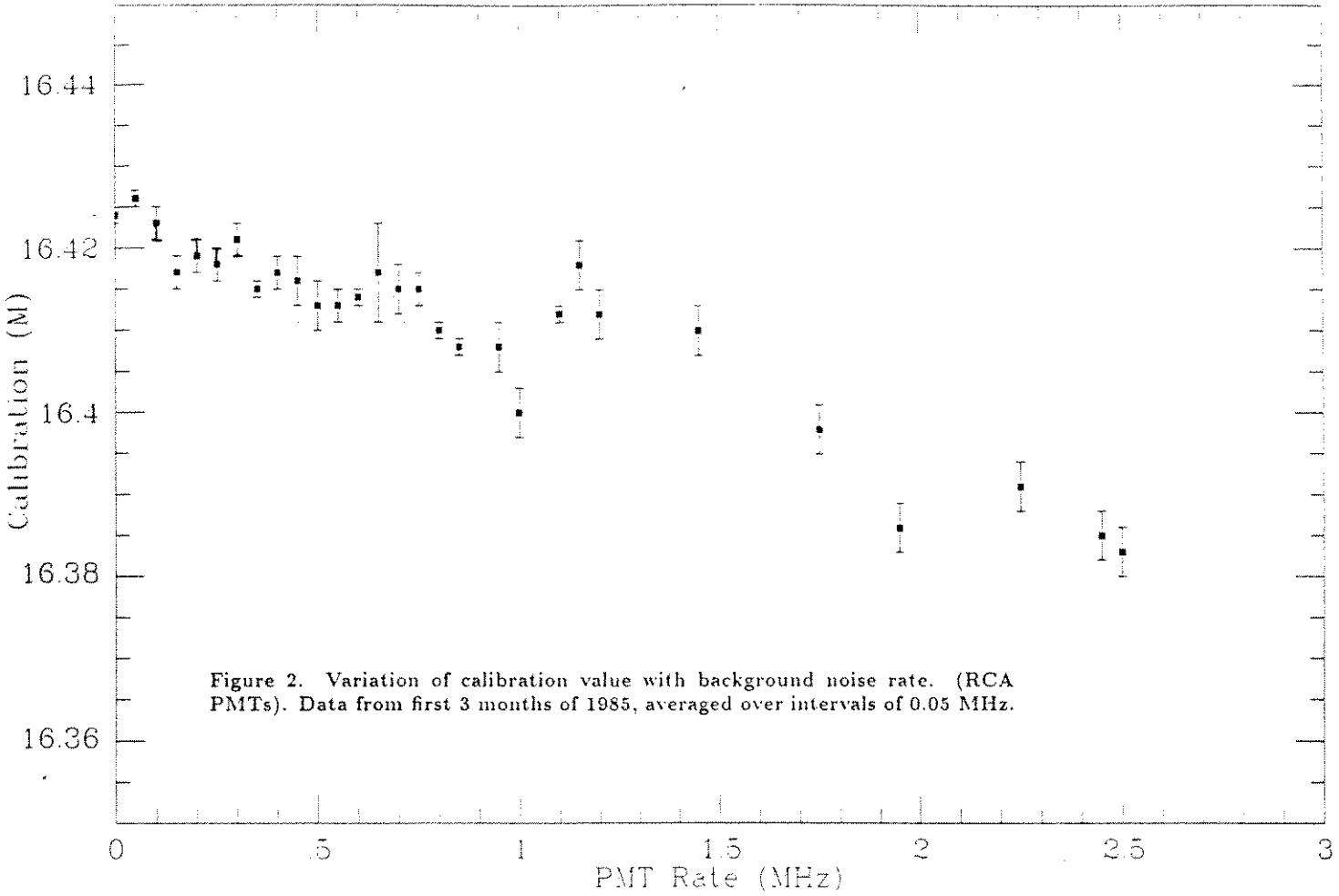

Figure 2. Variation of calibration value with background noise rate. (RCA PMTs). Data from first 3 months of 1985, averaged over intervals of 0.05 MHz.

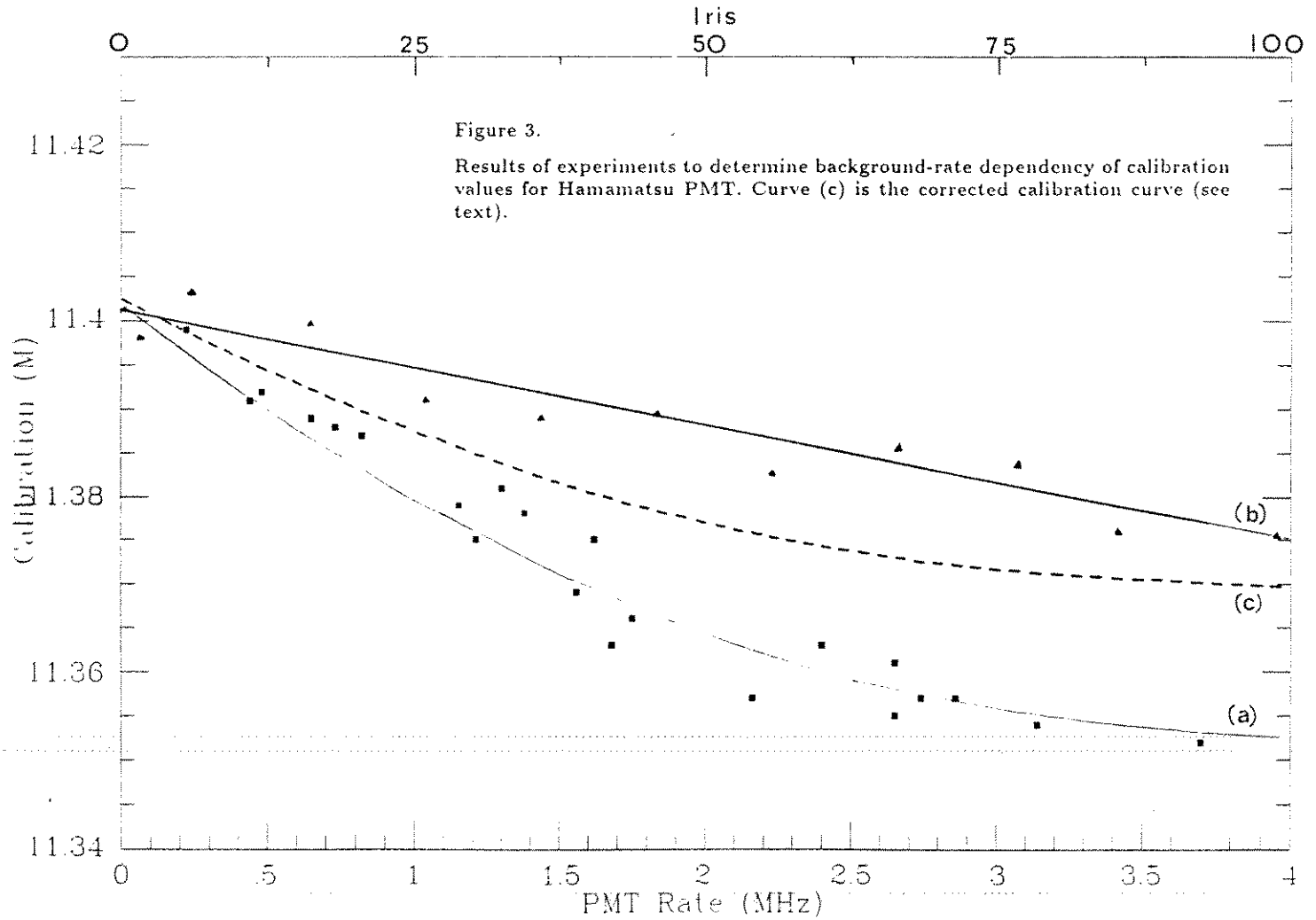

Figure 3.

Results of experiments to determine background-rate dependency of calibration values for Hamamatsu PMT. Curve (c) is the corrected calibration curve (see text).

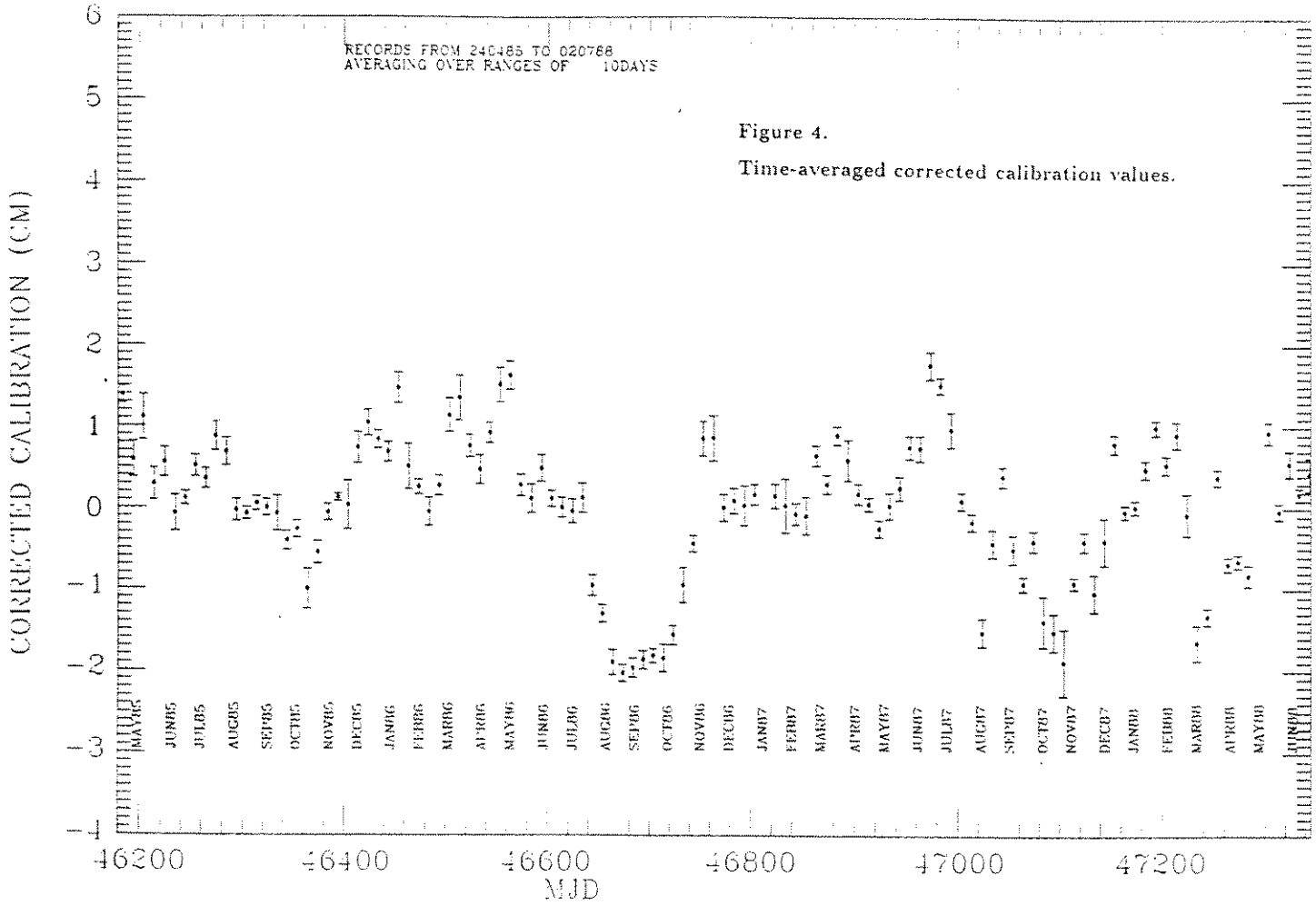

Figure 4.

Time-averaged corrected calibration values.

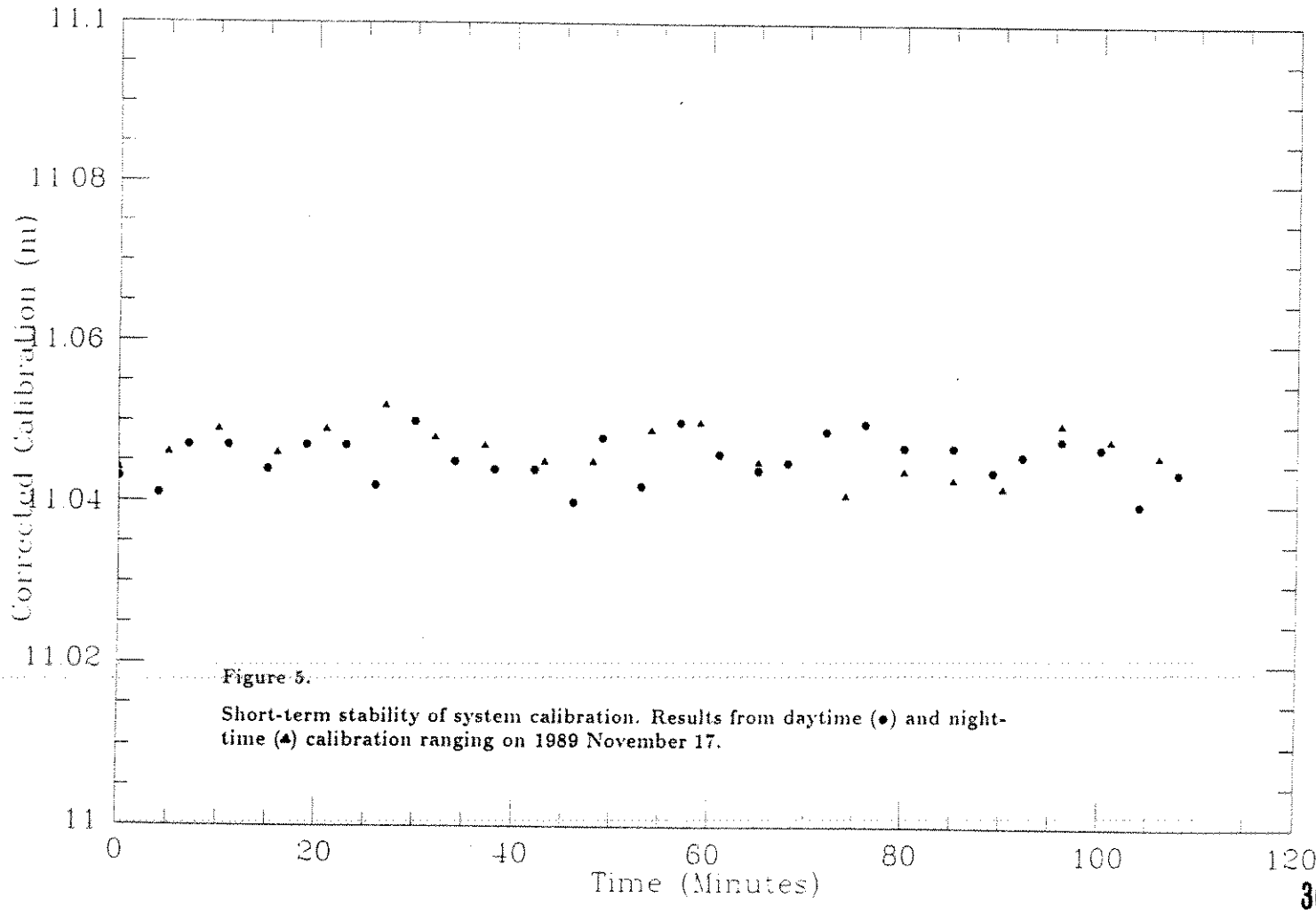

Figure 5.

Short-term stability of system calibration. Results from daytime (•) and nighttime (▲) calibration ranging on 1989 November 17.

CORRECTION OF LASER TRACKING DATA FOR VERTICAL AND HORIZONTAL REFRACTION.

A. Banni, E. Proverbio, V. Quesada
Astronomical Observatory, Cagliari, Italy

ABSTRACT

To compute the SLR data the Saastominien-Marini-Murray's model for the correction due to the atmospheric refraction is usual.

In previous works we have verified the reliability of this model in the Tyrrhenian and Mediterranean area.

The refraction has been calculated by means of radiosonde balloons carrying out observations for more than one year and twice a day without stopping. The differences, between these data and those expected by Marini-Murray's model, are more than ten cm for 90° elevation.

At the moment we are building a model of the atmospheric refraction available for the Sardinian area. These model is based on atmospheric parameters measured every 100 meters of altitude till 16000 m by means of radiosonde balloons and for low elevations it considers the horizontal refraction.

In last years there was an improvement in the study of atmospheric refraction index in order to contribute to evaluate refractivity effects on laser ranging observations.

Today to compute laser tracking data the Saastomoinen-Marini-Murray's formula for correction due to the atmosphere refraction effects is usual.

In previous works we have verified the reliability of this model in the Mediterranean area (Banni et al.,1987), and we tried to determine refraction correction terms for laser ranging on the basis of radiosonde data (Banni et al.,1988).

The aim of our effort is to elaborate a local tridimensional atmosphere model using gradients, both vertical and horizontal, of pressure, temperature, humidity and so of refractivity for 6943 A, the ruby laser wavelength.

Punctual atmospheric refractivity has been calculated by means of the parameters carried out both at noon and midnight with radiosonde balloons during 1988.

The refraction index was calculated using following formulae:

phase refraction index n_f

$$(n_f-1)=f(\lambda)\cdot\frac{p-ew}{720.775}\cdot\frac{1+(p-ew)\cdot(0.817-0.0133t)\cdot10^{-6}}{1+0.003661t}+$$

$$+\frac{(3159+0.2963)\cdot10^{-8}}{1+0.003661t}\cdot ew\cdot(1+27.1^{-6}\cdot ew)$$

(Edlen, 1966)

$$(n_f-1)\cdot10^{8}=7844.5\cdot\frac{p}{T}-1238\cdot\frac{ew}{T}$$

(Motrunič, 1979)

$$N_f=(287.604+1.6288/\lambda^{2}+0.0136/\lambda^{4})\cdot(p/1013.25)\cdot$$

$$\cdot(273.15/T)-11.2683\cdot ew/T$$

(Gardner, 1976)

group refraction index n_g

$$(n_g-1)= \frac{173.3+1/\lambda^2}{173.3-1/\lambda^2} * (n_f-1)$$

(Motruniċ, 1979)

$$N_g=80.343 * f(\lambda) * p/T-11.27 * ew/T$$

(Gardner, 1979)

In this paper we used the Gardner formulae, but we plan to verify the reliability of several formulae by means of ground targets laser ranging.

The differences between refractivity observed data and those calculated using Marini-Murray's atmospheric model, show values on the order of a few cm for 90 degrees elevations in SLR measurement corrections.

In fact in the Tyrrhenian-Mediterranean area the troposphere is very different from spherical symmetry model.

Figures 1, 2, 3 show the mean vertical gradients versus altitude. In these figures we observe both pressure and refractivity gradients are negative with an exponential trend. Temperature gradient is negative with an almost constant trend.

Figures 4, 5, 6 show the mean horizontal gradients versus altitude. In these figures there is a clear evidence that within one kilometre absolute gradients are often less than those of instrumental resolution (1*10^-1).

Figures 7,8 show differences determined at 12h and 24h respectively between SLR measurement corrections calculated by means of atmospheric observed data and using Marini-Murray model.

Results obtained seems to confirm reliability of our model but it needs to analyze long data series to verify this procedure from a quantitative point of view.

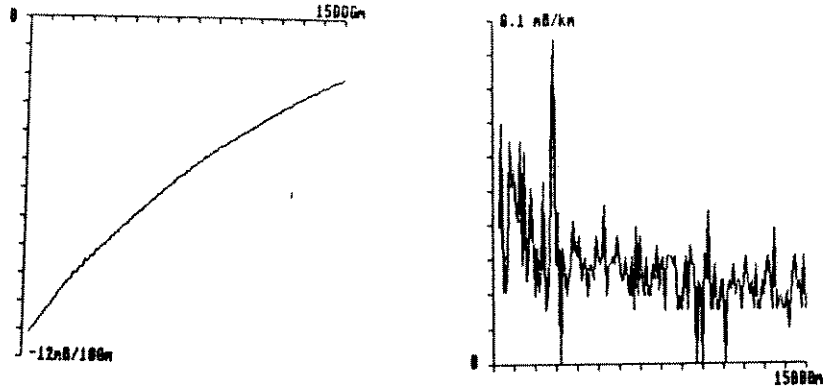

Fig.1,2, Mean vert. gradient and mean horiz. gradient of pressure

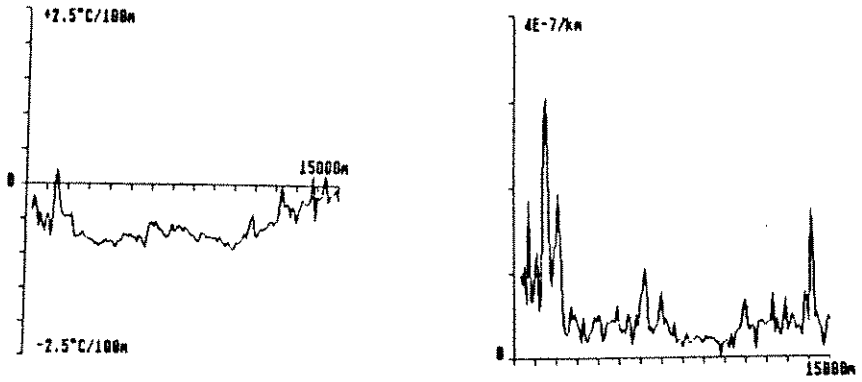

Fig.3,4, Mean vert. gradient and mean horiz. gradient of temperature

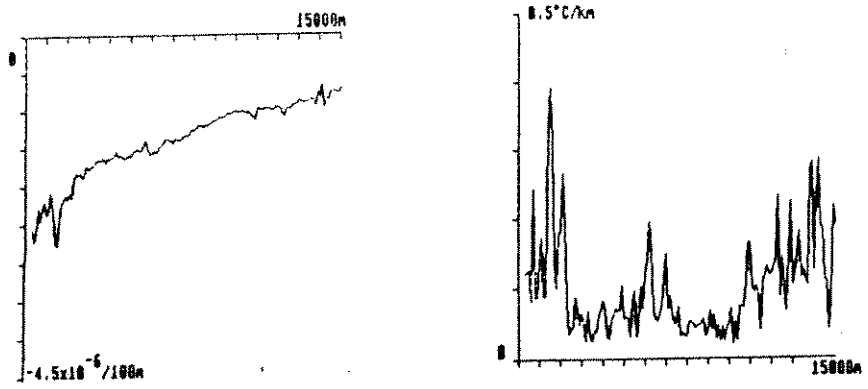

Fig.5,6, Mean vert.gradient and mean horiz. gradient of refraction index

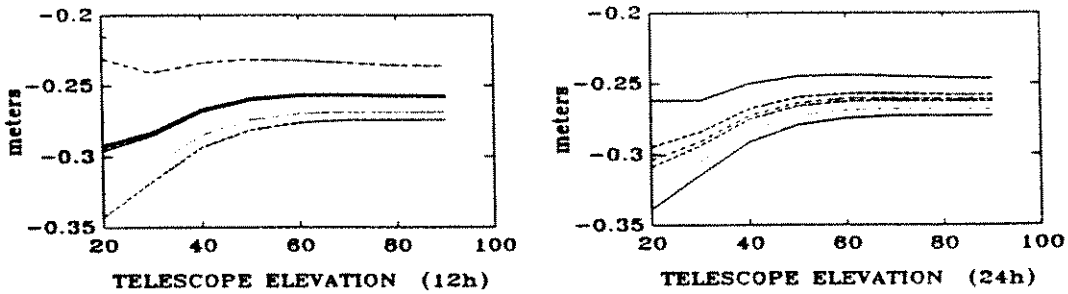

Fig. 7,8, Differences between corrections calculated by means of observed data and by means of Saastamoinen-Marini-Murray's model. Each diagram is referred to days 1, 3, 4, 5, 6, 7 March 1988.

Ground atmospheric parameters:

Fig.1	day	5	1	4	6	3	2
line (from the top)		1	2	3	4	5	6
Pressure (mmBar)		993.0	1007.6	1006.6	1001.1	1010.2	1016.0
Temperature (°C)		13.5	7.0	12.4	9.8	12.0	9.9
Relative Humidity (%)		56.0	93.0	56.0	85.0	66.0	32.2

Fig.2	day	1	3	5	4	2	6
line (from the top)		1	2	3	4	5	6
Pressure (mmBar)		1008.1	1002.0	999.5	1014.5	1005.2	1006.7
Temperature (°C)		6.4	10.0	10.8	10.6	11.0	11.0
Relative Humidity (%)		93.0	55.0	93.0	55.0	98.0	70.0

Elevation	20	30	40	50	60	70	80
Mean at 12^h	0.29	0.27	0.26	0.26	0.26	0.26	0.26
Mean at 24^h	0.30	0.29	0.28	0.27	0.27	0.27	0.27

Last table shows mean differences, for a spring week, from Saastamoinen-Marini-Murray's model exceed 26 cm at noon and 27 cm at midnight, they are too large as regards to required precisions.

REFERENCES

G.S. Gardener - CORRECTION OF LASER TRACKING DATA FOR THE EFFECTS AT HORIZONTAL REFRACTIVITY GRADIENTS -
Applied Optics 16(a), 1977.

J.W. Marini - CORRECTION OF SATELLITE TRACKING DATA FOR AN ARBITRARY TROPOSPHERIC PROFILE - Radio Science 7(2), 1972

I.I. Motrumic, I.V. Svalagin - ON DETERMINATION OF ATMOSPHERIC CORRECTION TO LASER MEASUREMENTS -
Astrometria i Astrophisika 37, 1979

J.J. Freeman - REAL TIME COMPENSATION FOR TROPOSPHERIC RADIO REFRACTIVE EFFECTS ON RANGE MEASUREMENTS -
Nasa Tech. Rep 109, 1964

J. Saastomoinen - INTRODUCTION TO PRACTICAL COMPUTATION AT ASTRONOMICAL REFRACTIVE - Bull. Geod. 107, 1972

J.W. Marini, J. Murray - CORRECTION OF LASER RANGE TRACKING DATA FOR ATMOSPHERIC REFRACTION AT ELEVATION ANGLE ABOVE 10 DEGREES - Nasa Tech. Rep. X, 1973

S. Takagi - ASTRONOMICAL REFRACTION AT THE ATMOSPHERE -
ILOM, 1974

A. Banni, E. Proverbio, V. Quesada - ATMOSPHERIC REFRACTION EFFECTS ON LASER RANGING OBSERVATIONS - Proc. WEGENER-MEDLAS Workshop, Bologna 1987

A. Banni, E. Proverbio, V. Quesada - METEOROLOGICAL GRADIENT CORRECTION TERMS FOR LASER TRACKING DATA AT CAGLIARI - 100 IAU Colloqium, Beograd 1988 (in press)